Preben J.S. Vie

Characterisation and Optimisation of the Polymer Electrolyte Fuel Cell

Institutt for kjemi

Norges teknisk-
naturvitenskapelige universitet
NTNU

Avhandling nr. 37 - Mai 2002

Characterisation and Optimisation of the Polymer Electrolyte Fuel Cell

Preben J.S. Vie
Institutt for kjemi
Norges teknisk-naturvitenskapelige universitet
NTNU
Trondheim, Norway

Doktoringeniøravhandling 2002:37
IFK 2002:57
ISBN 82-471-5431-5
ISSN 0809-103X

Preface

My interest for fuel cells emerged during 1995. I was working in the same laboratory as Steffen Møller-Holst. He was finishing his doctoral work on polymer fuel cells and I was working on my master degree on transference numbers at the former Department of Physical Chemistry, Norwegian Institute of Technology (NTH), University in Trondheim. Steffen was extremely enthusiastic about fuel cells, and this influenced my growing interest for fuel cells. The concept of fuel cells has an elegant approach to solving some of the major environmental issues. Fuel cells have a potential of high fuel efficiency in addition to a pollution free exhaust. I was enchanted.

In January 1996, I received a grant from the Research Council of Norway, enabling me to start my thesis work on polymer fuel cells. Professor Signe Kjelstrup has been my primary supervisor. She has been extremely patient during these years, supporting my work with invaluable help and understanding. Her husband, Professor Dick Bedeaux, deserves recognition for his help with the theory.

Steffen Møller-Holst has acted as my secondary supervisor, giving me advice on most subjects related to fuel cells. Even if Steffen has not been related to Department of Chemistry since 1997, we still have had many valuable discussions on fuel cells. Steffen's advice were invaluable when I rebuilt and reconstructed the fuel cell test-facility. I am also extremely grateful for all his assistance during these years both professional and personal. I'm grateful for Steffen's friendship and guidance through the American bureaucracy during my stay at Los Alamos National Laboratory.

Also, I would like to thank my colleague and office roommate for the last one and a half years, Rune Halseid, for all our discussions, and for his help reading through this thesis. Rolf Jarle Aaberg has given me valuable input. Monica Strømgård performed several experiments in the laboratory, and deserves recognition for that work. In 1997 Mikael Paronen convinced me that his membrane was worth testing. After a lot of struggles with his membrane, a chapter in this thesis evolved. Without Hans Petersen's electronic expertise, the building of the fuel cell test-facility would have been much more difficult. The assistance from Nils Wæraas and Ketil Joner at the workshop enabled the building of the new test-facility.

I am grateful to the people working at the Laboratory of Physical Chemistry for a pleasant working environment. Since August 2000, the people at Department of Materials Technology and Electrochemistry, have been my colleagues. They have supplied me with an equivalently pleasant workplace. John Georg Seland should be thanked for making the days at Physical Chemistry even more enjoyable, as well as evenings, both at NTNU and exploring Trondheim's night-life.

In 1998, Inger-Kristin entered my life. Since then, she has been a never-ending support, comfort and life-companion. I want to thank her for her patience and understanding for my late evenings at work. I would also like to thank my family for all their encouragements. Finally I am dedicating this thesis to my late father Rudolf Vie. Without his support in early days, my impetus for science and technology would probably have disappeared during school.

Summary

This thesis presents work performed on five subjects of the polymer fuel cell:

- A polymer fuel cell test-facility was optimised. A fuel cell housing was designed and built, enabling measurements of local fuel cell temperatures. The fuel cell voltage was measured between the gas diffusion backings using thin platinum wires. This assures that the true fuel cell voltage is measured.
- The Nafion® content and content of Acetylene Black in the fuel cell electrode was optimised in a 3^2-factorial experiment. The amount of Nafion varied between 15, 25 and 35 wt%, and Acetylene Black varied at 0, 5 and 10 wt%. The data was analysed with the Bootstrapping method, and the reproducibility was assessed. The optimal amount of Nafion was found at 35 wt%. There was no significant optimum for the Acetylene Black content.
- A novel fuel cell membrane was tested in the polymer fuel cell. The membrane was a proton irradiated and directly sulfonated poly(vinyl fluoride) (PVF-SA) membrane. The performance was slightly better than for a Nafion® 117 membrane tested under the same conditions.
- A fuel cell model based on irreversible thermodynamics was presented. The model was a one-dimensional model solving the heat and water transport perpendicular to the membrane surface. A potential and temperature profile was calculated, based on literature data. Temperatures inside the membrane (Nafion® 117) were estimated to be 5 °C higher at 1 A/cm^2 than in the gas channels.
- The local temperatures were measured inside the polymer fuel cell. At 1 A/cm^2 the temperature difference between gas channel and membrane

was measured to 6 ^{o}C. The thermal conductivities in the membrane, backing and catalytic layer were estimated from the temperature measurements. The thermal conductivity of the gas diffusion backing with electrode was 0.19 ± 0.05 W/mK and the thermal conductivity of the Nafion® 115 membrane was estimated to 0.1 ± 0.1 W/mK. The heat-transfer coefficient of the electrodes was calculated to 1000 ± 300 W/m^2K.

List of symbols

Latin characters

a_x	activity of substance x
A	area in fuel cell model ($5\mathrm{cm}^2$)
A	substance A
b	Tafel constant (V)
B	substance B
C_p	heat capacity (J/Kmol)
d^y	thickness in phase y (m)
d_{memdry}	dry membrane thickness (m)
$D_{\mathrm{H_2O},\lambda}$	diffusion coefficient for water referenced to the water content λ (m^2/s)
$D^{'}_{\mathrm{H_2O}}$	intra-diffusion coefficient of water (m^2/s)
$D_{\mathrm{x_1x_2}}$	binary diffusion coefficient of substance x_1 in substance x_2 (m^2/s)
F	Faraday constant (96485 C/mol)
F^y_x	gas flow of substance x in part y (mol/s)
G_x	Gibbs energy for substance x (J/mol)
h_x	enthalpy for substance x (J/mol)
H_x	enthalpy for substance x (J/mol)
j	current density ($\mathrm{A/cm}^2$)
j^0_x	exchange current density ($\mathrm{A/cm}^2$)
J^y_x	flux of substance x in part y ($\frac{\mathrm{mol}}{\mathrm{m}^2\mathrm{s}}$)
J'_q	heat flux ($\mathrm{J/m}^2\mathrm{s}$)
l	phenomenological coefficient
M_x	molecular or equivalent weight of substance x ($\frac{\mathrm{g}}{\mathrm{mol}}$)
P_0	standard gas pressure (101.325 kPa)

P^{cr}	critical pressure (Pa)
P_T^{sat}	saturation pressure of a gas at a given temperature T
P_x	partial pressure of substance x (Pa)
r	specific resistance ($\Omega\mathrm{cm}^2$)
r^y	resistance in phase y (Ωm)
$\mathrm{r}^{s,y}$	resistance in surface y ($\Omega\mathrm{m}^2$)
r^2	correlation coefficient
R	the universal gas constant (8.3143 $\frac{\mathrm{J}}{\mathrm{Kmol}}$)
R_{mem}	membrane resistance ($\Omega\mathrm{m}^2$)
s	membrane swelling factor (s = 0.0126 for Nafion®117 membrane) ($d^m = (1 + s\lambda) \cdot d_{memdry}$)
S	entropy (J/Kmol)
s_i	standard deviation for model i
T_0	normal temperature (273.15 K)
T^{cr}	critical temperature (K)
T^y	temperature in part y (K)
U_x^y	gas flow of substance x in part y ($\frac{\mathrm{l_N}}{\mathrm{min}}$)
x_x	mole fraction of substance x

Greek letters

α	net water transport factor in membrane ($\frac{F^a_{\mathrm{H_2O}}}{F_{\mathrm{H_2}}}$)
α^a	anodic symmetry factor in Butler-Volmer equation
α^c	cathodic symmetry factor in Butler-Volmer equation
ϵ	porosity
η	overpotential
θ	volume fraction
λ	water concentration in membrane ($\frac{n_{\mathrm{H_2O}}}{n_{\mathrm{RSO_3^-}}}$)
λ^m	thermal conductivity in membrane (W/mK)
λ^b	thermal conductivity in the backing (W/mK)
$\lambda^{s,g}$	heat transfer coefficient ($\mathrm{W/m^2K}$)
μ_x	chemical potential (J/mol)
ξ_x	conversion of substance x ($\frac{F_\mathrm{x}}{F_\mathrm{x}^{in}}$)
π	Peltier heat (J/mol)
ρ	density ($\mathrm{kg/m^3}$)
σ	conductivity (S/m)

τ	tortuosity
ϕ	potential (V)

Subscripts

H_2	hydrogen
O_2	oxygen
H_2O	water
tot	total
w	water
x	substance x (examples: H_2, O_2 and H_2O)

Superscripts

1	interface between the anode gas channel and the anode gas diffusion backing
2	interface between the anode gas diffusion backing and the anode electrode
3	interface between the cathode gas diffusion backing and the cathode electrode
4	interface between the cathode gas diffusion backing and the cathode gas channel
a	anode
b	backing
c	cathode
cr	critical
g	gas
hum	humidifier
in	substance entering anode or cathode side
l	liquid
liq	liquid
m	membrane
out	substance leaving anode or cathode side
s	surface
sat	saturated
tot	total

vap	vapour
y	location and phase in system (examples: a, l, in,a or s,c)

Abbreviations

AB	Acetylene Black
AFC	Alkaline Fuel Cell
ICE	Internal Combustion Engine
MEA	Membrane and Electrode Assembly
MCFC	Molten Carbonate Fuel Cell
OCV	Open Circuit Voltage
PAFC	Phosphoric Acid Fuel Cell
PEEK	Poly(ether ether ketone)
PEFC[1]	Polymer Electrolyte Fuel Cell
PEM	Polymer Electrolyte Membrane
PEMFC[1]	Polymer Electrolyte Membrane Fuel Cell
PES	Polyethersulfone
PVF	Poly(vinyl fluoride)
PZEV	Partial Zero Emission Vehicle
SOFC	Solid Oxide Fuel Cell
SPEFC[1]	Solid Polymer Electrolyte Fuel Cell
SPFC[1]	Solid Polymer Fuel Cell
SS-316	Stainless steel alloy
SULEV	Super Ultra-Low Emission Vehicle
ZEV	Zero Emission Vehicle

---

[1] PEFC, PEMFC, SPEFC and SPFC denote the same type of fuel cell: The Solid Polymer Electrolyte Membrane Fuel Cell (SPEMFC) ...

Contents

Preface iii

Summary v

List of symbols vii

Contents xi

1 Introduction 1
- 1.1 Background 1
- 1.2 Problem statement 4
- 1.3 Outline of the thesis 6

2 The fuel cell test-facility 9
- 2.1 Introduction 9
- 2.2 The fuel cell housing 10
- 2.3 The test-station 13
- 2.4 Conclusion 17

3 Electrode optimisation 19
- 3.1 Introduction 19
- 3.2 Experimental 20
- 3.3 Results and Discussion 21
- 3.4 Conclusions 26

4 Testing of new membrane types 29
- 4.1 Introduction 30
- 4.2 Experimental 31

4.3 Results and discussion 33
4.4 Conclusion 38

5 Polymer fuel cells described by irreversible thermodynamics 41
5.1 Introduction 41
5.2 System description 43
5.3 Conservation of charge, mass and energy 46
5.4 Entropy production and flux equations 48
5.5 Cell potential and overpotentials 55
5.6 Cell dimensions and properties 60
5.7 Further results 62
5.8 Discussion and conclusions 67
List of symbols 69

6 Local heat production 71
6.1 Introduction 71
6.2 Thermal effects 72
6.3 Temperature measurements 77
6.4 Thermal conductivities 82
6.5 Conclusions 91

Bibliography 93

Appendices 105

A The fuel cell model 105
A.1 The structure of the fuel cell model 105
A.2 Solving the fuel cell model 106
A.3 Assumptions 107
A.4 Equations 107
A.5 Auxiliary equations 118
A.6 Substantiation of the model 119

B Fit of polarisation curve data 127
B.1 Introduction 127
B.2 Theory 127
B.3 Experimental 131
B.4 Results and discussion 131
B.5 Conclusion 136

C Preparation of thermocouples 137
C.1 Thermocouple description 137
C.2 Coating the thermocouples 138
C.3 Testing of isolated thermocouples 140
C.4 Stability of the coating 142
C.5 The dimension of the isolated thermocouple 143

D The data acquisition system and control program 145
D.1 The data acquisition system 145
D.2 Control program 146
D.3 Analyzing the data 151

Chapter 1

Introduction

1.1 Background

1.1.1 A brief history of the fuel cell

W. R. Grove [Grove, 1839, 1842] has for a long period been credited as the inventor of the fuel cell [Blomen and Mugerwa, 1993]. Recently, C.F. Schönbein has also been credited this invention [Bossel, 2000]. The fuel cell's ability to combine hydrogen and oxygen to water, described by Scönbein, was performed in an acidic solution. Details from Schönbein's discovery is documented by Bossel [2000]. During the following century other fuel cell types were demonstrated by different scientists. F.T. Bacon's development of the modern alkaline fuel cell (AFC) in the 1930s represented the first approach toward fuel cell commercialisation. He could, in 1959, demonstrate an alkaline fuel cell stack producing 6 kW, on pressurised hydrogen and oxygen. [Blomen and Mugerwa, 1993].

In the 1960s the fuel cell was further developed by NASA in their space program, driven by the need for very compact units producing electricity and water. The polymer fuel cell (PEMFC) was first demonstrated in the Gemini space program. Two 1 kW units were utilised for on-board electricity production. But, the PEM fuel cell was found inferior to the alkaline fuel cell with respect to performance and durability. Therefore, the AFC was chosen for the later Apollo-program and in the Space-shuttles still being launched.

In the 1970s the energy crises stimulated research on fuel cells for terrestrial applications. Phosphoric acid fuel cell (PAFC) plants were manufactured and they became commercially available during the first half of the 1990s. A large-scale PAFC plant has for example been running in Japan producing 4.8 MW of electricity [Blomen and Mugerwa, 1993]. Matsumoto and Kasahara [1998] document the large activity on PAFCs in Japan.

Membranes with better stability and performance than the membranes used by the Gemini-program, were discovered[1] for use in PEM fuel cells. And in the 1980s the PEMFC achieved much higher power densities than the Gemini fuel cell stack. Today the PEMFC is the most promising low temperature fuel cell for *transportation applications*, since it is very compact. The use of solid materials reduces corrosion problems.

The solid oxide fuel cell (SOFC) is a promising technology for *stationary power plants*, due to high waste heat quality (800 - 1000 °C) and high energy efficency [Blomen and Mugerwa, 1993]. Material problems were previously believed to prevent the SOFC from broad commercialisation [Thomas and Zalbowitz, 1999].

1.1.2 Fuel cells of today

The PEM fuel cell is expected to become a viable alternative to the internal combustion engine (ICE) for vehicle propulsion. Prototypes of fuel cell powered electric buses are already running in public transportation systems in Canada and USA, and several prototypes of fuel cell cars have been introduced. DaimlerChrysler has launched its own program for fuel cell cars and plan to have a car ready for the market in 2004. [DaimlerChrysler, 2001a]. They have already demonstrated the propulsion of small cars in the Mercedes A-class, running on methanol (NECAR 5) or liquid hydrogen (NECAR 4) [DaimlerChrysler, 2001b]. The liquid hydrogen car (NECAR 4) has a range of 450 km. In NECAR 5, methanol is reformed to hydrogen on-board, giving a range of 400 km with 40 litres methanol. This may not seem very impressing, but taking into account that the volumetric energy density of methanol is half that of gasoline, some of the potential of the fuel cell is demonstrated. Other car manufacturers have also demonstrated similar cars.

What is the reason for this "modern" interest in the fuel cell? Towards the end of the 20th century the regulations/laws for the emissions from the ICE cars have become stricter, and far less emissions are allowed. In California, USA, 10 % of new vehicles sold by a car manufacturer has to be "zero emission vehicles" (ZEV) in 2003 according to Lloyd [2000]. Recently, this demand

---

[1] DuPont developed the Nafion® membrane for the chlor-alkali process in the late 1960s

was revised to 2 % pure ZEVs, 2 % advanced partial zero emission vehicles (PZEVs) and 6 % conventional PZEVs [Lloyd, 2001]. Still, this is a tough goal to reach for the car-industry. Especially when the electric vehicle (EV) driven on rechargeable batteries is only able to reach 200 km on every recharge of the battery [Galloway and Haslam, 1999], and the energy densities of the batteries are relatively low [Appleby, 1995; Kalhammer, 2000], compared to the fuel cell. The on-board hydrogen fuel cell vehicle is considered a ZEV.

The fuel cell is similar to an electric battery, the difference being that the fuel cell is continuously supplied with fuel. The fuel may be stored in tanks comparable to the petrol tanks for ICE. The fuel is usually hydrogen, but hydrogen can be stored in different energy carriers [Metkemeijer and Achard, 1994; Ogden et al., 1999; Prigent, 1997; Thomas et al., 2000; Ellis et al., 2001]. As mentioned above, a fuel cell car powered by methanol is demonstrated, but ammonia is also a promising carrier for hydrogen [Adlhart and Terry, 1969; Bloomfield et al., 1982; Ross Jr., 1981; Szymanski et al., 1980]. In addition, natural gas is hydrogen-rich, and can be fed into fuel cells operating at high temperatures, i.e. SOFCs, or molten carbonate fuel cells (MCFCs). The natural gas may be converted to hydrogen through an internal reforming reaction. In low temperature fuel cells, natural gas has to be preprocessed and converted into hydrogen-rich gas before entering the fuel cell. Most of the hydrogen-rich energy carriers are processed this way. Methanol (and ethanol) has proved to work directly as fuel in the polymer fuel cell [Ren et al., 1996; Wang et al., 1995]. The other types of low temperature fuel cells, alkaline fuel cells and phosphoric acid fuel cells, have somewhat stronger requirements to the fuel. The alkaline fuel cell is operated only on very pure gases, both hydrogen and air must be virtually CO_2-free. The phosphoric acid fuel cell can use fuels containing quite high amounts of some impurities (CO/CO_2), but no other fuels than hydrogen are possible.

Fuel cells can operate very efficiently compared to the ICE; electric efficiencies of 50 - 70 % from hydrogen til electricity are possible at reasonable current densities. The fuel cell reaction is not restricted by the Carnot cycle as is the ICE. The energy converted into electrical energy in the fuel cell is restricted by the Gibbs energy of the fuel cell reaction. The reaction where hydrogen and oxygen produces liquid water and electricity, would ideally give us 1.18 V at 80 ^{o}C, or 237 kJ/mol hydrogen converted. Due to irreversibilites, both heat and electricity are produced, and the fuel cell usually operates at 0.7 V (around 60 % efficiency referenced to Gibbs energy). In the combustion of hydrogen and oxygen, 286 kJ/mol heat is produced. Therefore, 83 % of the potential combustion energy is left for the ideal fuel cell reaction. This means that the efficiency for the fuel cell reaction actually is around 50 % on a higher heating value basis at 0.7 V. We see that the fuel cell more than doubles the fuel efficiency, compared to the ICE, which normally has an efficiency of about 20 %. When considering the total efficiency for a vehicle, the efficiencies will be lower.

The conversion of hydrogen in a fuel cell is a very clean and environmental friendly process. Only water is produced as exhaust, and SO_x and CO/CO_2 emissions are eliminated. BMW is running a 750hL limousine directly on hydrogen in an ICE [BMW, 2002; Pehr et al., 2001]. In the ICE some NO_x will be produced depending on the working temperature in the engine.

When running a fuel cell on methane or methanol some CO_2 is produced, but to a much lesser extent than in the ICE, due to the higher efficiency in the fuel cell. Such cars are defined as Super Ultra-Low Emission Vehicles (SULEV) in California [Lloyd, 2000].

1.2 Problem statement

As discussed in chapter 1.1, the PEMFC is soon to be commercialised. Well-performing fuel cell stacks and systems have been developed [Panik, 1998; Acres, 2001; DaimlerChrysler, 2001a], and the power density of Ballard Power System's stacks has improved almost 7 fold in five years, from 0.15 kW/l and 0.11 kW/kg at an average cell voltage of 0.57 V in 1990 to 1 kW/l and 0.7 W/kg at 0.68 V in 1995 [Prater, 1994, 1996]. According to Kalhammer [2000], Ballard has even reached 1.4 kW/l. The power density of a fuel cell system is important, especially for mobile applications. Additionally, the fuel efficiency is also very important for the competitiveness, compared to ICE vehicles. A goal for most PEM fuel cell systems has been to reach a nominal operation voltage of 0.7 V or higher. This should ensure a fuel cell stack efficiency of approximately 50%. By increasing the voltage further, an even higher efficiency is obtained. The problem of increasing the operation voltage is the inherent reduction in current density and therefore also a low power density. Recently, Uribe et al. [2001] reported a PEM fuel cell running at 0.8 V and 0.4 A/cm^2. This performance is comparable to most performances at 0.7 V.

Despite these pronounced performance improvements, there is still a lot left to be done. Most commercial fuel cell electrodes in fuel cell stacks contain more expensive Pt-catalyst (often more than 2 mg Pt/cm^2, Gore PRIMEA® have a loading of 0.4 - 0.5 mg Pt/cm^2) than the smaller fuel cell test MEA's (less than 0.2 mg Pt/cm^2) in different laboratories around the world [Wilson et al., 1995; Kumar et al., 1995; Passalacqua et al., 2001; Ihonen et al., 2001] and the electrode compositions must be optimised further. The main impetus for the fuel cell reaction is an enhanced contact area between the reacting gases, electron conductor and protonic conductor on the catalyst surface, constituting the three-phase boundary. This means that there is a need for protonic conductor for instance in the form of Nafion®-polymer, electronic conductor in the form of porous carbon, and a catalyst, typically platinum. Finally, there has to be gas voids close to the catalyst surface, all together constituting the catalyst layer in the fuel cell. These demands are usually solved by mixing finely dispersed platinum on carbon-powder (Vulcan XC-72) with a Nafion®-solution, and finally adding appropriate solvents. This slurry can be sprayed or pasted onto the membrane or gas-diffusion electrode and parameters like drying time and drying temperature can be varied. Interaction between factors is important to ensure that a real optimum composition and morphology is found. In this thesis the electrode composition is optimised with respect to ionomer content and electronic conductivity in chapter 3.

The price of the fuel cell system is to a large extent dependent on the price of the proton conducting membrane, catalyst and bipolar plate materials. In polymer fuel cells the Nafion®117 membrane is widely used, and it has a price of more than \$800/m^2. Several manufacturers are trying to replace this expensive perfluorinated membranes with cheaper and better performing membranes [Ledjeff-Hey and Heinzel, 1996; Büchi et al., 1995]. A promising material is the directly sulfonated PVF-membrane [Paronen, 1999]. The base polymer in this material is cheap (\$10/m^2). The preparation method is simple, and it can easily be scaled up for large-scale production. The polymer is irradiated with protons to create radicals. Then the material is directly sulfonated with chlorosulfonic acid, and finally the material is cleaned [Paronen, 1999]. Due to the simplicity of the preparation method, the production costs will be low. The membranes have to be tested under realistic fuel cell conditions. Results from tests of such membranes is reported in chapter 4.

In order to obtain a better understanding of the dynamics of polymer fuel cells, mathematical models are valuable tools. Several mathematical models describing the polymer electrolyte fuel cell exist [Springer et al., 1991, 1993; Bernardi and Verbrugge, 1992; Fuller and Newman, 1993]. The models usually describe the water transport and electrode kinetics in the fuel cell and try to predict the behaviour of a fuel cell system under varying operation conditions. In this thesis a fuel cell model based on irreversible thermodynamics [Førland et al., 1988] is presented (chapter 5).

A very important aspect in fuel cell systems is the heat-management. Where is the heat produced and how fast is the heat dispersed in the system? These are key-questions in the modelling and construction of fuel cell stacks. High temperatures can cause the membrane to dry-out and reduce the membrane conductivity drastically, and platinum particles may start to agglomerate. Fuel cell stacks are usually cooled by air or by circulation of water. When designing the system, knowledge of heat production and heat transport is crucial. The use of irreversible thermodynamics in the modelling of these phenomena will provide insight into the fundamentals of the processes taking place in the fuel cell [Førland et al., 1988]. Irreversible thermodynamics is a theory applying equilibrium thermodynamics to systems not in equilibrium. The system under investigation is separated into smaller subsystems. A model calculating a temperature profile through the membrane is presented in chapter 5. Some of the transport coefficients in the model are not known. To verify the calculated temperature profile, a local temperature profile has been measured as described in chapter 6. Based on this information, thermal conductivities in the fuel cell can then be calculated.

1.3 Outline of the thesis

This thesis consist of a mixture of published and not yet published material:

Chapter 2 presents the fuel cell test-station and the new fuel cell housing. This chapter documents the experimental setup used in chapters 3, 4 and 6, and will not be published.

Chapter 3 describes work on optimisation of the fuel cell electrodes with respect to protonic and electronic conductivity. This work was accepted for poster presentation at the 1998 Fuel Cell Seminar in Palm Springs, USA [Vie and Møller-Holst, 1998]. The results are further elaborated in this chapter, and a new publication is under preparation.

Chapter 4 is an article in press in Journal of Membrane Science. The proton irradiated and directly sulfonated poly(vinyl fluoride) membrane is tested in a fuel cell test-facility. The performance is compared to that of Nafion® 112 and 117 membranes tested under similar conditions. This work is a collaboration between Department of Chemistry, NTNU, Laboratory of Polymer Chemistry, University of Helsinki and the Accelerator Laboratory, University of Helsinki.

Chapter 5 is a publication on a fuel cell model based on irreversible thermodynamics. It was published as a chapter in the book "Surface chemistry and electrochemistry of membranes", edited by Torben Smith Sørensen [Kjelstrup et al., 1999]. An abstract with results from this model was also accepted as an oral presentation at the 49th annual meeting of the International Society of Electrochemistry [Vie et al., 1998]. This work was written in cooperation with Professor Signe Kjelstrup and Professor Dick Bedeaux.

Chapter 6 presents measurements of local temperatures in the polymer fuel cell. Based on these measurements, thermal conductivities are estimated. These results are not yet published, but a publication is under preparation. This work is performed in cooperation with Professor Signe Kjelstrup.

Appendix A presents the basis for the fuel cell model in chapter 5. The equations are more elaborated. The equations will also apply in the calculation of the thermal conductivities in chapter 6.

Appendix B is a short note on fitting polarisation curve data to an empirical model. The model is based on the Butler-Volmer equation describing the electrode kinetics. Equations for the reversible fuel cell voltage as a function of temperature and pressure are also presented.

Appendix C is a chapter presenting the preparation of insulated and isolated thermocouples used for measurement of local temperatures in the fuel cell.

Appendix D is a presentation of the control program and measurement system for the fuel cell test-facility.

Chapter 2

The fuel cell test-facility

This chapter presents the fuel cell test-facility at Department of Chemistry. The original equipment designed by Møller-Holst [1996b] is briefly presented. The changes to the equipment during this thesis project are documented.

2.1 Introduction

The system for testing fuel cell membrane and electrode assemblies (MEA's) was continuously changed during the work with this dissertation. The system was developed by Møller-Holst [1996b]. A fuel cell housing in PES (polyethersulfone) was supporting pistons with parallel flow channels and a geometrical area of 5 cm^2. The pistons were in stainless steel (SS-316), and a pneumatic cylinder controlled the mechanical pressure over the MEA [Møller-Holst, 1996b]. The reacting gases were humidified in stainless steel cylinders of approximately 1 litre. The gas flow-rates and gas pressures were controlled from a computer programmed with LabVIEW. For a more detailed description of the first version fuel cell test-station, see Møller-Holst [1996b].

The last version of the test-station shall be described below. A more stable and better cell performance was sought. The fuel cell housing material was changed, due to the testing of new and fragile proton-conducting membranes, which could burst leading to a H_2/O_2 fire. The data-acquisition system was extended, including better control of the fuel cell load, control of the mass flow according to the conversion of the reacting gases, easier programmed measurements of polarisation curves, and measurements of several temperatures locally inside the fuel cell (Appendix D).

2.2 The fuel cell housing

The fuel cell housing has evolved significantly since Steffen Møller-Holst built the first version [Møller-Holst, 1996b]. He showed the importance of design of gas flow-patterns, and achieved enhanced fuel cell performance, see figure 4.3, page 35 in [Møller-Holst, 1996b]. The second generation piston had a larger current collecting surface and a better gas flow pattern. Møller-Holst included a reference electrode in the centre of the piston. Another major contribution to the design of the fuel cell housing was the introduction of a pneumatic cylinder for controlling the mechanical pressure over the MEA. The effect of the mechanical pressure is demonstrated in figure C2 in [Møller-Holst, 1996b]; higher mechanical pressure enhances fuel cell performance. This author has observed similar effects.

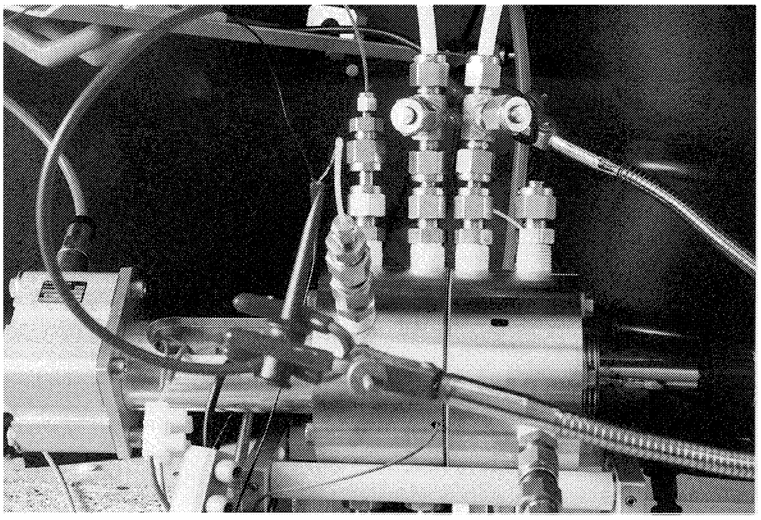

Figure 2.1: The fuel cell housing assembled for testing in the fuel cell test-station. The pneumatic cylinder is to the left. The reacting gases enter at top. Several wires for connecting voltage and temperature-measurements are shown.

The new fuel cell housing design has the whole cell housing built in stainless steel (SS-316). The rationale was to assure that the system could withstand small fires when testing new, fragile polymer electrolytes. A small fire in the cell can ignite a larger melt-down/fire of the fuel cell housing in Polyether Sulfone (PES). Experience indicated that PES is fragile and easily brakes when over-tightening screws.

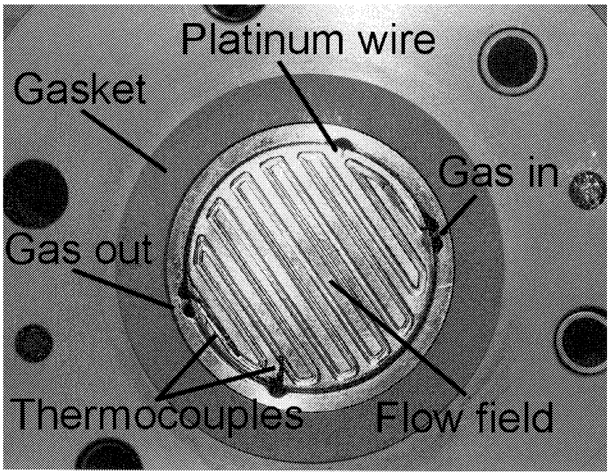

Figure 2.2: The cathode piston top and parts of housing. The platinum wire (Ø 0.1 mm) measures the local cell voltage at the backing. One thermocouple measures the temperature at the outlet of the gas channel, and one can measure the local temperature at the membrane electrode interface. The preparation of the thermocouples is described in appendix C. A gasket (natural rubber) is inserted to keep the cell gas-tight. The surface of the cell-housing is not stainless steel, but a thin plate (1mm) of PEEK. This will avoid short-circuits over the two half cells.

When redesigning the fuel cell housing, some new features were included. Several holes were added in the cell housing for running measurement probes to the top of the piston. These holes enable measurements of local temperatures in the system, and measurements of the real fuel cell voltage at the backings (figures 2.1 and 2.2). The pistons were also redesigned. I introduced the heating element for the fuel cell system inside the piston, similar to the design of Møller-Holst [1996b]. But, the heating element does not penetrate the gas flow-field. Møller-Holst [1996b] used the heating element as a sensor for the reference electrode, but it introduced thermal gradients in the MEA. The new design introduces a flexibility, enabling the researcher to choose whether to use reference electrodes or not. A new design for the reference electrodes was introduced, with possibilities for several reference electrodes on both cathode and anode.

New pistons were designed with interchangeable piston-tops in the same manner as by Møller-Holst [1996b]. A new serpentine-type flow-field design was introduced. See figure 2.2 for a detailed view of the piston. This flow-field pattern will prevent water flooded channels which is more normal in parallel flow channel patterns. Figure 2.2 shows examples of the different types of probes that can be introduced at the piston-top.

The possibility to measure the local cell voltage over the MEA eliminates the previously unknown voltage drops in the stainless steel pistons. The piston-top has been attached to the rest of the piston through a threaded connection. Resistance variations occurred over this contact. Surface resistance in the stainless steel introduces an unknown resistance [Wind et al., 2002]. This effect is demonstrated in table 2.1. We observed large variations in the cell voltage measured at the backings when the current density and cell voltage at the back of the pistons were constant in different experiments. This effect will affect the reproducibility of the fuel cell experiments, e.g. figure 3.2 in chapter 3. These voltage drops should be independent of the type of experiment. If not, the voltage drops over the pistons will vary from fuel cell assembly to fuel cell assembly. A similar effect has been observed by Ihonen et al. [2001].

Table 2.1: The varying total voltage drops over the fuel cell pistons for different experiments.

Experiment	Current density (A/cm^2)	Cell voltage at back of piston (V)	Cell voltage at backing (V)	Total voltage drop over pistons (V)
000525da	1.0	0.2	0.3	0.1
000608da	0.99	0.2	0.25	0.05
000615da	1.02	0.2	0.28	0.08

In figure 2.3 the two half cells were almost ready for assembly. The cathode half cell housing was only missing a membrane with catalytic layers, and the anode cell missed a gas diffusion backing. A thin Teflon gasket (20 μm) can be seen on top of the natural rubber gasket. This gasket prevented contaminations from the rubber gasket from entering the polymer electrolyte.

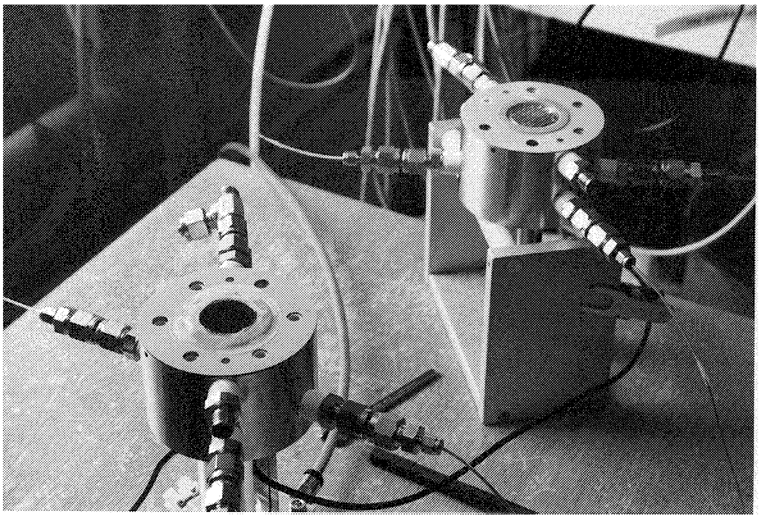

Figure 2.3: The two half cells were almost ready for assembly. The cathode half cell is to the left on the picture, resting on the pneumatic cylinder. The backing (gas diffusion electrode) has been inserted. A thinner Teflon gasket with a defined open area (Ø 25 mm) rests on top of the gasket in natural rubber (figure 2.2). Different probes come out of the half cell housings. In the background (to the right) the anode housing rests on the support for the whole assembled fuel cell.

2.3 The test-station

A photo of the fuel cell test-station taken in 2000 is given in figure 2.4. The fuel cell test-station system was mainly the same as developed by Møller-Holst [1996b]:

1. Compressed gases, hydrogen and oxygen, enter digitally controlled mass flow controllers; type Brooks 5850S, and flow through 1/4" copper tubing to the gas humidifiers.
2. The hydrogen and oxygen gas-flow can be stopped by valves for purging the anode and cathode sides with nitrogen in an emergency situation.
3. The gases are passing through manual flow-meters for extra manual flow-control. Nitrogen gas-flow for purging is only controlled with these controllers.

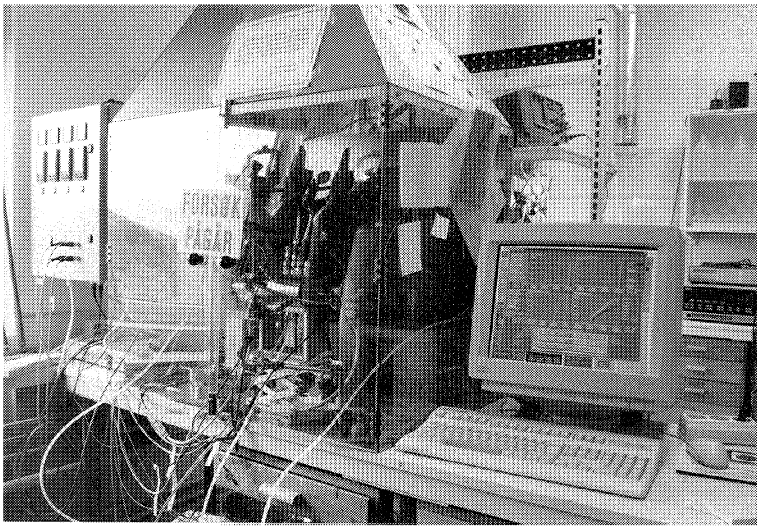

Figure 2.4: The test-station in 2000. In the centre of the picture, slightly to the left, the fuel cell housing and humidifiers are situated in a hood. The temperatures are controlled from the box to the left. The computer is situated to the right. All the instruments are placed in a rack behind the test-station to avoid water-spilling and instrument malfunction.

4. The feed gas pressures are monitored with a pressure gauge.
5. The gases enter two gas humidifiers. The temperatures of the humidifiers can be controlled independently. These humidifiers are new, and will be described in section 2.3.1.
6. Finally the gas enters through 1/4" Teflon tubing to the fuel cell under test in the new fuel cell housing. The fuel cell housing is described in section 2.2.
7. The exhaust gases from the fuel cell enter two separate water condensers. The condensers are described in section 2.3.2.
8. The gases from the condensers enter pressure control valves from Brooks (model 5866). The valves are controlled digitally from the computer.
9. At last, the exhaust gases exits through the ventilation system.

2.3.1 The gas humidification system

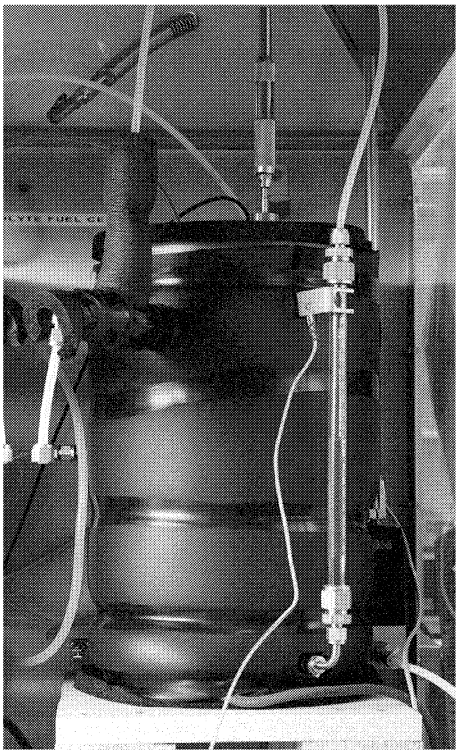

Figure 2.5: The new gas humidifier. The glass tube in front is designed for measuring the water level in the internal water container, and as a point for refilling water. The whole system is thoroughly insulated.

The new gas humidifiers (figure 2.5) are based on the same principle as the humidifiers developed by Møller-Holst [1996b]. Dry gas is bubbled through water at a given temperature. Saturation of the gases at the given humidification temperature is assumed. To obtain a stable humidification, the dry gas is pre-heated in a stainless steel tube coil. Then the gas is finely dispersed through a glass-sieve to obtain small gas bubbles that will fast obtain saturation with water. Finally, the gas leaves the humidifier in a downward direction, so that all the water vapour leaves the system, instead of condensing on a colder top-plate.

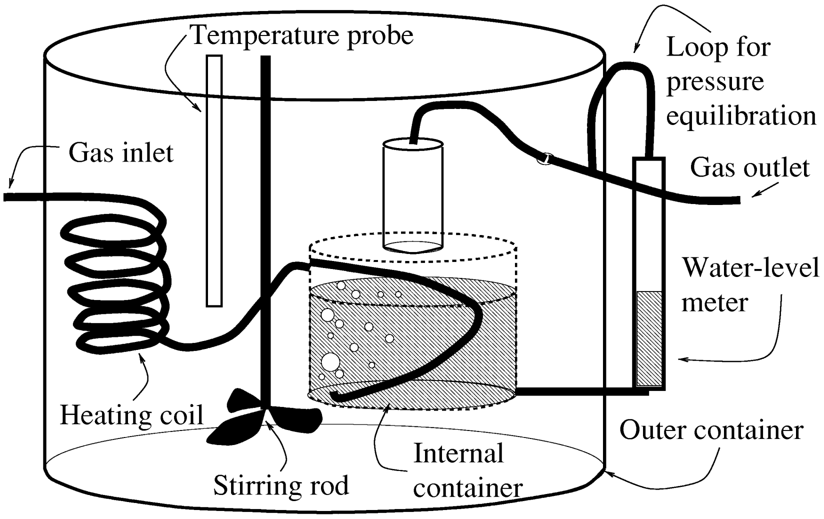

Figure 2.6: A sketch of the new gas humidifier. The drawing is not to scale. The outer container has a volume of 10 l. The inner container has a volume of 800 ml. All fittings are Swagelok fittings. The fittings for the water-level meter in glass were special made from the workshop at NTNU.

These requirements for the fuel cell humidification system is solved by having an internal water-filled bubble container inside a larger container, also filled with water. The outer container is heated by electrical heating tape, and the temperature of the outer water-bath is controlled by a PID-controller (Eurotherm 2408[1]) and a Pt-100 thermistor. A stirring rod can be inserted to obtain a more homogeneous water temperature in the outer container. The outer container has a volume of approximately 10 l. The inner container has a volume of 800 ml and is filled through an external glass-tube, which also works as an internal water-level meter. The humidifier was thoroughly tested by Heldal [1999]. He found that the actual water content varied within ± 10 % from the calculated water content. This error could be due to errors in the digital mass-flow controllers at low flow-rates or inaccurate temperature measurements.

---

[1] Eurotherm A/S, Postboks 227, NO-1326 Lysaker

2.3.2 The water condensers

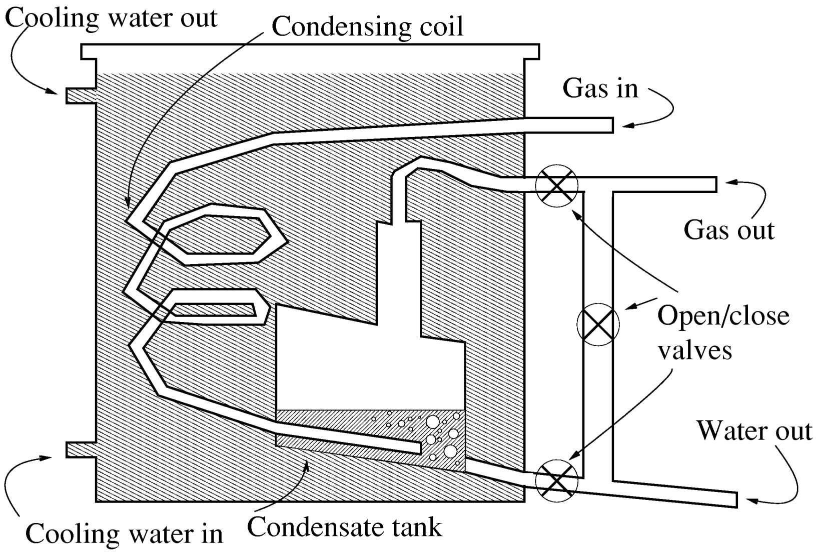

Figure 2.7: A schematic sketch of the water condenser. The drawing is not in scale. The outer container has a volume of approximately 10 l. The condensate tank has a volume of 500 ml. All fittings are Swagelok fittings, and the tubing are 1/4" and 1/2" SS-316 tubing.

The water condensers are designed to remove water by condensing the water in the gas flow, see figure 2.7. The condensers are able to operate pressurised, and the condensing medium is tap-water with a temperature of 5 - 8 °C. The vapour pressure of water at these temperatures is very low. To obtain higher accuracy, when measuring the net water transport through the membrane, the water leaving the condenser can be calculated. The condensers were tested by Heldal [1999]. He found them to work satisfactory for gas flow-rates up to 500 mlN/min.

2.4 Conclusion

The polymer fuel cell test-facility at Department of Chemistry has been optimised. A new fuel cell housing was designed and built, enabling measurements of local fuel cell temperatures. The fuel cell voltage is measured between the gas diffusion backings using thin platinum wires. This assures that the true fuel cell voltage is measured. New gas humidifiers were built assuring a water content within ± 10 % of the theoretical water content.

Chapter 3

Electrode optimisation

3.1 Introduction

The performance of the polymer electrolyte fuel cell (PEFC) has been significantly improved during the last decade, mainly through enhanced electrode properties and development of new membranes. Due to the complexity of the PEFC electrode, a systematic approach to electrode optimisation is desirable and advantageous, as shown in a recent study by Møller-Holst [1996a]. Experiments based on factorial design require fewer runs per factor studied, provide easy result evaluation and are advantageous for modelling purposes. Surprisingly few studies applying this powerful tool have been reported. In this work a statistically designed experiment was used to evaluate the effect of changes in the electrode composition on fuel cell performance. Preliminary results from this study were reported previously [Vie and Møller-Holst, 1998].

Acetylene Black (AB) (Shawinigan^{TM}, E-TEK Inc.) is a type of carbon with a very high electronic conductivity. Its introduction into porous carbon PEFC electrodes was suggested by Mosdale and Stevens [1993] and was later successfully implemented by Uchida et al. [1995]. Therefore, addition of Acetylene Black to the catalyst layer was chosen as the first factor to be studied in this work. Acetylene Black was substituted for a low percentage of the catalyst material (Pt on Vulcan XC72, E-TEK Inc.), both having a Pt-loading of 20 wt%. Previous experiments [Møller-Holst, 1996a] have shown improved cell performance when the amount of Nafion$^{®}$ in the catalyst layer was increased from 15 to 25 %. Thus the effect of the Nafion content in the electrode was chosen as the second factor. In this work the Nafion content was varied in

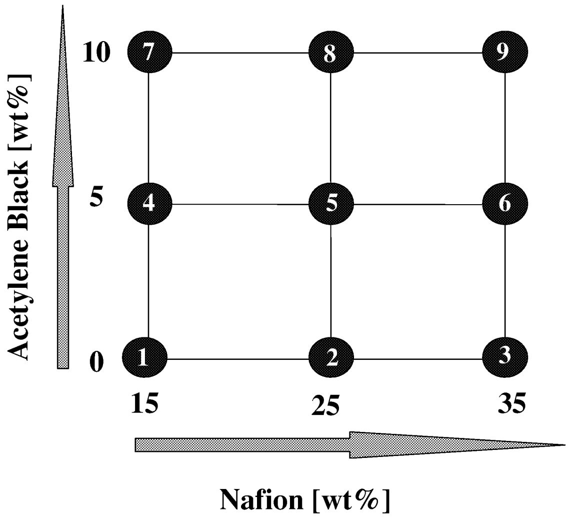

Figure 3.1: A schematic representation of 9 different compositions arranged as a 3^2-experiment. Each of the 9 cells are assigned a number from 1 to 9.

the range from 15 to 35 wt%. These two factors were each given three levels, forming a 3^2-factorial experiment [Box et al., 1978], as shown in Figure 3.1.

3.2 Experimental

The catalyst materials (20 % Pt on Vulcan XC72 and Acetylene Black) were mixed with Nafion solution and solvents, as described by Wilson and Gottesfeld [1992]. The prepared slurries were sprayed directly onto the membrane followed by drying in a hot-convection oven at 125 °C [Møller-Holst, 1996a], giving an active cell area of 5 cm^2 with a catalyst loading of 0.1 mg Pt/cm^2 ± 5 %. The Nafion 117 membrane was used throughout this study. Gas diffusion backings from ETEK[1] were contacted with the prepared membrane and electrodes and assembled in the fuel cell test facility described in chapter 2.

The cell break-in procedure included an initial step of switching the gases (from H_2 to O_2 and vice versa) on the electrodes 8-10 times, keeping the voltage at 0.2 V for 5-10 minutes each time. This reversing of the fuel cell

---

[1] ETEK Elat® double-sided, carbon only

(periodically using the anode as cathode and the cathode as anode) may speed up the activation process and shorten the break-in time. The cells were run at 0.2 V for 48 hours prior to electrochemical characterisation, to achieve stable performance. Each cell was characterised several times to confirm that it had reached maximum performance and that the performance was reproducible. An improved version of a fully automated test-station developed by Møller-Holst [1996b] was used for the electrochemical characterisation of the fuel cells. The test facility is described in chapter 2. All cells were characterised by obtaining polarisation curves at atmospheric gas pressures and gas flow rates of 0.3 l_N/min, corresponding to a maximum gas conversion of 5 %. The cell temperature was 70 °C, and the reacting gases (H_2 and O_2) were humidified at 80 °C.

3.3 Results and Discussion

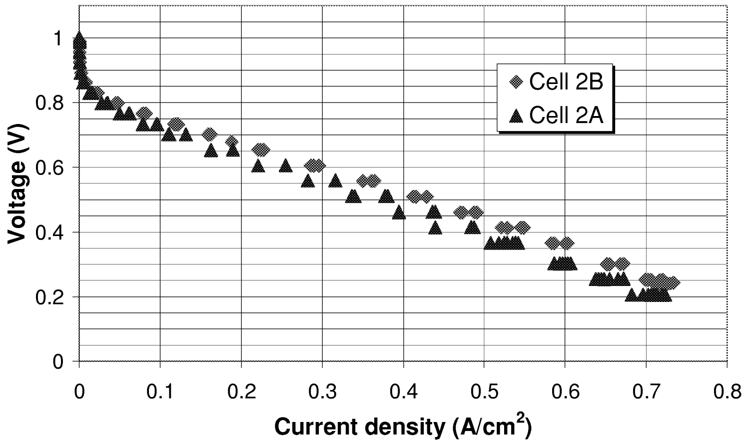

Figure 3.2: Polarisation curves for two identical cells (2A and 2B). The reproducibility is in agreement with previous results [Møller-Holst, 1996b]

A total number of 12 cells were studied, including one replicate of cells 2,5 and 7 (see figure 3.1). The polarisation curves for cell 2 and its replicate are shown in figure 3.2. The reproducibility was in agreement with previously reported results for the same experimental setup [Møller-Holst, 1996b]. Due to the low number of replicates we will disregard coupling effects (interactions) of Nafion and Acetylene Black, and analyse the results only with respect to the two main factors; i.e. the Nafion and Acetylene Black contents in the catalyst layer.

3.3.1 Qualitative assessment of the polarisation curves

Based on the results for 9 cells and their replicates (figure 3.3), the effect of variations in Nafion and Acetylene Black contents on cell performance was evaluated. From figure 3.3 it can be seen that cells 3, 6 and 9 show better performance than the other cells. These three cells have all a Nafion content of 35 wt% in the catalytic layer. This indicate that the proton conductivity of the catalyst layer might constitute a bottle-neck limiting the reaction rate and hence the fuel cell performance. Cells 1 and 4, both 15 wt% Nafion, show very poor performance, whereas cell 7, also 15 wt% Nafion, performs around average.

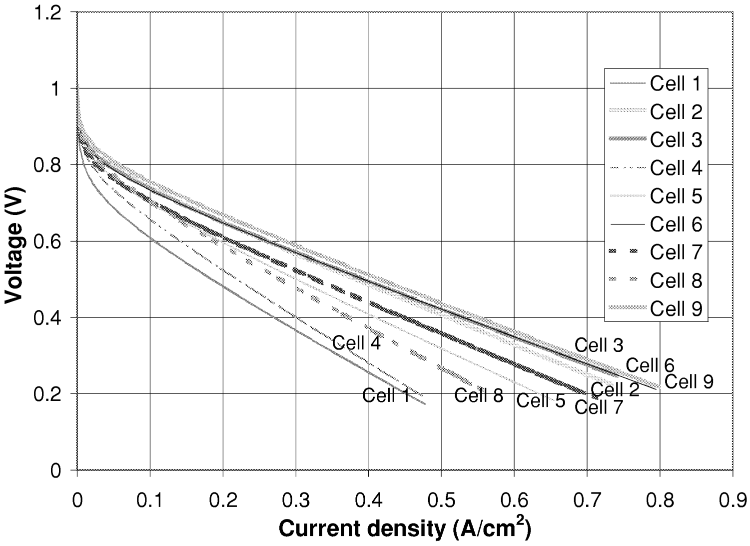

Figure 3.3: Polarisation curves for all tested cells, fitted to a Tafel-type model (equation (3.1)). An average is reported for the reproduced cells.

The effect of adding Acetylene Black to the catalytic layer is not easily distinguishable. Cells with a given AB composition, e.g., 7, 8 and 9 (all 10 wt%

AB) are more or less randomly distributed in the result range (Figure 3.3). The results are similar for 0 and 5 wt% Acetylene Black, and, thus, no clear trends are seen. This indicates that addition of Acetylene Black had a small or negligible effect on cell performance.

3.3.2 Quantitative analysis by the Bootstrapping method

The polarisation curves have a typical Tafel-type exponential form, including both current density (ohmic resistance) and the logarithm of the current density terms (activation losses):

$$E = E^0 - b \ln j - rj \tag{3.1}$$

Both terms cannot follow a statistical normal distribution. This makes it generally difficult to apply ordinary statistics to obtain error estimates. To assess the significance of the difference in cell performance, a statistical approach called "Bootstrapping" was applied [Efron and Tibshirani, 1993].

Bootstrapping [Efron and Tibshirani, 1993] is a method from which statistical distributions can be generated, based on the observed polarisation curves. The distributions can then be compared and the significance of the two main effects can be determined. All the data for a given level of one factor e.g., 15 wt% Nafion was congregated into one data-set, i.e., data for cells 1, 2 and 3 were merged. Half the data points were picked out randomly and fitted to a Tafel-type exponential model (equation (3.1)). A high number (1000) of such model curves were generated and from these curves a statistical distribution was formed. This distribution represented a confidence interval for the mean polarisation curve for the cells with a given amount of Nafion or AB in the catalyst layer. The calculations were performed using Matlab® software [MathWorks, Inc., 2002].

The generated curves for 15, 25 and 35 wt% Nafion are shown in figure 3.4 and from these ensembles of curves, significance levels for the data may be determined. From the figure it is clearly seen that increasing the Nafion content of the catalyst layer improved cell performance. The effect of increasing the Nafion content from 15 to 35 wt% constitutes about 110 mV at 0.3 A/cm^2 and 130 mV at 0.6 A/cm^2. The calculated distributions at current densities of 0.3 A/cm^2 and 0.6 A/cm^2 are shown in Figure 3.5. No overlap is seen and, thus, we can conclude that the average polarisation curves are significantly different.

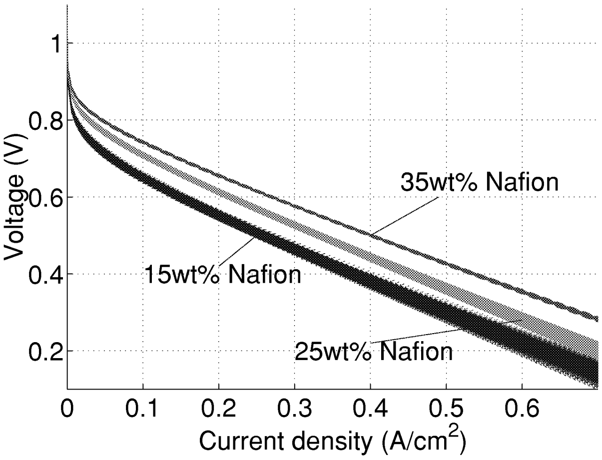

Figure 3.4: Distribution of polarisation curves calculated with the Bootstrapping method obtained for different levels of Nafion, averaged over the different Acetylene Black contents.

A similar enhanced fuel cell performance is confirmed by Antolini et al. [1999] and by Passalacqua et al. [2001]. They both report an optimal Nafion content of 33 wt%. The increased fuel cell performance might be due to:

- Increased protonic conductivity in the catalyst layer
- Enhanced contact between the active catalyst layer and the membrane phase
- Increased three-phase area

The main difference in figure 3.4 is seen in the activation region of the polarisation curves i.e., at low current densities. This indicates that variations in Nafion content largely influence the three-phase area and protonic conductivity of the catalyst layer and probably also improve the contact between membrane and catalyst layer.

The Bootstrapping method was also applied to all cells with 0, 5 and 10 wt% Acetylene Black, respectively, and the generated polarisation curves are shown in Figure 3.6. Substantial overlap between the curves is observed. In Figure 3.7 the calculated distributions are shown at current densities of 0.3 A/cm^2 and 0.6 A/cm^2, respectively. From these curves, we can clearly

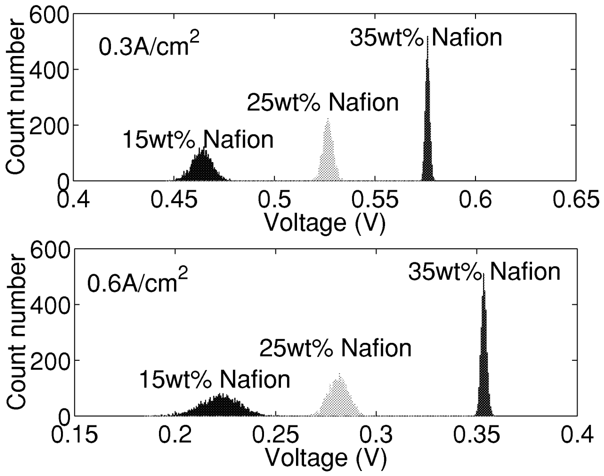

Figure 3.5: The distribution of cell voltages at 0.3 A/cm^2 and 0.6 A/cm^2, showing significant difference for the different Nafion contents.

see the overlap between the different distributions for the different contents of Acetylene Black. At 0.3 A/cm^2 the overlap is complete for 0 and 10 wt% AB, whereas at 0.6 A/cm^2 the distributions are somewhat separate. At lower current densities (not shown) 0 wt% totally overlaps 5 wt%. This means that the average polarisation curves for 0, 5 and 10wt% Acetylene Black are not significantly different. We can therefore not conclude that there will be an effect of adding Acetylene Black to the catalytic layer in the polymer fuel cell.

The curves indicate that 10 wt% Acetylene Black has the best performance at low current densities, and, thus, that AB enhances the activation limited oxygen reduction reaction. This is in contrast to Gojkovic et al. [1998], who states that the type of carbon does not affect the O_2 reduction reaction. At higher current densities, however, the cells with 0 wt% AB show the best performance. Acetylene Black is, according to Mosdale and Stevens [1993], a type of carbon with a very high conductivity and should therefore reduce the ohmic resistance in the catalyst layer. This is confirmed by Jordan et al. [2000]. They show that addition of Acetylene Black to the diffusion layer next to the catalytic layer enhances the fuel cell performance. This may be in contradiction to the results obtained in our study. But, one should note that the diffusion layer and the catalytic layer have completely different functions and their thickness differ by 1 to 2 orders of magnitude (5 - 10 μm versus 100

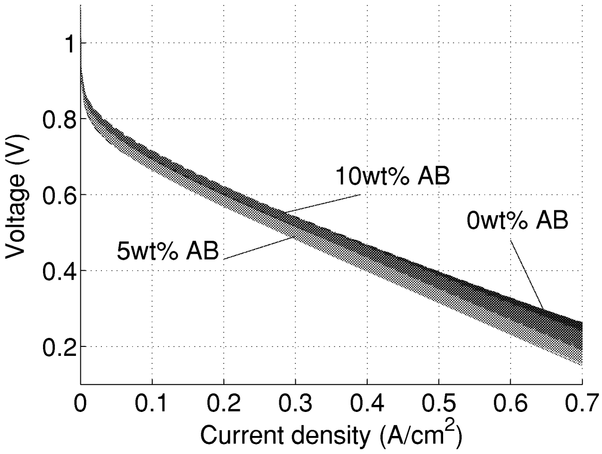

Figure 3.6: Distribution of polarisation curves calculated with the Bootstrapping method obtained for different levels of Acetylene Black, neglecting the effect of variation in the Nafion content.

- 200 μm). If there is any significant effect at all, it seems that an increased amount of AB increases the resistance of the catalyst layer. There might also be small contributions from diffusion limitations, due to variations in catalyst layer morphology, that shifts the picture and alter these conclusions. Smaller particles may increase the layer density, and hence augment diffusion limitations. It should be pointed out that these effects are small and within the reproducibility of the results.

These results indicate that there are other processes than the electronic conductivity of the catalyst layer that constitutes the bottle neck in the complex and inter-related transport and reaction processes that occur in these fuel cells.

3.4 Conclusions

Substitution of up to 10 % of the catalyst layer carbon (Vulcan XC72) by Acetylene Black gave no significant change in cell performance. Hence electronic conductivity of the catalyst layer is not a bottle-neck in the polymer electrolyte fuel cell. Increasing the Nafion content from 15 to 35 wt% had a considerable positive effect on cell performance, mainly attributed to increase in three-phase area and enhanced contact between the catalyst layer and the

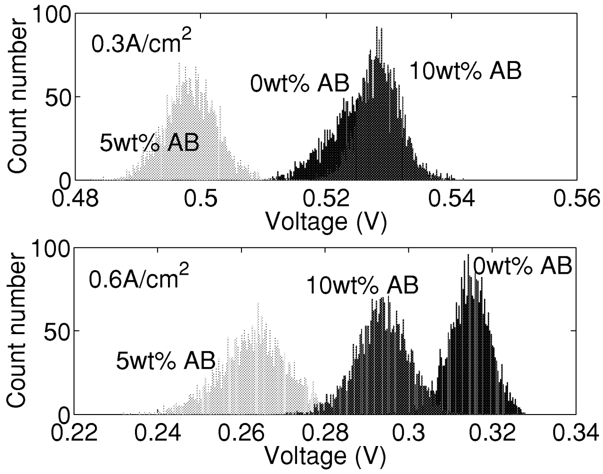

Figure 3.7: The distribution of cell voltages at 0.3A/cm^2 and 0.6A/cm^2, showing overlap for the different Acetylene Black contents.

membrane phase. This result is in accordance with other results in the literature [Antolini et al., 1999; Passalacqua et al., 2001]. Bootstrapping was shown to be a useful statistical method to obtain estimates for distributions around mean values and for interpretation of the results. Factorial design was shown to be a viable tool in the optimisation of the electrode composition in the polymer electrolyte fuel cell.

Acknowledgements

Monica Strømgård is acknowledged for the laboratory testing. Martin Høy is thanked for assistance with the statistical analysis.

Chapter 4

Testing of new membrane types

In this chapter a paper in press in Journal of Membrane Science is presented. The title of the paper is: “Fuel cell Performance of Proton Irradiated and Subsequently Sulfonated Poly(vinyl fluoride) Membranes”. The authors of this paper are:

- Preben J.S. Vie and Monica Strømgård [1]
- Eero Rauhala [2]
- Mikael Paronen and Franciska Sundholm [3]

In the paper results are given on testing of a novel type of membrane in the polymer electrolyte fuel cell.

Abstract

Proton irradiated and sulfonated poly(vinyl fluoride), PVF-SA, membranes have been tested with respect to fuel cell performance and swelling in water. Swelling of the PVF-SA membranes was clearly lower than that of the Nafion® 117 and 112 membranes. In fuel cell tests the performance of the low price PVF-SA was better than Nafion 117 membranes tested under similar conditions. In contrast, the Nafion 112 membrane performed better than the

---

[1] Department of Chemistry, NTNU, NO-7491 Trondheim,NORWAY

[2] Accelerator Laboratory, University of Helsinki, PB 43, FIN-00014 HY, FINLAND

[3] Laboratory of Polymer Chemistry, University of Helsinki, PB 55, FIN-00014 HY, Helsinki, FINLAND

PVF-SA membrane. The low ohmic resistivity of Nafion 112 and the compatibility between Nafion membrane and Nafion impregnated electrodes explain this. PVF-SA membranes suffered from degradation during the fuel cell testing.

4.1 Introduction

Ionic conductivity of polymer electrolyte membranes (PEM) has been shown to be higher in materials which contain phase separated structures and ion aggregates than in homogeneous materials [Kreuer et al., 1995; Paronen et al., 1999]. An example of this kind of material is Nafion® which contains ion aggregates of the size of 3-5 nm [Gierke et al., 1981]. If a PEM is made by sulfonation of polymer film, reorganisation of the sulfonic groups and formation of clusters are restricted by the mobility of the polymer chains. This reorganisation is dependent on crystallinity, glass transition temperature (T_g) and cross-linking density of the polymer matrix. Through a styrene grafting and sulfonation method this problem is avoided due to the tendency of phase separation of the grafted poly(styrene) chains [Hietala et al., 1999].

Direct sulfonation of fluoropolymer films is a new and attractive method for preparation of proton conductive membranes for fuel cells. In this method and with these materials the main problems are the lack of necessary phase separation and also difficulties in performing the sulfonation. Our approach to avoid these problems has been to use heavy charged particle irradiation. Heavy charged particles create more or less cylindrical tracks of radiolysis products when traversing through the material. The diameter of the cylindrical zone of radiolysis products is dependent on the particle, but it is generally in the range of 1 to 6 nm [Waligórski et al., 1986]. The size of this modified zone is thus comparable to the size of the ion clusters found in Nafion [Gierke et al., 1981]. Radiolysis products formed along the tracks of the traversed particles are, e.g., radicals, conjugated structures, ions and volatile compounds [Chapiro, 1962] in addition to some physical changes like formed microvoids [Besmann and R.Greer, 1975]. Some of these changes can be utilised further in the functionalisation reactions. This approach was thus used in our work where the direct sulfonation of poly(vinyl fluoride) was performed. The water uptake, ion exchange capacity and ion conductivity of this material were shown to be improved if the original material was irradiated with energetic protons prior to the sulfonation, compared to the respective values of the samples irradiated with electrons [Paronen et al., 1999, 1997; Ostrovskii et al., 1999]. Regarding the ion conductivity, values of around 20 mS/cm have been achieved with proton irradiated samples. In contrast, the ion conductivity of both the non-irradiated and electron beam irradiated PVF-SA membranes have been less than 6 mS/cm [Paronen et al., 1997]

We present here the first fuel cell test results of the proton irradiated and subsequently sulfonated PVF membranes. Several membranes were tested until failure of fuel cell function. A comparison with respect to performance is made with commercial Nafion 117 and 112 membranes (DuPont) tested under similar fuel cell conditions.

4.2 Experimental

4.2.1 Membrane preparation and characterisation

The first step of the membrane preparation was irradiation of the PVF films (Tedlar, DuPont), thickness 50 μm and 25 μm with respectively 5 MeV or 2.5 MeV protons under vacuo with the absorbed dose of 400 kGy. A detailed description of the irradiation is given elsewhere [Paronen et al., 1997]. After this the membranes were sulfonated with chlorosulfonic acid (1.5 vol-% in 1,2-dichloroethane). Sulfonation time of the thicker membrane was 120 min whereas the thinner membrane was sulfonated for 85 min. After sulfonation the samples were purified with different solvents (1.2-dichloroethane, tetrahydro furane, distilled water). Finally, the samples were kept in 3% H_2O_2 for 8 h to convert all the sulfur functional groups to sulfonic acid functionality [Ostrovskii et al., 2001].

Membrane swelling both with respect to water uptake and dimensional changes were analysed. Drying of the membranes was done by keeping the samples in a vacuo desiccator at 65 °C for 24 h. Hydration of the samples was done by boiling the samples for 1 h in distilled water followed by storing at room temperature for 24 h. Changes in thickness and dimensions along the surface were measured from samples of size 0.5 cm · 4.0 cm. With each of the analysed samples, 3 or more parallel analyses were performed.

4.2.2 Fuel cell tests

The membranes were tested in an improved version of the fully automated fuel cell test-station developed by Møller-Holst [1996b]. A pneumatic cylinder was attached to one side of the cell fixture, ensuring a reproducible mechanical pressure over the Membrane and Electrode Assembly (MEA). This is a very important parameter since the performance of the MEA and consequently of the whole fuel cell is dependent on the contact within the MEA, which in turn is significantly dependent on the applied mechanical pressure. In addition, problems arising from possible lack in mechanical strength of the membranes can be avoided better during the test procedure by means of precise gas pressure control. The overall structure of one half of the fuel cell test fixture is shown in figure 4.1.

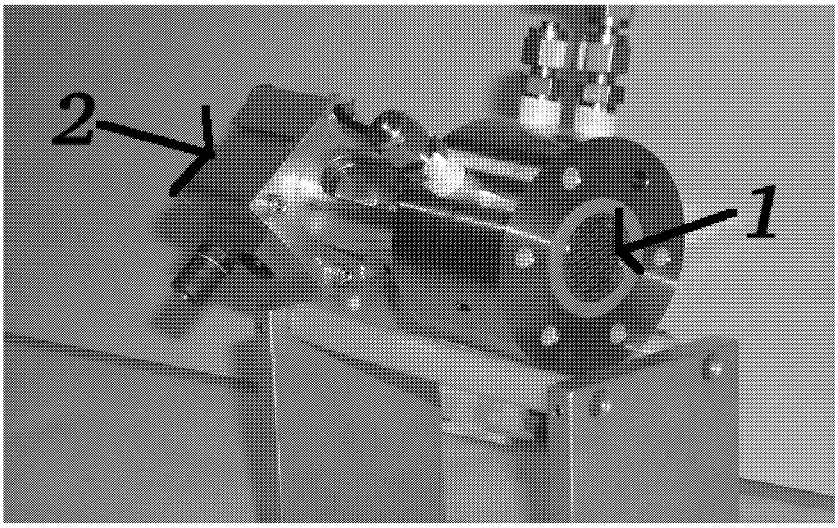

Figure 4.1: Photograph of one half of the fuel cell housing. The MEA is placed in contact with the piston at 1) and a similar piston in the other half. The pneumatic cylinder at 2) controls the mechanical pressure over the MEA.

The temperatures of the cell and humidified gases were controlled and were varied from 30 to 80 °C. Temperatures of the humidified gases (hydrogen and oxygen) were kept approximately 10 °C over the temperature in the fuel cell. The total cell area was 4.9 cm^2. All electrodes were commercial E-TEK Elat®/STD electrodes with 20% Pt/C and a Platinum loading of 0.5 mg Pt/cm^2. A 5% Nafion solution was sprayed on the electrode surface, to give a Nafion loading of 0.6 mg/cm^2. This procedure will increase the performance of the electrode and increase the ionic contact between layers in the MEA. The electrodes were then simply contacted with the proton conductive membrane, and inserted into the fuel cell housing.

4.3 Results and discussion

Two different types of sulfonated PVF membranes have been tested in a fuel cell. One type of PVF membrane was based on originally 50 μm thick PVF and the other on 25 μm thick film. The films were otherwise essentially the same except the thickness. Analysed properties of the membranes are given in Table 4.1. The respective values for both Nafion 117 and 112 are also given.

Table 4.1: Selected properties of the tested membrane samples. The values given for changes in both X and Y directions along the surface are defined as percentages of the respective length in wet state. The thickness of the membrane is denoted d_{mem}. The conductivity in the membrane, σ, was measured at ~50 °C.

Sample	d_{mem} (dry state)	Ion exchange capacity	σ	Water uptake		Dimensional changes upon dehydration		
					(λ)	d_{mem}	X	Y
	[μm]	[meq/g]	$\left[\frac{mS}{cm}\right]$	[g/g] ±0.03	$\left[\frac{n_{H_2O}}{n_{SO_3H}}\right]$	[μm] ±2	[%] ±2	[%] ±2
PVF [25μm]	27±2	1.5±0.2	5±1	0.20	7±1	-2	91	94
PVF [50μm]	60±2	1.5±0.2	5±1	0.20	7±1	-4	93	95
Nafion 117	175±2	0.9±0.1	29±4	0.32	21±2	-32	83	87
Nafion 112	55±2	0.9±0.1	20±4	0.32	21±2	-5	82	85

Ion exchange capacity of the PVF-SA membranes is determined by the sulfonation time and concentration of the sulfonation reagent. In this work these variables were chosen so that the sulfonation profile across the membrane was relatively even but simultaneously, the overall ion exchange capacity was as low as possible. A low ion exchange capacity will give better mechanical properties. In practice, sufficient homogeneous distribution of the sulfonation across the membrane demanded such a heavy sulfonation that the ion exchange capacities of the PVF-SA membranes were almost twice as high as of the Nafion membranes. Despite this, the water uptake of the PVF-SA membranes was clearly lower than for the Nafion membranes. Due to the lower water uptake also the dimensional changes upon hydration were lower.

The difference in swelling between the Nafion membranes and sulfonated PVF can be explained by several factors. The molecular structures of both types of membranes can be considered to be similar with respect to the interaction of water with the polymer backbone. Both polymers are based on highly hydrophobic backbones, which does not interact directly in the swelling. However, the crystallites possibly present in the hydrophobic phase can limit the swelling because crystallites work as cross-linking points. The crystallinity of the membranes has a minor effect in this study, however, as the crystallinities of Nafion and sulfonated PVF-SA membranes are almost the same [Gruger et al., 2001; Paronen et al., 1999]. The membrane swelling can be expected to be dependent also on the polymer's glass transition temperature. For the hydrophobic part of Nafion, which is essentially similar with PTFE, the T_g is -73 °C, but for pure PVF the T_g is 41 °C [Brandrup et al., 1999]. This difference can thus explain partially the different swelling behaviour of the membranes. The extent of cross-linking is also different. The original PVF film used in this work is based on a linear polymer, but the irradiation treatment creates cross-linking [Wall et al., 1966]. In addition, the sulfonation can produce cross-linking due to the formation of sulfonate bridges [Gilbert, 1965]. In contrast to this, Nafion is not a chemically cross-linked matrix. The organisation of the sulfonic acid groups may also be important in the wetting of the polymer. It is well accepted that the sulfonic acid groups form cluster structures and networks in Nafion membranes [Gierke et al., 1981]. In contrast, such structures do not exist in the sulfonated PVF membranes [Paronen et al., 1999]. Unfortunately, we did not have any possibilities to test and could not either find any information on the swelling effect of the arrangement of the acid groups. Finally, mechanical stress affects swelling of the matrix. The original PVF-film may have significant mechanical stress arising from the film processing. In addition, stress is induced by swelling during the sulfonation. This can create high and permanent mechanical stress into the membranes as no solvents for the hydrophobic part of the membranes are in contact with the membranes. Significant stress can therefore exist in the final membranes, which in turn limits the swelling. Of these alternative explanations we believe that the main reasons for the low swelling of PVF-SA are due to higher T_g of the hydrophobic matrix, cross-linking of the polymer matrix and the mechanical stress.

The conductivity of the fuel cell membrane at 50 °C was calculated from polarisation curve data presented in figures 4.2 (PVF-SA 50 μm) and 4.3 (PVF-SA 25 μm, Nafion 117 and Nafion 112). The linear parts of the polarisation curves were fitted to linear regression models. The respective slopes represent the total ohmic resistance in the fuel cells. Under the assumption that most ohmic resistance is due to the membrane resistance, a conductivity of the hydrated fuel cell membrane was calculated. The conductivity of Nafion 117 was measured by Springer et al. [1991] at varying temperatures and water contents in the membrane (λ). At 50 °C and $\lambda = 14$ the conductivity was calculated to 89 mS/cm. ($\lambda = 14$ corresponds to a Nafion 117 membrane in equilibrium with a gas with 100 % relative humidity.) The lower conductivity for Nafion 117 presented in table 4.1 can be explained by an additional resistance introduced by the fuel cell electrodes and gas diffusion backings, in addition to a possible lower water content (λ) in the membrane. The calculated conductivity for the 50 μm PVF-SA membrane is not directly comparable with the other conductivities due to other test conditions. The most important factor is the different mechanical pressure.

All PVF-SA membranes were tested in a fuel cell until fuel cell failure. The test time varied between 150 and 210 h. In all cases the failure was indicated by a sudden drop in the open circuit voltage (OCV). Inspection of the MEAs did always show cracks in the membrane. The position of the cracks was always outside the active electrode area, i.e. between the electrodes and the gas gaskets. During testing, the area in which failure occurred was continuously in contact with pure hydrogen and oxygen. The most probable reason for the rupture could therefore be either oxidation or mechano-chemical degradation of the membrane. Some of the tested PVF-SA samples were also analysed with FTIR. Fuel cell testing did not, however, bring any significant visible differences in the spectra. Further analysis of the degradation mechanism is under work.

On the basis of the extensive fuel cell testing of the PVF-SA membranes, the membranes are rather stable below 50 °C. However, at 70 °C the membranes ruptured rather quickly. The performance, i.e., voltage as a function of current density in the fuel cell with the PVF-SA membranes increased significantly throughout the testing periods but the increase was fastest during the first 2 days. This increase was clearly higher than the typical increase with Nafion membranes. The most probable explanation for this difference is based on the compatibility of the membrane with the electrode. With Nafion membranes, compatibility and consequently contact within the MEA is surely better due to the Nafion ionomer present in the catalyst. In contrast, PVF-SA membranes form a less compatible interface to the Nafion ionomer in the electrodes. Due to the applied mechanical pressure and fuel cell temperature, the contact between PVF-SA and Nafion in the catalyst layer becomes better with time. This results in a continuous improvement in fuel cell performance compared to Nafion membranes that tend to have a slightly reduced performance.

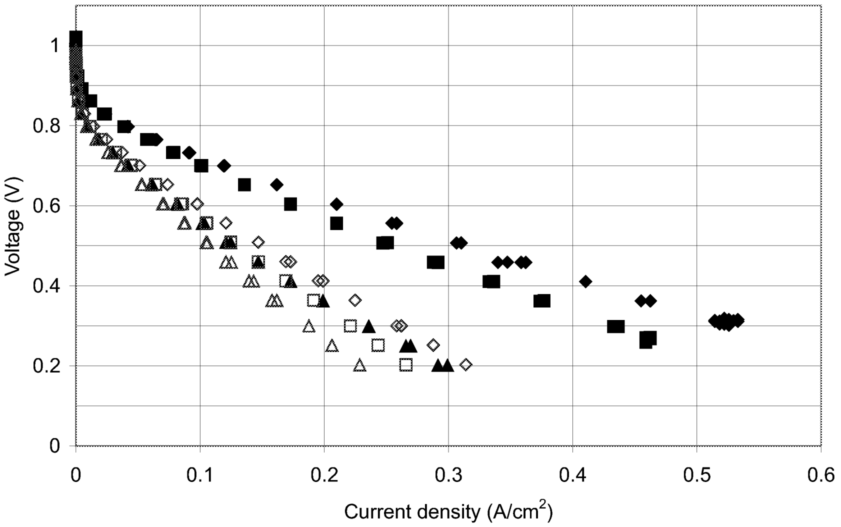

Figure 4.2: Polarisation characteristics of the tested membranes at different temperatures. Nafion 117: 30(△), 50 (□) and 70 (◇) °C; PVF-SA (50 μm) 30 (▲), 50 (■) and 70 (◆) °C. The gas pressures were 1 bara and the mechanical pressure 4.5 bara over the MEA.

During the testing we could not observe any measurable signs of degradation in the system, and the fluctuations in the observed voltages and current densities were small. We could observe increased performance when increasing temperature. This is as expected for polymer electrolyte fuel cells. A typical improvement in performance of the PVF-SA membrane based fuel cells with increasing temperature is shown in Figure 4.2. A comparison with Nafion 117 tested under similar conditions showed a better performance for the PVF-SA membrane. The difference could partially be explained by a smaller thickness for the PVF-SA membrane. The PVF-SA (matrix polymer 50 μm) membranes were about 60 μm thick and the thickness of Nafion 117 is about 175 μm. Thus, with thicker membranes we see a higher ohmic loss and consequently, poorer performance of the fuel cell. Another explanation is that the Nafion membrane was tested at a reduced mechanical pressure (4.5 bara) compared to normal testing conditions for Nafion membranes (10 bara). This gives an increased contact resistance and consequently a poorer performance. The calculated conductivity for Nafion 117 presented in Table 4.1 was therefore not based on this measurement.

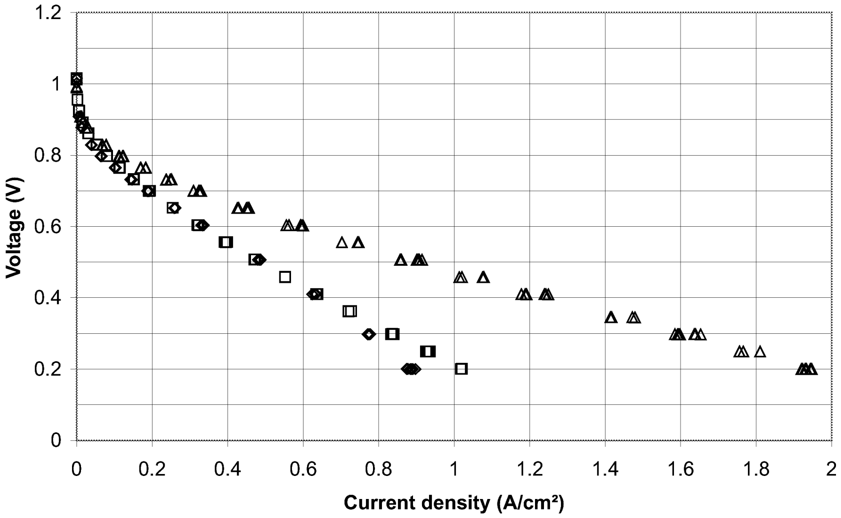

Figure 4.3: Polarisation characteristics of the tested membranes, PVF-SA (25 μm) (□), Nafion 117 (◇) and Nafion 112 (△), at close to optimal fuel cell temperatures for the PVF-SA membrane. The gas pressure was 2 bara and the temperatures varied slightly around 50 °C. The mechanical pressure was 10 bara.

Effects of the membrane thickness were also tested. Our aim was to observe the effect of membrane thickness on both fuel cell performance and fuel cell stability. A reduced thickness of the PVF-SA membrane from 50 to 25 μm did not pose any problems in the testing. The thinner membranes (Figure 4.3) were mechanically strong enough and thus did not rupture during the installation into the fuel cell fixture. Neither did an increased mechanical pressure compared to tests in Figure 4.2 cause any problems during testing. The measured OCV of the fuel cell with the 25 μm thick PVF-SA varied between 0.98 and 1.05 V during the test period. This OCV indicates that the gas permeation properties of PVF-SA membranes are suitable for PEMFC.

Polarisation curves measured with the 25 μm PVF-SA membrane are shown in Figure 4.3. Comparable polarisation curves for Nafion 117 and 112 membranes are also given. The performance of the PVF-SA membranes was slightly better than that of Nafion 117. In contrast, the performance of the PVF-SA (25 μm) membrane was lower than the tested Nafion 112 membrane (55 μm), despite the lower membrane thickness. This is caused by the higher ionic conductivity of Nafion (Table 4.1).

4.4 Conclusion

We have presented the swelling properties and fuel cell performance of the PVF-SA membrane. Despite the lower swelling upon hydration, PVF-SA membranes had a clearly lower fuel cell stability than Nafion membranes. In addition, the fuel cell performance of the PVF-SA was not yet as good as that of the Nafion 112. Despite this we consider the direct sulfonation method as a promising alternative for the preparation of proton conductive membranes. The preparation can be improved significantly, e.g., by the methods described below.

One of the key properties of the membranes with necessary ionic conductivity is the aggregation and phase separation of the sulfonic acid groups. This is easily achieved with materials which contain sulfonic acid groups or precursors of them during the film processing. With a grafting method the phase separation is also achieved easily due to the grafting kinetics. The situation with direct sulfonation is opposite. Without any control the sulfonation tends to proceed so that acid groups do not form the necessary clusters and aggregates. The results of this study show that necessary aggregation and consequently ionic conductivity can be achieved also in direct sulfonation by means of irradiation with heavy charged particles prior to sulfonation. In addition, mechanical strength of these membranes is initially good enough. As the mechanical strength is decreasing during fuel cell testing at higher temperature, there is a clear need for changing the matrix polymer or at least improving the sulfonation. Initial tests with fluorinated polymers with higher fluorine content show already now that some other polymers can be successfully used as matrix.

Acknowledgements

Funding from The Academy of Finland (MATRA), Svenska Tekniska Vetenskapsakademin i Finland r.f., the Nordic Energy Research Program (NEFP) and the Research Council of Norway is gratefully acknowledged.

Chapter 5

Polymer fuel cells described by irreversible thermodynamics

This chapter [Kjelstrup et al., 1999] was published as chapter 14 in [Sørensen, 1999]. A list of symbols specific for this chapter is included at the end.

Abstract

Irreversible thermodynamics for bulk systems and surfaces is applied to the solid polymer fuel cell. The cell is composed of three bulk phases (the membrane and the electrodes) and two membrane-electrode interfaces. The electric potential profile in the cell is calculated, using literature data for the membrane and the electrode, for the isothermal, isobaric single, polymer fuel cell. The overpotential is defined. The temperature profile compatible with the *emf* measurement, is given for electrode backing materials that are thermostated on the outside.

5.1 Introduction

Irreversible thermodynamics is a well established theory that describes transport in bulk systems, see *e.g.* de Groot and Mazur [1962]. When this theory is used to describe membrane transport, one has frequently assumed that there is equilibrium across the membrane-electrolyte interface (for a discussion, see Chapter 13 [Sørensen, 1999]). This assumption need not be fulfilled in practice, in particularly not in electrochemical systems, when there is an electrode attached to the membrane. When heat, mass and charge is transported across the membrane-electrode interface, the interface may have an energy which is different from the surroundings. Bedeaux and coworkers [Bedeaux et al., 1976; Albano and Bedeaux, 1987; Bedeaux, 1992] have extended the theory of irreversible thermodynamics so that it is capable of dealing with interfaces. Their theory introduces the surface or interface as a separate thermodynamic system following Gibbs [1961]. By allowing the interface to have its own thermodynamic variables, it becomes possible to describe interfaces which are not in equilibrium with adjacent bulk phases. The versatility of irreversible thermodynamics has thus been increased. Bedeaux and coworkers have since 1990 used irreversible thermodynamics for bulk systems and for interfaces to model heat and mass transport across liquid-gas interfaces [Bedeaux et al., 1990, 1992] and in electrochemical cells [Bedeaux and Ratkje, 1996; Ratkje and Bedeaux, 1996; Kjelstrup and Bedeaux, 1997].

The solid polymer fuel cell is today the most promising fuel cell for the transport sector, alone or in combination with batteries (hybrid engines). The cell produces electric energy from hydrogen and oxygen, usually between 70 and 90 °C. In the NECAR-model from Daimler-Benz, hydrogen is being supplied by water vapor reformation of methanol to a stack of fuel cells. Water is produced at the cathode, but must also be added to the anode at stationary state operation, to prevent the membrane from drying out. We shall study the energy conversion, and solve the coupled set of equations for heat, mass and charge transport in a one-dimensional single cell, using irreversible thermodynamics for the bulk parts of the cell [de Groot and Mazur, 1962] and for the electrode-membrane interfaces [Bedeaux et al., 1976; Albano and Bedeaux, 1987; Bedeaux and Ratkje, 1996; Ratkje and Bedeaux, 1996; Kjelstrup and Bedeaux, 1997]. We have chosen to illustrate the method by applying it to the solid polymer fuel cell, because of its future potential. The cell has been modeled extensively in the literature, and the description using irreversible thermodynamics can therefore be compared to well documented descriptions, for instance refs. [Springer et al., 1991, 1993].

There are three bulk parts in the single cell; the membrane and the backing materials for the electrode catalyst surface. There are two interfaces; the membrane-electrode interfaces between the backing materials and the membrane. The aim is to demonstrate irreversible thermodynamics for this heterogeneous system. This shall be done by a detailed calculation of the electric potential profile through the cell. The electric potential profile is also integrated to give the cell potential. From thermodynamic data for the electrode catalyst surface [Jerkiewicz and Zolfaghari, 1996; Zolfaghari et al., 1997; Vermeijlen et al., 1997], we estimate the *emf* of the isothermal, isobaric cell. The definitions of the anode and cathode overpotentials that follow from the theory are presented. We shall see that we can address also the pressure and temperature gradients in the cell.

5.2 System description

5.2.1 The membrane-electrolyte interface as a thermodynamic system

The membrane-electrode interfaces in the polymer fuel cell are illustrated in Fig. 5.1, see parts labelled 2. Both membrane-electrode interfaces are regions of about 10 μm thick between the carbon backing material and the polymer membrane. In this region one has three-phase contacts; because the electrode reaction requires contact between the electronic conductor (platinum on carbon), the ionic conductor (membrane), and the gas. We assume that the interface regions are electroneutral. Interface polarization, from excess protons and compensating negative charges in the metal, is possible, however. This membrane-electrode interface can be regarded as a thermodynamic system, separate from the adjacent membrane or electrode backing material (parts 1 and 3 in Fig. 5.1, respectively) according to Gibbs [1961]. The interface that we study is thicker than that Gibbs discussed, but this does not change the arguments for the method of treatment.

Gibbs introduced extensive variables of the surface as excess variables [Gibbs, 1961]. The excess internal energy of an interface is then obtained by integrating the internal energy across the interface and subtracting the extrapolated values of the internal energies of the adjacent bulk phases. Through such an integration procedure, we can obtain all excess densities per unit of interface area. These variables are denoted (s, a) and (s, c) in the present work; for the anode and cathode interface, respectively. The interface thickness of about 10 μm disappears as a variable by integration across the thickness. Gibbs [1961] places the excess densities of an interface on an equal footing with the bulk phase densities, in his discussion of thermodynamics of heterogeneous media. As a frame of reference for the fluxes into and out of the interface, we take the non-moving, equimolar surface of the Nafion membrane. This choice has the advantage that its location does not depend on the time in the experiment.

Existence of excess energy-, entropy- and mass densities, (u^s, s^s, n_i^s), implies that the surface also possesses its own temperature, $T^s = (\partial u^s/\partial s^s)_{n_i^s}$, and chemical potentials, $\mu_i^s = (\partial u^s/\partial n_i^s)_{s^s,n_j^s}$. The fundamental assumption in irreversible thermodynamics is that of local equilibrium [de Groot and Mazur, 1962]. By local equilibrium in an interface we mean that the normal thermodynamic relations are valid for the interface excess variables [Bedeaux et al., 1976; Albano and Bedeaux, 1987; Bedeaux, 1992]. An assessment of this assumption should be done on the basis of the results that can be derived from it. In the present context we shall use surface thermodynamic variables to derive expressions for the overpotential of the electrodes. The variables of the expression are accessible by experiments, which renders the results open to independent experimental tests.

5.2.2 Fuel cell processes

A schematic picture of the solid polymer single cell was shown in Fig. 5.1. We described the electrode-membrane interfaces above. These interfaces are the anode and the cathode of the cell, respectively. The electrolyte is a water-containing, proton-conducting membrane (part 1). The electrode backing on each side consist of porous carbon impregnated with Teflon (parts 3).

Hydrogen gas diffuses to the interface through pores in the anode backing, and produces protons by oxidation of atomic hydrogen adsorbed in the interface [Jerkiewicz and Zolfaghari, 1996; Zolfaghari et al., 1997; Vermeijlen et al., 1997]:

$$\frac{1}{2}\mathrm{H}_2(g,a) \rightarrow \mathrm{H}(s,a) \tag{5.1}$$

$$\mathrm{H}(s,a) \rightarrow \mathrm{H}^+(s,a) + e^-(s,a) \tag{5.2}$$

Here (g,a) denotes the gas phase in the pores close to the anode.

The membrane electrolyte contains between 10 and 15 molecules of water per ionic site [Springer et al., 1991]. Water must be supplied to the anode interface in order to prevent the membrane from drying out. In the stationary state there is a constant amount of water transported to the anode interface, calculated as t_w^a moles per Coulomb

$$t_w^a\mathrm{H}_2\mathrm{O}(g,a) \rightarrow t_w^a\mathrm{H}_2\mathrm{O}(s,a) \tag{5.3}$$

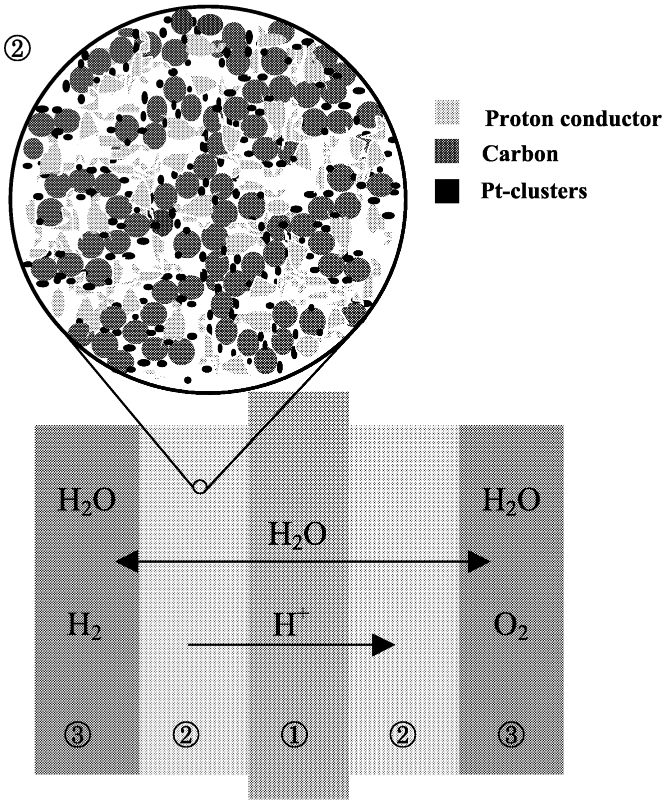

Figure 5.1: The symmetric cell arrangement. (1) denotes the membrane, (2) the electrode catalyst region (see insert) and (3) is the electrode backing material. Transport of protons is from left to right. Courtesy of Møller-Holst [1996b].

Proton conduction in the membrane electrolyte does not take place without water transport. The moles of water transported per Coulomb (the electro-osmotic effect) is t_w^m:

$$\mathrm{H}^+(m,a) \rightarrow \mathrm{H}^+(m,c) \tag{5.4}$$

$$t_w^m\mathrm{H_2O}(m,a) \rightarrow t_w^m\mathrm{H_2\ O}\ (m,c) \tag{5.5}$$

The side of the membrane facing the anode is denoted (m,a), while the side of the membrane facing the cathode is denoted (m,c).

At the cathode interface, protons react with adsorbed oxygen and produce water:

$$\mathrm{H}^+(s,c) + \frac{1}{4}\mathrm{O}_2(s,c) + e^-(s,c) \rightarrow \frac{1}{2}\mathrm{H}_2\mathrm{O}(s,c) \tag{5.6}$$

Oxygen gas migrates through the porous carbon backing on the cathode side:

$$\frac{1}{4}\mathrm{O}_2(g,c) \rightarrow \frac{1}{4}\mathrm{O}_2(s,c) \tag{5.7}$$

Water disappears from the cathode interface as vapor through the porous carbon:

$$t_w^c\mathrm{H}_2\mathrm{O}(s,c) \rightarrow t_w^c\mathrm{H}_2\mathrm{O}(g,c) \tag{5.8}$$

In the stationary state the amount of water vapor transported in carbon backing is t_w^c moles per Coulomb.

Diffusion in the carbon backing material is here taken to be fast. The Gibbs energy change of the cell reaction is normally written as:

$$\Delta_r G = \frac{1}{2}\mu_{H_2O}^{g,c} - \frac{1}{4}\mu_{O_2}^{g,c} - \frac{1}{2}\mu_{H_2}^{g,a} \tag{5.9}$$

Experience shows that not all of this chemical energy can be converted into electric energy, not even when very small currents are drawn from the cell. The ohmic losses in the cell are substantial for current densities of the order of 10^4 A/m^2. The overpotential, of the cathode mainly, reduces the cell potential similarly. It is one of the purposes of this work to describe interface potential drops and the anode and cathode overpotentials within the framework of irreversible thermodynamics. We shall thus locate, describe and explain the origin of the electric potential profile, as well as the sources of the dissipated energy. The temperature profile will also be discussed.

5.3 Conservation of charge, mass and energy in the interfaces and the bulk phases

The analysis of the system is restricted to stationary state conditions and transport in one direction only. The conservation equations of charge, mass and energy then take a simple form. It follows from electroneutrality that the electric current density j is constant throughout the cell. This is also true in the non stationary state if one uses the condition of charge neutrality. Polarization is usually small in bulk phases [de Groot and Mazur, 1962]. At an interface, one may not neglect the polarization. For a constant electric current, the interface polarization is constant, however.

Furthermore, the flux of hydrogen gas in the carbon backing on the anode side (a), and oxygen gas in the carbon backing on the cathode side (c) are constant and given in terms of the electric current density by:

$$2J_{H_2}^{a} = -4J_{O_2}^{c} = j/F \tag{5.10}$$

The water flux is constant in the carbon backing on the anode side and in the bulk membrane, continuous through the anode interface and given by

$$J_w^a = J_w^m \tag{5.11}$$

At the cathode interface, water is produced according to Eq. (5.6) so that the constant water flux in the carbon backing on the cathode side is given by

$$J_w^c = J_w^m + j/2F \tag{5.12}$$

The total energy flux J_e in the system (cf. de Groot and Mazur [1962] for a definition) is everywhere constant and continuous through the electrode interfaces. It is given in terms of the physical heat flux $J_q^{\prime i}$, where i= a (anode side) , m (membrane) *or* c (cathode side), in the bulk sections, and the comoving partial enthalpies of formation, and the electric current time the potential, ϕ:

$$\begin{aligned} J_e &= J_q^{\prime g,a} + J_{H_2}^{a} h_{H_2}^{g,a} + J_w^a h_w^{g,a} + j\phi^{g,a} = J_q^{\prime m,a} + J_w^m h_w^{m,a} + j\phi^{m,a} \\ &= J_q^{\prime m,c} + J_w^m h_w^{m,c} + j\phi^{m,c} = J_q^{\prime g,c} + J_{O_2}^{c} h_{O_2}^{g,c} + J_w^c h_w^{g,c} + j\phi^{g,c} \end{aligned} \tag{5.13}$$

The total energy flux, which must not be confused with the internal energy flux, is transformed partly into electric power through the reactions that take place in the membrane-electrode interfaces. The transformations in the interface are described in Subsections 5.4.2 and 5.4.3 below. In the carbon backing material on both sides, the gas fluxes, the water flux and the electric current density are constant. In the membrane, the water flux and the electric current density are constant. The enthalpies here depend on local densities and temperatures. Because the total energy flux is constant throughout, the often substantial changes of the enthalpies when we are crossing an interface, lead to corresponding changes in the measurable heat flux.

5.4 The entropy production rate and the flux equations

We consider transport per unit area in the x-direction across the membrane of a single cell, and start by finding suitable expressions for the entropy production rates. The frame of reference for the fluxes is the non-moving surfaces (the equimolar surface of Nafion).

5.4.1 The bulk phases

In the bulk membrane, there is transport of heat, water and charge (protons). In the carbon backing charge is transported as electrons. The transport of hydrogen on the anode side, and of oxygen on the cathode side are both given in terms of the electric current in the stationary state. These elements therefore need not be considered separately. Thus in all three bulk phases, the entropy production rate is according to de Groot and Mazur [1962]:

$$\sigma = J_q' \frac{d}{dx}(\frac{1}{T}) - J_w \frac{1}{T}\frac{d\mu_{w,T}}{dx} - j\frac{1}{T}\frac{d\phi}{dx} \tag{5.14}$$

where J_q' is the measurable heat flux, J_w is the water flux, and j is the electric current density. The conjugate forces of these fluxes are $\frac{d}{dx}(\frac{1}{T}) = -\frac{1}{T^2}\frac{dT}{dx}$, $-\frac{1}{T}\frac{d\mu_{w,T}}{dx}$, and $-\frac{1}{T}\frac{d\phi}{dx}$, where T is the temperature, $\mu_{w,T}$ the chemical potential of water at constant temperature and ϕ the (operational) electric potential that refer to given electrodes. The flux equations for the membrane are accordingly:

$$J_q' = -\frac{L_{qq}}{T}\frac{dT}{dx} - L_{qw}\frac{d\mu_{w,T}}{dx} - L_{q\phi}\frac{d\phi}{dx} \tag{5.15}$$

$$J_w = -\frac{L_{wq}}{T}\frac{dT}{dx} - L_{ww}\frac{d\mu_{w,T}}{dx} - L_{w\phi}\frac{d\phi}{dx} \tag{5.16}$$

$$j = -\frac{L_{\phi q}}{T}\frac{dT}{dx} - L_{\phi w}\frac{d\mu_{w,T}}{dx} - L_{\phi\phi}\frac{d\phi}{dx} \tag{5.17}$$

where L_{ij} are Onsager coefficients, and $L_{ij} = L_{ji}$ holds, see ref. [de Groot and Mazur, 1962]. The coefficients contain a factor $1/T$ from the forces.

In the pores of the carbon backing, we have transport of heat and gas, and in the carbon itself, electric charge is transported. We have assumed, as a first approximation, that diffusion of hydrogen and of oxygen are fast, or that their chemical potential gradients are zero. We could in principle make the same approximation for the chemical potential of the water in the carbon backing. This reduces the set to two equations for J_q' and j. As we have to take J_w along in the membrane, we give the more general form for all three bulk phase, rather than giving specialized expressions for each bulk phase separately.

By solving the last equation for $d\phi/dx$, we can write the constitutive equations in the following form

$$\begin{aligned} J_q' &= -\lambda\frac{dT}{dx} - l_{qw}\frac{d\mu_{w,T}}{dx} + \pi j && (5.18) \\ J_w &= -\frac{l_{wq}}{T}\frac{dT}{dx} - l_{ww}\frac{d\mu_{w,T}}{dx} + t_w j && (5.19) \\ \frac{d\phi}{dx} &= -\frac{\pi}{T}\frac{dT}{dx} - t_w\frac{d\mu_{w,T}}{dx} - rj && (5.20) \end{aligned}$$

Here $\lambda = (L_{qq} - L_{q\phi}L_{\phi q}/L_{\phi\phi})/T$ is the (Fourier) thermal conductivity in W/mK, $l_{qw} = l_{wq} = L_{qw} - L_{q\phi}L_{\phi w}/L_{\phi\phi}$, $\pi = L_{q\phi}/L_{\phi\phi}$ is the Peltier coefficient in J/C, $l_{ww} = L_{ww} - L_{w\phi}L_{\phi w}/L_{\phi\phi}$, $t_w = L_{wq}/L_{\phi\phi}$ is the transference coefficient introduced earlier, and $r = 1/L_{\phi\phi}$ is the electrical resistivity in ohm m. We have chosen a definition of the transference coefficient such that its dimension is mol/C. This coefficient will then be given by the more usual transport number (which is dimensionless) multiplied by Faraday's constant (96500 C/ mol). The last equation gives the electric potential gradient in the bulk phases (in the unit V/m). The expression can be integrated to obtain the potential differences across these parts. The current density is given in A/m^2. It is common to model the potential drop across the membrane by the last term only, the resistance drop [Springer et al., 1991]. This means that the cell is normally taken to be isothermal and isobaric.

For the different bulk phases we have:

$$\begin{aligned} \pi^a &= T[(S_e^* + \frac{1}{2}S_{H_2})/F + t_w^a S_w^a] && (5.21) \\ \pi^m &= T[S_{H^+}^*/F - t_w^m S_w^m] && (5.22) \\ \pi^c &= T[(S_e^* - \frac{1}{4}S_{O_2})/F + t_w^c S_w^c] && (5.23) \end{aligned}$$

Here S_i is the entropy and S_i^* is the transported entropy of i . The first equation says that heat (entropy) is transported with electrons, hydrogen and water across the carbon backing on the anode side [Ratkje et al., 1995]. The second says that heat is transported reversibly with protons and water across the membrane. The third expresses that electrons, oxygen and water carry heat through the carbon backing on the cathode side.

The transference coefficients satisfy

$$t_w^a = t_w^m = t_w^c - \frac{1}{2F} \tag{5.24}$$

The first identity says that the need for water transport in the membrane determines the water transport to the anode interface. After the reaction at the cathode interface, half an additional molecule of water is carried along per charge carrier. We shall find the variation in ϕ , μ_w and T across the cell, for given different current densities j, and given boundary conditions. The membrane-electrode interfaces play an important role in the energy conversion and dissipation. They give the boundary conditions for integrations across the three bulk phases as will be explained below.

5.4.2 The anode interface

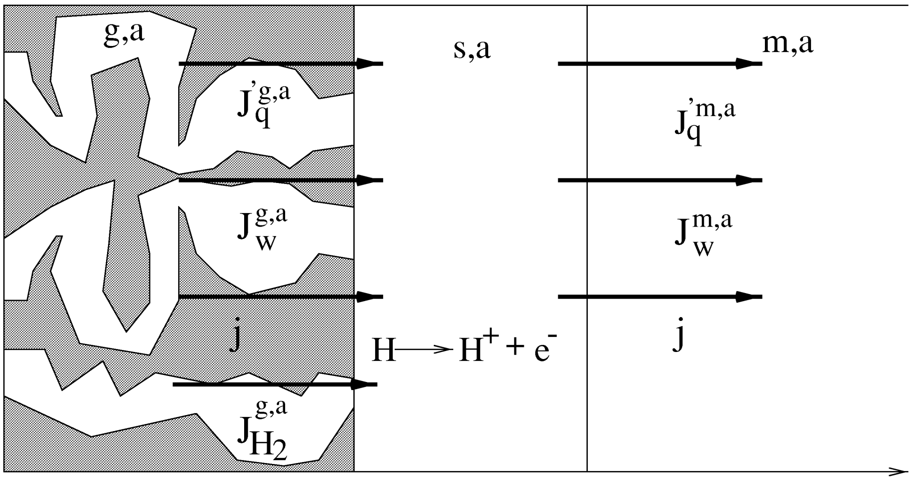

Figure 5.2: Fluxes of heat (J_q'), water (J_w), current (j) and hydrogen (J_{H_2}) into and out of the anode interface. The carbon backing close to the interface is denoted (g,a), the anode interface (s,a) and the membrane close to the interface (m,a).

A schematic illustration of the fluxes into and out of the anode interface is given in Fig. 5.2. The entropy production rate is [Bedeaux et al., 1976; Albano and Bedeaux, 1987; Bedeaux, 1992]:

$$\begin{aligned}\sigma^{s,a} &= -J_q^{\prime g,a}\frac{T^{s,a}-T^{g,a}}{T^{s,a}T^{g,a}} - J_q^{\prime m,a}\frac{T^{m,a}-T^{s,a}}{T^{s,a}T^{m,a}} - J_w^{g,a}\frac{1}{T^{s,a}}(\mu_{w,T}^{s,a}-\mu_{w,T}^{g,a}) \\ &\quad -J_w^{m,a}\frac{1}{T^{s,a}}(\mu_{w,T}^{m,a}-\mu_{w,T}^{s,a}) - j\frac{1}{T^{s,a}}\Delta\phi^{s,a} - v^{s,a}\frac{A^{s,a}}{T^{s,a}} \qquad (5.25)\end{aligned}$$

The thermodynamic variables for the interface were defined in Section 5.2. There are two heat fluxes connected with an interface. One heat flux into (or out if the sign is negative) the interface from the carbon backing, $J_q^{\prime g,a}$, has the conjugate force $-(T^{s,a}-T^{g,a})/T^{s,a}T^{g,a}$. The other heat flux out of (or into, if the sign is negative) the interface into the membrane, $J_q^{\prime m,a}$, has the conjugate force $-(T^{m,a}-T^{s,a})T^{m,a}T^{s,a}$. Similarly, there are two water fluxes, $J_w^{g,a}$ and $J_w^{m,a}$, with conjugate forces $-(\mu_{w,T}^{s,a}-\mu_{w,T}^{g,a})/T^{s,a}$ and $-(\mu_{w,T}^{m,a}-\mu_{w,T}^{s,a})/T^{s,a}$, respectively. The electric current density, j, through the interface, has the conjugate force $-\Delta\phi^{s,a}/T^{s,a} = -(\phi^{m,a}-\phi^{g,a})/T^{s,a}$. We have assumed that the interface has a constant polarization for a given constant j. Thus, there is no contribution to σ^s from the displacement current.

According to Eqs. (5.1) and (5.2), the reaction $\frac{1}{2}H_2(g) \rightarrow H^+ + e^-$ goes in two steps via atomic hydrogen. The total reaction is also illustrated in Fig. 5.1. The contribution to the entropy production rate from the flux of $\mathrm{H}_2(g)$ into the interface is contained in the last term. This term is the product of the electrode reaction rate, $v^{s,a}$, and the affinity, $A^{s,a}$, of the total reaction at the anode. The affinity is equivalent to Gibbs energy change for the anode reaction. The reaction rate is given in terms of the current density by:

$$v^{s,a} = j/F \qquad (5.26)$$

This reaction rate refers to one mole electrons produced. The overall affinity is:

$$A^{s,a} = \mu_{H^+}^{s,a} + \mu_{e^-}^{s,a} - \frac{1}{2}\mu_{H_2}^{g,a} \qquad (5.27)$$

Experimental data [Jerkiewicz and Zolfaghari, 1996; Zolfaghari et al., 1997; Vermeijlen et al., 1997] support the view that hydrogen is adsorbed in atomic form at Pt, and that the chemical potential of the adsorbed atom is the same, whether it is chemisorbed or electrochemically adsorbed.

$$\mu_H^{s,a} = \mu_{H^+}^{s,a} + \mu_{e^-}^{s,a} \qquad (5.28)$$

With Eq. (5.28), the rate limiting step is the first one, with the affinity:

$$A^{s,a} = \mu_H^{s,a} - \frac{1}{2}\mu_{H_2}^{g,a} \tag{5.29}$$

We estimate the affinity in Section 5.5.

By introducing the assumptions and the flux dependencies of Eq. (5.26) into Eq. (5.25), we find:

$$\begin{aligned}\sigma^{s,a} \quad = \quad & -J_q'^{g,a}\frac{\Delta T^{g,a}}{T^{s,a}T^{g,a}} - J_q'^{m,a}\frac{\Delta T^{m,a}}{T^{s,a}T^{m,a}} - J_w^{g,a}\frac{1}{T^{s,a}}\Delta\mu_{w,T}^{g,a} \\ & -J_w^{m,a}\frac{1}{T^{s,a}}\Delta\mu_{w,T}^{m,a} - j\frac{1}{T^{s,a}}\left[\Delta\phi^{s,a} + \frac{A^{s,a}}{F}\right]\end{aligned} \tag{5.30}$$

with $\Delta T^{g,a} = T^{s,a} - T^{g,a}$ and $\Delta T^{m,a} = T^{m,a} - T^{s,a}$ .There are similar definitions for the chemical potential differences. The flux equations follow from the entropy production:

$$J_q'^{g,a} = -l_{qq}^{a,g}\frac{\Delta T^{g,a}}{T^{g,a}} - l_{qq}^{a,gm}\frac{\Delta T^{m,a}}{T^{m,a}} - l_{qw}^{a,g}\Delta\mu_{w,T}^{g,a} - l_{qw}^{a,gm}\Delta\mu_{w,T}^{m,a} + \pi^a j \tag{5.31}$$

$$J_q'^{m,a} = -l_{qq}^{a,mg}\frac{\Delta T^{g,a}}{T^{g,a}} - l_{qq}^{a,m}\frac{\Delta T^{m,a}}{T^{m,a}} - l_{qw}^{a,mg}\Delta\mu_{w,T}^{g,a} - l_{qw}^{a,m}\Delta\mu_{w,T}^{m,a} + \pi^m j \tag{5.32}$$

$$J_w^{g,a} = -l_{wq}^{a,g}\frac{\Delta T^{g,a}}{T^{g,a}} - l_{wq}^{a,gm}\frac{\Delta T^{m,a}}{T^{m,a}} - l_{ww}^{a,g}\Delta\mu_{w,T}^{g,a} - l_{ww}^{a,gm}\Delta\mu_{w,T}^{m,a} + t_w^a j \tag{5.33}$$

$$J_w^{m,a} = -l_{wq}^{a,mg}\frac{\Delta T^{g,a}}{T^{g,a}} - l_{wq}^{a,m}\frac{\Delta T^{m,a}}{T^{m,a}} - l_{ww}^{a,mg}\Delta\mu_{w,T}^{g,a} - l_{ww}^{a,m}\Delta\mu_{w,T}^{m,a} + t_w^m j \tag{5.34}$$

$$\Delta\phi^A = -\pi^a\frac{\Delta T^{g,a}}{T^{g,a}} - \pi^m\frac{\Delta T^{m,a}}{T^{m,a}} - t_w^a\Delta\mu_{w,T}^{g,a} - t_w^m\Delta\mu_{w,T}^{m,a} - r^{s,a}j \tag{5.35}$$

The coefficients include the common factor $1/T^{s,a}$. Their subscript indicate first the flux and then force that is relevant. Their superscripts indicate first the region (here the anode), then the side(s) of the interface that are involved (g, m or both; gm). We calculate the electric potential jump across the anode in terms of the effective electric potential $\Delta\phi^A$ from:

$$\Delta\phi^{s,a} = \Delta\phi^A - \frac{1}{F}A^{s,a} = \Delta\phi^A - \frac{1}{F}(\mu_H^{s,a} - \frac{1}{2}\mu_{H_2}^{g,a}) \tag{5.36}$$

The Peltier heats and the transference coefficients for the anode interface are identical to the bulk values in the adjacent bulk phase. The interface has an excess electric resistance, $r^{s,a}$. Due to Onsager symmetry the l -matrix is symmetric.

Mass and heat fluxes into the anode interface from the carbon backing have cross coefficients similar to the same fluxes in the carbon backing. This is also true for fluxes from the interface into the membrane. The coupling coefficients across the interface are probably less important. We shall therefore neglect the coupling coefficients across the interface, i.e. we take $l_{qq}^{a,mg} = l_{qq}^{a,mg} = l_{qw}^{a,gm} = l_{wq}^{a,gm} = l_{qw}^{a,mg} = l_{wq}^{a,mg} = l_{ww}^{a,gm} = l_{ww}^{a,mg} = 0$. The constitutive relations then reduce to

$$J_q'^{g,a} = -l_{qq}^{a,g}\frac{\Delta T^{g,a}}{T^{g,a}} - l_{qw}^{ag}\Delta\mu_{w,T}^{g,a} + \pi^a j \tag{5.37}$$

$$J_w^{g,a} = -l_{wq}^{a,g}\frac{\Delta T^{g,a}}{T^{g,a}} - l_{ww}^{a,g}\Delta\mu_{w,T}^{g,a} + t_w^a j \tag{5.38}$$

for the heat and water fluxes in terms of the temperature jump, the chemical potential jump and the electric current into the anode interface from the carbon backing. On the membrane side of the interface one similarly obtains

$$J_q'^{m,a} = -l_{qq}^{a,m}\frac{\Delta T^{m,a}}{T^{m,a}} - l_{qw}^{a,m}\Delta\mu_{w,T}^{m,a} + \pi^m j \tag{5.39}$$

$$J_w^{m,a} = -l_{wq}^{a,m}\frac{\Delta T^{m,a}}{T^{m,a}} - l_{ww}^{a,m}\Delta\mu_{w,T}^{m,a} + t_w^m j \tag{5.40}$$

The expression for the electrical potential jump, Eq. (5.35), remains the same.

5.4.3 The cathode interface

The excess entropy production rate of the cathode interface is:

$$\begin{aligned}\sigma^{s,c} \;=\;& -J_q'^{m,c}\frac{T^{s,c}-T^{m,c}}{T^{s,c}T^{m,c}} - J_q'^{g,c}\frac{T^{g,c}-T^{s,c}}{T^{s,c}T^{g,c}} \\ & -J_w^{m,c}\frac{1}{T^{s,c}}(\mu_{w,T}^{s,c}-\mu_{w,T}^{m,c}) - J_w^{g,c}\frac{1}{T^{s,c}}(\mu_{w,T}^{g,c}-\mu_{w,T}^{s,c}) \\ & -\frac{1}{T^{s,c}}j\Delta\phi^{s,c} - \frac{1}{T^{s,c}}v^{s,c}A^{s,a}\end{aligned} \tag{5.41}$$

The symbols have the same meaning as described above for the anode interface, they refer now, however, to the cathode interface. The stationary state reaction rate is again:

$$v^{s,c} = j/F \tag{5.42}$$

and the chemical reaction Eq. (5.6) has affinity:

$$A^{s,c} = \frac{1}{2}\mu_w^{g,c} - \mu_H^{s,c} - \frac{1}{4}\mu_{O_2}^{g,c} \tag{5.43}$$

where we have used again the assumption $\mu_H^{s,c} = \mu_{H^+}^{m,c} + \mu_{e^-}^{g,c}$. The entropy production rate becomes:

$$\sigma^{s,c} = -J_q'^{m,c}\frac{\Delta T^{m,c}}{T^{s,c}T^{m,c}} - J_q'^{g,c}\frac{\Delta T^{g,c}}{T^{s,c}T^{g,c}} - J_w^{m,c}\frac{1}{T^{s,c}}\Delta\mu_{w,T}^{m,c} \tag{5.44}$$

$$-J_w^{m,c}\frac{1}{T^{s,c}}\Delta\mu_{w,T}^{g,c} - j\frac{\Delta\phi^C}{T^{s,c}} \tag{5.45}$$

with the effective electric force, $\Delta\phi^C$. The effective electrical potential, in terms of the electric potential jump across the cathode interface, is:

$$\Delta\phi^{s,c} = \Delta\phi^C - \frac{1}{F}A^{s,c} = \Delta\phi^C - \frac{1}{F}(\frac{1}{2}\mu_w^{g,c} - \mu_H^{s,c} - \frac{1}{4}\mu_{O_2}^{g,c}) \tag{5.46}$$

Neglecting again the coupling coefficients *across* the interface for heat and water flow the constitutive relations become

$$J_q'^{m,c} = -l_{qq}^{c,m}\frac{\Delta T^{m,c}}{T^{m,c}} - l_{qw}^{c,m}\Delta\mu_{w,T}^{m,c} + \pi^m j \tag{5.47}$$

$$J_w^m = -l_{wq}^{c,m}\frac{\Delta T^{m,c}}{T^{m,c}} - l_{ww}^{c,m}\Delta\mu_{w,T}^{m,c} + t_w^m j \tag{5.48}$$

for the membrane side of the interface, and

$$J_q'^{g,c} = -l_{qq}^{c,g}\frac{\Delta T^{g,c}}{T^{g,c}} - l_{qw}^{c,g}\Delta\mu_{w,T}^{g,c} + \pi^c j \tag{5.49}$$

$$J_w^c = -l_{wq}^{c,g}\frac{\Delta T^{g,c}}{T^{g,c}} - l_{ww}^{c,g}\Delta\mu_{w,T}^{g,c} + t_w^c j \tag{5.50}$$

for the cathode side of the interface. The effective electrical potential is given by

$$\Delta\phi^C = -\pi^m\frac{\Delta T^{m,c}}{T^{m,c}} - \pi^c\frac{\Delta T^{g,c}}{T^{g,c}} - t_w^m\Delta\mu_{w,T}^{m,c} - t_w^c\Delta\mu_{w,T}^{g,c} - r^{s,c}j \tag{5.51}$$

This expression can be used with Eq. (5.46) to find the electric potential jump across the cathode interface.

5.5 The cell potential and the electrode overpotentials

5.5.1 The cell potential

The local cell potential variation, $\phi(x)$, can be calculated for each part of the cell. The integration of the electric potential is carried out over the carbon backing on the anode side, Eq. (5.20), the anode interface, Eqs. (5.35) and (5.36), the membrane electrolyte, Eq. (5.20), the cathode interface, Eqs. (5.51) and (5.46), and the carbon backing on the cathode side, Eq.((5.20)). The integration starts in the carbon backing at a point with a distance d^a from the anode interface. The temperature and the chemical potential of water at this point are T_o^a and $\mu_{w,o}^a$, respectively. The integration ends at a point in the carbon backing on the cathode side with a distance d^c from the cathode interface. The temperature and the chemical potential of the water at this point are T_o^c and $\mu_{w,o}^c$. We calculate the complete electric potential profile across the cell, using these equations and conditions in Section 5.7. We investigate the interface potential jumps in the next subsection, and the variations in the same in subsection 5.5.3.

The total cell potential is the sum of all contributions:

$$\Delta\phi = \int_a^{g,a} d\phi + \Delta\phi^{s,a} + \int_{e,a}^{e,c} d\phi + \Delta\phi^{s,c} + \int_{g,c}^{c} d\phi \tag{5.52}$$

By introducing all appropriate expressions, using constant entropies in the Peltier coefficients, and constant transference coefficients and electrical resistances, we obtain:

$$\begin{aligned}
\Delta\phi \;=\; & \Bigg[-\left[\frac{1}{2F}\mu_w^{g,c} - \frac{1}{4F}\mu_{O_2}^{g,c} - \frac{1}{2F}\mu_{H_2}^{g,a}\right] + \frac{1}{F}\left[\mu_H^{s,c} - \mu_H^{s,a}\right] \\
& - \left[\frac{1}{F}\left(S_{e^-}^* + \frac{1}{2}S_{H_2}\right) + \frac{t_w^a}{2}S_w^a\right](T^{s,a} - T_o^a) \\
& - \left[\frac{1}{F}S_{H^+}^* - t_w^m S_w^m\right](T^{s,c} - T^{s,a}) \\
& - \left[\frac{1}{F}(S_{e^-}^* - \frac{1}{4}S_{O_2}) + \frac{t_w^c}{2}S_w^c\right](T_o^c - T^{s,c})\Bigg] \\
& -t_w^a(\mu_{w,T}^{s,a} - \mu_{w,o}^a) - t_w^e(\mu_{w,T}^{s,c} - \mu_{w,T}^{s,a}) - t_w^c(\mu_{w,o}^c - \mu_{w,T}^{s,a}) \\
& -j(r^a d^a + r^{s,a} + r^e d^e + r^{s,c} + r^c d^c)
\end{aligned} \tag{5.53}$$

The cell *emf* is defined by $E = \lim_{j\to 0}(\Delta\phi)$. The classical cell *emf* is $E = -\Delta_r G/F$, with $\Delta_r G$ from Eq. (5.9). For a zero electric current, constant temperature and constant chemical potential of water, we find an additional contribution to E, $(\mu_H^{s,c} - \mu_H^{s,a})/F$, compared with the classical result. The classical result is recovered for $dT = 0$, $d\mu_{w,T} = 0$, $j \to 0$ and

$$\mu_H^{s,a} = \mu_H^{s,c} \tag{5.54}$$

Experimental values for E are about 0.2 V less than the *emf* (1.18 V for $70^o C$ and 1 bar) calculated from Eq. (5.9) [Møller-Holst, 1996b]. The discrepancy has been explained by mixed cathode potentials, or Pt-corrosion potentials, or low exchange current densities [Bockris and Srinivasan, 1969]. We see below that it can be explained, in terms of a difference between the chemical potentials of hydrogen at the anode and cathode surface. This would also explain the reproducible nature of the effect. We estimate the size of the term below, on the basis of known values for the chemical potential of H at the surface of Pt.

5.5.2 Maximum interface potential jumps (Constant $\mu_{w,T}$ and T)

The maximum potential jumps across the electrode interfaces for constant temperature and chemical potential of water, are according to Eqs. (5.36) or (5.46), $\Delta\phi^s = -\frac{1}{F}A^s(j=0)$. This is the potential jump in the *emf*-measurement. For the anode interface we have:

$$(\Delta\phi^s)_{j=0} = -\frac{1}{F}\left(\mu_H^{s,a} - \frac{1}{2}\mu_{H_2}^{g,a}\right) \tag{5.55}$$

The difference in chemical potentials is the Gibbs energy change for adsorption of hydrogen gas on Pt. The chemical potential of H in the μm thick layer that we define as the interface, $\mu_H^{s,a}$, is equal to the chemical potential of H at the Pt-surface, since H occurs only adsorbed at Pt in the interface region.

We can estimate the potential jumps at the anode and cathode from the standard Gibbs energy change for adsorption of H from an acid solution, reported for different surface coverages of hydrogen on Pt and Rh by Jerkiewicz and Zolfaghari [1996]; Zolfaghari et al. [1997]. One of their major findings was that the state of H for electrochemical adsorption from the solution was identical to state of chemisorbed gas. The membrane side of our interface is also acid; we have a membrane polymer with a high proton concentration. In lack of other data, we shall use their value for $\mu_H^{s,a}$ for high surface coverage on Pt, for T =343 K (-11 kJ mol^{-1}), with Eq.(5.55). This gives $(\Delta\phi^{s,a})_{j=0} = 0.11$ V for $p_{H_2(g)} = 1$ bar. This is illustrated in Fig. 5.4. The data [Jerkiewicz and Zolfaghari, 1996; Zolfaghari et al., 1997] indicate that $\mu_H^{s,a}$ will be more negative when the acidity increases. This means that our estimate of $(\Delta\phi^{s,a})_{j=0}$ may be too high.

The affinity for the reaction at the cathode surface is:

$$\begin{aligned} A^{s,c} &= \frac{1}{2}\mu_w^{g,c} - \mu_H^{s,c} - \frac{1}{4}\mu_{O_2}^{g,c} = \frac{1}{2}h_w^{g,c} - h_H^{s,c} - \frac{1}{4}h_{O_2}^{g,c} \\ &\quad -T\left(\frac{1}{2}s_w^{g,c} - s_H^{s,c} - \frac{1}{4}s_{O_2}^{g,c}\right) \end{aligned} \tag{5.56}$$

At the cathode, the excess surface density of polarized hydrogen atoms (the surface coverage of H) must be much smaller than at the anode. We expect that it is virtually zero at low current densities. The data cited above [Jerkiewicz and Zolfaghari, 1996; Zolfaghari et al., 1997] were extrapolated to zero surface coverage to give $\mu_H^{s,c} = -20$ kJ mol^{-1}. The other thermodynamic data were taken from standard tables, see Section 6.2. The results were $A^{s,c} = -94.6$ kJ mol^{-1}, giving $(\Delta\phi^{s,c})_{j=0} = 0.98$ V. In other words, the electrochemical reaction at the cathode is responsible for a major part of the cell's *emf*, see Fig. 5.4.

The sum of the anode and cathode potential jumps is the total *emf*, 1.09 V from these estimates. This is 0.11 V less the classical value. The origin of the reduction is the difference $\mu_H^{s,a} - \mu_H^{s,c} = -10$ kJ mol^{-1}.

The jumps in the electric potential for *emf*- conditions, reflects a *reversible* energy change in the interface during the electrochemical reaction. In the anode, the positive jump is due to the spontaneous adsorption of gas. When there is local equilibrium between the bulk gas and the surface, the term is of course zero. A higher acidity in the membrane than in the solution we have taken data from, will also make the anode potential jump smaller. At the cathode, however, the term is never zero. Here the jump reflects that the chemical reaction is not in equilibrium. This is not in conflict with the interface being in local *thermodynamic* equilibrium. The potential jumps across the interfaces do *not* represent a loss of energy, for a kinetically hindered discharge reaction (with a high activation energy). In the limit of zero current density, the chemical reaction is reversible, and the energy change is likewise.

5.5.3 Electrode overpotentials (Constant $\mu_{w,T}$ and T)

The overpotential of an electrode surface is the potential between a current carrying electrode (working electrode) and a reference electrode of the same kind, which carries negligible current. We distinguish between the concentration overpotential, and the surface overpotential (see e.g. Newman [1991]). The concentration overpotential is due to gradient(s) in chemical potential(s) of component(s) accumulating in front of the working electrode. According to Newman, the concentration overpotential contains also a term due to excess electric resistance. The concentration overpotential derived from irreversible thermodynamics gives the same result. The surface overpotential is due to the *rate limiting* electrochemical reaction [Newman, 1991]. The Butler-Volmer equation is normally used to describe the surface overpotential, but Newman states that the Gibbs energy change of the electrochemical reaction is equivalent to the Butler-Volmer equation [Newman, 1991, p. 187]. In irreversible thermodynamics, differential change in Gibbs energy of the electrode reaction plus a resistance drop, gives the electrode surface overpotential at constant temperature. We shall see below how this can be derived for our interfaces.

Consider again the overpotential experiment. We examine such an experiment for both fuel cell electrodes. The chemical potential of water and the temperatures are constant across the interfaces. We assume that we are able to neglect (or correct for) contributions to the measurement from the membrane, so that we deal only with the contribution from the membrane-electrode interface. The working electrode in the experiment, has its interface potential drop from Eqs.(5.36) or (5.46):

$$\Delta\phi^s = -\frac{1}{F}A^s(j) - r^s j$$

The reference electrode has the opposite interface potential drop, taken for $j = 0$. The overpotential is the sum of these potential drops:

$$\eta^s = \Delta\phi^s(j) - \Delta\phi^s(j=0) = -[A^s(j) - A^s(j=0)]/F - r^s j \qquad (5.57)$$

The expression gives $\eta^s = 0$ when $j = 0$, as it should. The affinity is equal to the Gibbs energy change of the reaction at constant temperature. When the reaction for $j = 0$ is fast, there is local chemical equilibrium in the interface and $A^s(j = 0) = 0$. The expression (5.57) contains a reversible contribution (from the affinities) and a dissipative contribution (from the resistance term).

Equation (5.57) will describe *the change* in the interface potential drop at the working electrode, (here change in the Gibbs energy), from its value in the *emf*-experiment.

For our anode reaction, Eq.(5.57) gives:

$$\eta^{s,a} = [\mu_H^{s,a}(j=0) - \mu_H^{s,a}(j)]/F - r^{s,a}j \tag{5.58}$$

Experiments on fuel cells give the anode overpotential as a linear function of current density [Møller-Holst, 1996b]. This must then mean that $\eta^{s,a} = -r^{s,a}j$, with constant $r^{s,a}$ and that $\mu_H^{s,a}(j=0) = \mu_H^{s,a}(j)$ (the surface coverage of H varies little with j). The resistance, $r^{s,a}$, is the resistance of the electrochemical reaction (5.2).

The similar expression for the cathode gives:

$$\begin{aligned}\eta^{s,c} &= \frac{1}{F}\left(\frac{1}{2}\mu_w^{g,c} - \mu_H^{s,c} - \frac{1}{4}\mu_{O_2}^{g,c}\right)_{j=0} \\ &\quad -\frac{1}{F}\left(\frac{1}{2}\mu_w^{g,c} - \mu_H^{s,c} - \frac{1}{4}\mu_{O_2}^{g,c}\right)_{j} - r^{s,c}j\end{aligned} \tag{5.59}$$

where $r^{s,c}$ is the resistance of reaction (5.6). The chemical potential of bulk water and oxygen gas disappear from the expression, giving the same final form as Eq.(5.58):

$$\eta^{s,c} = \frac{RT}{F}\ln\frac{a_H^{s,c}(j)}{(a_H^{s,c})_{j=o}} - r^{s,c}j \tag{5.60}$$

It is likely that the chemical potential of H in the polarized interface depends on j.

Measurements indicate, however, that $\eta^{s,c}$ depends on the oxygen pressure in the bulk phase [Vermeijlen et al., 1997]. This means that the assumptions we have used to derive Eq. (5.59) are not valid. When the assumption $\mu_{O_2}^{s,c} = \mu_{O_2}^{g,c}$ is removed, we obtain

$$\eta^{s,c} = \frac{RT}{F}\ln\frac{a_H^{s,c}(j)[p_{O_2}^{s,c}(j)]^{\frac{1}{4}}}{[a_H^{s,c}(p_{O_2}^{s,c})^{\frac{1}{4}}]} - r^{s,c}j \tag{5.61}$$

It is interesting to compare the expressions above to experimental results. Such results are often summarized by the empirical Tafel equation [Springer et al., 1991; Bockris and Srinivasan, 1969; Newman, 1991]:

$$\eta^{s,c} = \frac{2RT}{F}\ln\frac{j}{j_o} \tag{5.62}$$

with the exchange current density, j_o, directly proportional to the oxygen pressure, p_{O_2}, $j_o = j'_o p_{O_2}$. The exchange current density and the factor 2 depend on the electrode activity [Vermeijlen et al., 1997]. A direct comparison of the two equations (5.60) and (5.62) says that the two expressions lead to the same behavior if the chemical activity of H is given by $a_H^{s,c}(j) = a_H^{s,c}(0)[1 + (j/j_o)^2]$, and $r^{s,c}j$ can be neglected. The polarized nature of the atom and Eq. (5.43) is relevant in this context. By putting the two equations equal to one another, we can determine $a_H^{s,c}(j)$ (or $a_{H^+e^-}^{s,c}(j)$) for the cathode from Tafel plots. The overpotential for hydrogen evolution has also been related to the hydrogen pressure [Jerkiewicz and Zolfaghari, 1996; Zolfaghari et al., 1997]. With the terminology used in this work, we have from [Jerkiewicz and Zolfaghari, 1996; Zolfaghari et al., 1997]

$$\eta^{s,a} = -\frac{RT}{2F} \ln \frac{p_{H_2}^{g,a}(j)}{(p_{H_2}^{g,a})_{j=o}}$$

This equation is obtained by neglecting $r^s j$, and by assuming that there are (different) equilibria across the interface, depending on the current density, $\mu_H^s(j) = \frac{1}{2}\mu_{H_2}^g(j)$.

5.6 Cell dimensions and properties

5.6.1 Cell geometry and operation

The single fuel cell used in our model study was constructed by Møller-Holst [1996b]. The carbon backing (part 3 of Fig. 5.1) has a thickness of 180 μm, and a porosity of 0.4. The tortuosity is taken to be 7 [Springer et al., 1996]. The carbon backing is made from a porous carbon cloth, impregnated with carbon and Teflon. The interface is made by mixing 65 wt% of 20 wt% Pt on C with 15 wt% Nafion 117 and 20 wt% carbon [Møller-Holst, 1996b]. The result is the 10 μm catalyst layer, shown in detail on the insert in Fig.5.1. The final layer has 13 wt% or 0.1 mg Pt cm^{-2} membrane surface. The carbon backing of the two sides are made the same way, and have the same properties. The membrane is standard for the purpose, Nafion 117 from DuPont, 175 μm thick (part 1 of Fig.5.1). The membrane has molecular weight of M_m =1.1 kg/mol, dry density of $\rho_{dry} = 1.64 \cdot 10^{\,3}$ kg m^{-3}, and swelling factor $s = 0.0126$ [Springer et al., 1991].

The outer parts of the carbon backing are thermostatted at 70 °C and the cell is operated at 1 bar. The hydrogen and oxygen gases are saturated with water at a slightly higher temperature, to maintain the saturation pressure p_w in the cell. Gases are supplied by flows perpendicular to the transport direction with flow rates $F_{H_2} = F_{O_2} = 3.406 \cdot 10^{-5}$mol s^{-1}, and $F_w^a = F_w^c = 2.984 \cdot 10^{-6}$ mol s^{-1}.

5.6.2 Transport properties and thermodynamic data

We have taken a constant water transference number through the membrane, $t_w = 1.2$. Ottøy [1996] found this result for a membrane in contact with water vapor, and with a water contents, λ, between 2 and 14 molecules of water per ionic site. Likewise, the diffusion constant of water, scaled to dry membrane, was taken as the constant self diffusion constant, in the absence of pressure gradients, $D_w = 1.2 \cdot 10^{-10}$ m^{2}s^{-1} [Springer et al., 1991]. In the presence of pressure gradients, we used $l_{ww} = 1.2 \cdot 10^{-6}$ s mol^2(m^{3}kg)$^{-1}$ [Ratkje et al., 1995].

The thermal conductivity of the membrane was estimated to λ^e =0.2 W/mK as the harmonic mean of the conductivity of rubber (60 vol%) and water (40 vol%) [Nummedal, 1996]. The thermal conductivity of the electrodes were taken to be that of carbon, $\lambda^a = \lambda^c = 10$ W/mK [Delhaès and Carmona, 1981]. The excess interface resistance to heat transfer was taken to be 100 times larger than that of the membrane, so that it scales similar to the electric resistance [Kjelstrup and Bedeaux, 1997].

The electric resistance of the membrane varies largely with the membrane water content and will therefore give a varying electric potential gradient through the membrane. According to Springer et al. [1991] we have

$$r^e(30^oC) = \frac{1}{0.005139\lambda - 0.00326} \tag{5.64}$$

$$r^e(T) = \exp\left[-1268\left(\frac{1}{303} - \frac{1}{T}\right)\right] \tag{5.65}$$

The excess resistance of the two interfaces was found by subtracting the membrane resistance and the resistance of the carbon backing from the total cell resistance [Møller-Holst, 1996b]. The excess interface resistance of one electrode was then found as half this value, giving $r^{s,a} = r^{s,c} = 7.15 \cdot 10^{-6}$ ohm m^2 for the 10 μm layer. The resistance of the carbon backing was $2 \cdot 10^{-4}$ ohm m.

Thermodynamic data were taken from ref. [Aylward and Findlay, 1971]. The standard Gibbs energies of formation for liquid and vapor water at this temperature and pressure are g_w^o = -237 and -229 kJ/mol, respectively. Standard entropies are $s_{H_2}^o = 131$, $s_{O_2}^o = 205$,, $s_w^o = 189$ J/molK for the gas and $s_w^o = 70$ J mol^{-1}K^{-1} for the liquid. The standard Gibbs free energies of formation for the pure gases are zero. The transported entropy of electrons was neglected, giving $S_{H+}^* - t_w S_w = 13.4$ J/Kmol. [Ratkje et al., 1995].

5.7 Further results

5.7.1 The water concentration profile

The concentration profile of water in the membrane as a function of current density, was determined from Eq. (5.16) rewritten as

$$J_w = -D_w \frac{dc_w}{dx} + t_w j \tag{5.66}$$

Here D_w is the diffusion constant of water and c_w is the water concentration in the membrane. The current density varied between 10^{-3} and 0.7 A/cm^2. The equation was solved for constant J_w, j,T, and p. The iteration procedure of Springer et al. [1991] was applied, to adjust the water activity at the boundaries to the water activity in the gas phase, and to the gas flow rates. We thus assumed equilibrium for water across the membrane surface, $\Delta\mu_w^{s,a} = \Delta\mu_w^{g,a} = 0$ and $\Delta\mu_w^{s,c} = \Delta\mu_w^{g,c} = 0$. The resulting concentration profiles for $dP = 0$ and $dT = 0$ are shown in Fig.5.3. The water flux consistent with this calculation was constant within a few percent for current densities chosen.

The figure shows that the concentration profiles for water are linear across the membrane for all current densities. This is due to the constant D_w and t_w. The value of D_w is so small, that we only have a significant contribution to J_w from diffusion when j is very large. As a consequence, the membrane resistance, that is a function of the water content, will vary largely for high current densities. We shall see that this determines the shape of the electric potential profile in the membrane. The results of Fig. 5.3 raise the question of how back diffusion can be increased. This lead us to investigate the effect of a pressure gradient across the membrane, see below.

From the water concentration profiles, the membrane resistance at any position in the membrane was calculated from Eq. (5.64) and (5.65). The electric potential profile across the membrane was then calculated from Eq. (5.20) for varying current densities (see below).

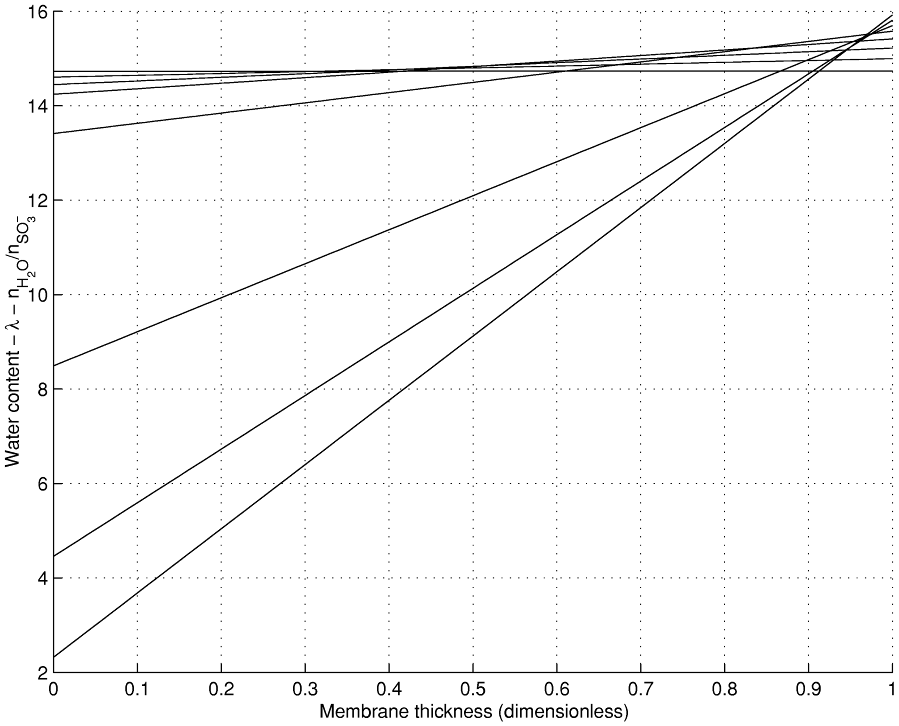

Figure 5.3: The calculated water concentration profile through the membrane under fuel cell operation. The current density varies from 1 mA/cm^2 to 600 mA/cm^2. The anode is to the left.

5.7.2 Electric potential profiles and the polarization curve

The electric potential profile, calculated for $j = 0$, with $dT = 0$ and $dp = 0$, is shown by horizontal lines connected with jumps over the interfaces in Fig.5.4. The electric potential is constant in all bulk phases, since there are no ohmic losses. The importance of the cathode as the place where the potential jump of the cell is generated, is seen. The small, but significant contribution by the anode to the total potential, means that this interface should not be neglected when improvements are discussed. The sum of the electrode potential jumps is the *emf* of the cell, as discussed in Section 5.5.

Electric potential profiles for increasing values of j are compared in the same figure. The electric potential profile is (almost) constant in the carbon backing, due to the high electric conductivity, except at very high current densities. The positive potential gain in the anode, as well as in the cathode, is visibly reduced by the ohmic resistance that we have used for the interfaces, already for the lowest current density. The nonlinear profile in the electrolyte, especially at high current densities, is due to the changing water content of the membrane. The curve has a higher slope close to the anode, in agreement with Fig. 5.3.

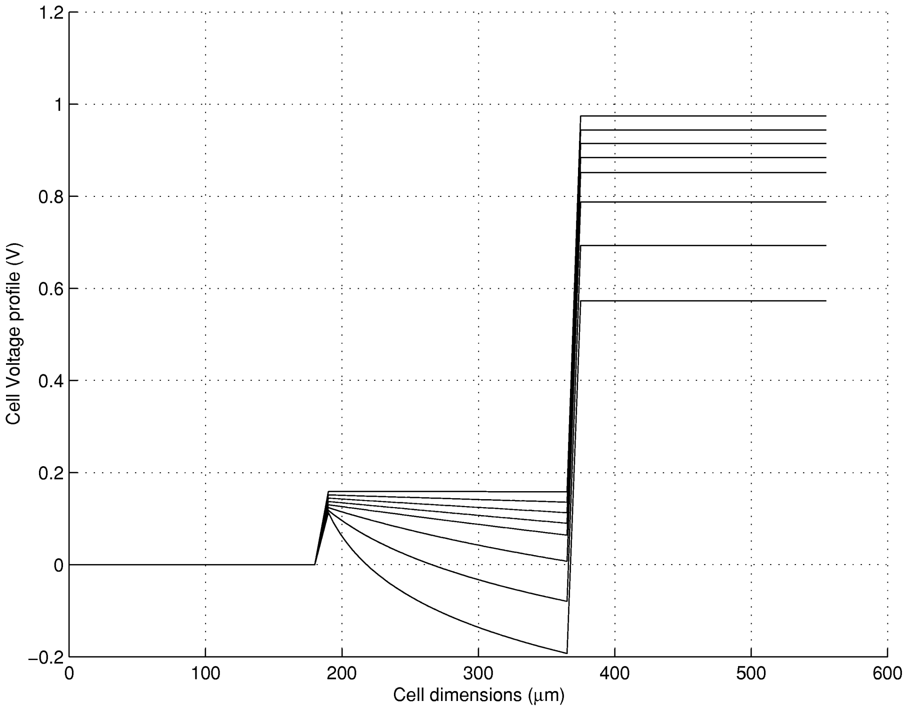

Figure 5.4: The electric potential profile through the fuel cell at different current densities. The anode is to the left.

The relation between the cell potential $\Delta\phi$ and the electric current density j, is the polarization curve (see Fig. 5.5 below). Such curves have been used extensively to evaluate fuel cell performance. In order to establish a basis for our results, we recalculated the results of Springer et al. [1991], using their expressions Eq. (5.64) and Eq. (5.65), with the water concentration profiles from Fig. 5.3. The model has later been extended by Springer et al. [1993], but we have chosen their first work as a principle reference because of its clearness.

The polarization curve, derived from their expressions, is shown with star symbols in Fig. 5.5. The curve has three typical phases. There is a rapid potential drop for small current densities, followed by an approximately linear region up to 0.5 A/cm^2, and an increasing negative slope as the current density increases beyond that value. While the first phase has been explained by the cathode overpotential, the last phase has been explained by the change in the membrane resistance with the water content.

The corresponding polarization curve from our equations is given by the open symbols in Fig.5.5. This curve uses the same $\mu_H^{s,a}$ and $\mu_H^{s,c}$ that we found in the estimates above, a constant temperature and pressure, and the membrane water content profiles of Fig.5.3. We start the curve at 1.09 V. The first phase has a different structure, because we have not used a chemical potential of H that varies with j (i.e. we have not introduced overpotentials). The second phase can be used to determine the constant cell resistance. The third phase of the curve is similar to that of the reference model. The difference between the curves represents the difference of chemical potentials of the polarized H-atom at the membrane-electrode interface. By taking the difference between our curve and an experimental polarization curve, we can obtain an estimate for $\mu_H^{s,c}$, when $\mu_H^{s,a}$ is known.

5.7.3 Pressure difference effects

The fact that diffusion of water in the membrane from the cathode to the anode is low, with the set of data that we have used, leads to a speculation that a positive *pressure difference* across the membrane may be profitable for the membrane resistance: If one can increase the force on water in this direction, one will need a smaller supply of water on the anode side. A calculation using a pressure difference of 1 bar between the electrodes indeed led to a more even distribution of water across the membrane. At very small current densities, there was even a net transport of water from the cathode to the anode. The cell potential was affected by this through $\Delta\mu_w = V_w\Delta p$. The difference in chemical potential of water across the membrane lead to a decrease in the *emf* we calculate of 30 mV. This means that there is a trade-off between reducing the membrane resistance loss, and increasing the chemical potential difference

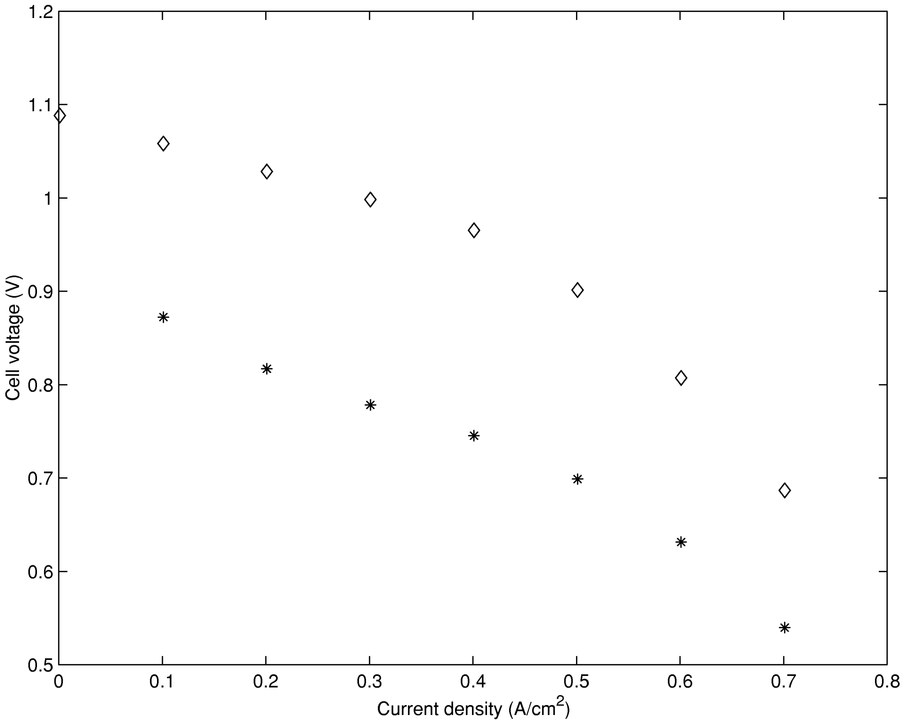

Figure 5.5: Polarization curves calculated for different mathematical models of the solid polymer fuel cells. $*$: The model based on Springer et al. [1991]. $\diamond$: Model based on equations given here, without overpotentials.

of water across the membrane.

5.7.4 Thermal gradient effects

In the laboratory, the outer parts of the cell are normally kept at constant temperature. One may ask whether it is profitable to maintain a difference in temperature between the two sides. The electric potential profile through the cell is affected by the temperature according to Eqs. (5.35) and (5.51). This was not taken into account in the calculation of potential profiles described above, where we assumed that the total cell was thermostatted, and that $\Delta P = 0$.

In order to find the impact of the local temperature on the cell behaviour, we calculated the temperature profile through the cell setting the same terminal temperature of the carbon backing on the two sides. We did not include the overpotentials at the electrodes. The results are presented in Fig. 5.6. We see that the temperature of the membrane rises, depending on the current density, to about 4 K above the terminal temperature for the highest current density. The rise in surface temperatures is proportional to the current density, as expected from the Peltier effect, see Eqs.(5.21) and (5.23).

The higher temperature in the membrane is caused by the Joule heat. The estimated thermal conductivity that we have used, is obviously so low that heat can accumulate. Such heat accumulation may have a bearing on the kinetics of the electrode reactions and the overpotential of the cathode. (The effect on the reversible part of the cell potential is small). More should be known about the thermal conductivity of the membrane and the membrane surface, to establish what the correct surface conditions are.

The temperature profiles in the bulk phases are linear, consistent with constant thermal conductivity in these phases, and a negligible local Joule heat. The fuel cell process are maintained by an energy flux from the cathode to the anode. A temperature difference of 5 K in either direction between the electrodes, has a negligible impact on this energy flux. The surface temperature is always higher than the electrode bulk temperature. The next step will be to see how the overpotential affects this situation.

5.8 Discussion and conclusions

Irreversible thermodynamics has been used to analyze major events in the solid polymer fuel cell; that is the membrane-electrode interface reactions, membrane transport, and a few operating conditions. From the chemical potential of hydrogen at the electrode surface, we have estimated the membrane-electrode interface potential jumps, and given the *emf* of the system. We have calculated the electric potential profile through the cell and have shown how it varies with current density and membrane water content for isothermal, isobaric conditions. We have given expressions for the overpotential, and shown how that the drop in electric potential is related to the chemical potential of hydrogen in the interface. Equations that deal with pressure - and temperature gradients and their interaction with other intensive variables, have been presented and discussed, so that a basis for more detailed calculations has been laid.

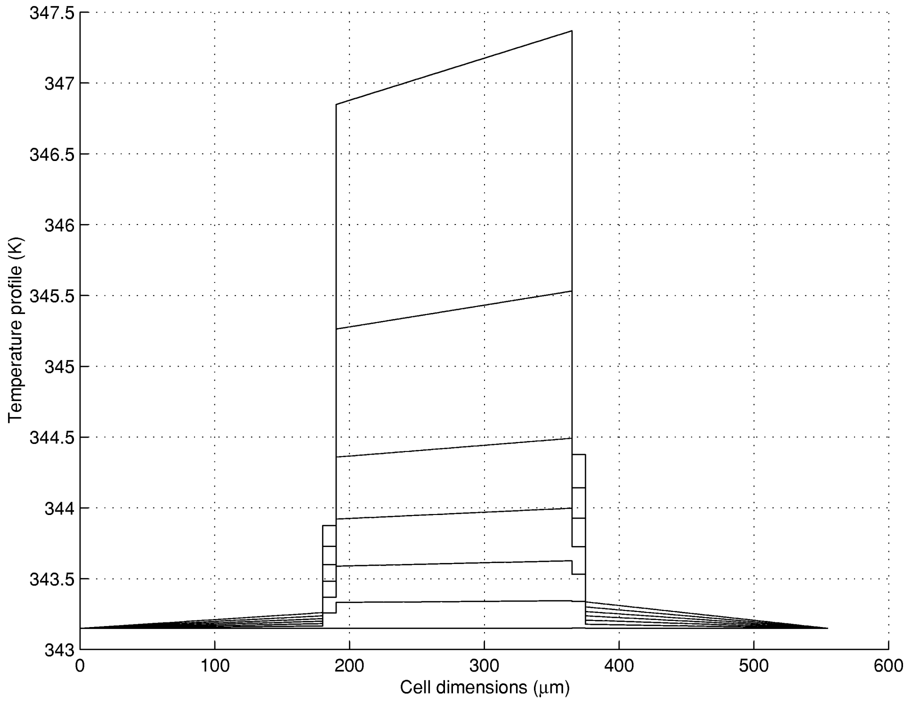

Figure 5.6: Temperature profiles in the fuel cell for different current densities. The anode is to the left.

While the equations that are obtained for the overpotential from irreversible thermodynamics are almost the same as those normally used, the premises that are used in their derivation differ. We assume local equilibrium in the interface (for all current densities) and linear flux-force relationships. The overpotential has a reversible and a dissipative term. The Butler-Volmer equation and the Tafel equation, on the other hand, have a non-linear relation between *one* flux, j, and the overpotential, η^s. The Butler-Volmer model has inherent a dissipative term, as is seen by expansions for small current densities. The model behind the Butler-Volmer equation, the jump of the charged particle across an activation barrier, was however also related to differences in chemical potentials [Newman, 1991].

Our equation for the overpotential can be tested by measuring $\mu^s_H(j)$, independent of the electrochemical reaction. Further progress could be made in this manner. A simultaneous solution of all variables in the heterogeneous system is also lacking. Several aspects remain to be studied; for instance the gas diffusion in the carbon backing. This is, however, outside the scope of a book dealing with membrane surfaces.

Acknowledgements

P.J.S. Vie is grateful for a grant given by the Norwegian Research Council. D. Bedeaux was Onsager professor at NTNU when the work was done. S. Møller-Holst is thanked for critical comments to the manuscript. K. Nisancioglu is thanked for pointing out to us Newman's equivalent forms for the surface overpotential.

List of symbols

a	anode
a_i^y	activity of i in y
$A^{s,y}$	affinity in y surface reaction
c	cathode
d	differential
d	distance
D_i	diffusion constant of i [m^2/s]
e	electron
emf	electromotive force
F	Faraday's constant [96485 C/mol]
F_i	Flow of i
g	gas
g_i^y	Gibbs energy of i in y [J/mol]
G	Gibbs energy [J/mol]
h_i^y	enthalpy of i in y [J/mol]
H	enthalpy [J/mol]
i	component
j	current density [A/m^2]
j_0	exchange current density
J_i^y	flux of i in y [mol/m^2s]
$J_q^{\prime y}$	flux of measurable heat in y
J_e	energy flux [J/m^2s]

l_{ij}	Onsager coefficient for diffusion
L_{ij}	Onsager coefficient (basic)
m	membrane
M_m	molecular weight [kg/mol]
n_i	mass density of i
P_i	pressure of i [Pa]
r^y	electrical resistivity in y [Ωm]
R	universal gas constant [8.3143 J/molK]
s	surface
s	swelling factor
s	entropy density
s_i^y	entropy of i in y [J/molK]
S	entropy [J/K]
S^*	transported entropy [J/molK]
t_w^y	water transference number in y
T^y	temperature in y [K]
u	energy density
$v^{s,y}$	surface reaction rate in y [mol/m^{2}s]
V_i	molar volume of i [m^3/mol]
w	water, H_2O
x	coordinate
y	phase, example: s,a,g, or c
α	$J_w^a/J_{H_2}^a$
Δ	a difference
η^y	overpotential in y
λ^y	Fourier thermal conductivity in y [W/mK]
μ_i^y	chemical potential of i in y
π^y	Peltier coefficient in y
ρ	density [kg/m^3]
σ^y	entropy production in y [J/Km^{3}s]
ϕ	electrical potential [J/mol]

Chapter 6

Local heat production

6.1 Introduction

The understanding of the heat-production and heat-transport in the polymer fuel cell is essential for the commercialisation of the fuel cell system. Irreversible losses occur both locally at the electrode surfaces and in the current conducting media. Depending on the thermal conductivity of the different parts of the fuel cell, increased local temperatures can occur, see chapter 5. Measurements of increased local temperatures along current stream lines have already been demonstrated in other electrochemical systems [Kjelstrup et al., 2000; Millet, 1991].

No research groups have yet, to our knowledge, tried to measure a temperature profile perpendicular to the membrane surface in a fuel cell, measuring the local temperatures close to the electrodes. However, temperature measurements along gas channels in fuel cells have previously been measured and modelled. Kobayashi et al. [1989] measured the temperature distribution over the end plates on the cathode and anode in a molten carbonate fuel cell. They measured the temperatures in the reacting gases in a two dimensional grid along the flow plates. Adžić et al. [1997] performed similar measurements in the solid oxide fuel cell. Both groups of scientists demonstrated temperature gradients along the end-plates. Later Kobayashi's group [Fujimura et al., 1992] used their previous results [Kobayashi et al., 1989] to model the temperature in a three-dimensional grid, introducing the axis perpendicular to the gas flow-plates.

Local temperatures in the polymer fuel cell will be reported in this chapter. Temperatures can be measured in several different layers of the fuel cell. Equations for the heat-transport and heat-production are obtained from irreversible thermodynamics. These equations describe the system and help to understand the measured temperatures. Thermal conductivities in the system are calculated by introducing the measured temperatures into the equations.

Thermal effects due to the electrode overpotentials and the phase transition of water were not included in chapter 5. As will be shown, these are important effects, and will be included here. Peltier heats will however not be included due to the relatively large measurement errors.

6.2 Thermal effects

The heat transfer in the polymer fuel cell was described in chapter 5. In this section the thermal effects will be further elaborated for the five layers in the polymer fuel cell.

6.2.1 The anode backing

The energy balance over the anode gas diffusion backing is presented in equation (6.1). Heat is entering the backing by heat conduction (J'_q) and the transport of hydrogen and water ($J_\mathrm{x} h_\mathrm{x}$). Heat is produced due to an ohmic resistance in the backing.

$$\begin{aligned} & J'^{g,a,0}_q + J^a_{H_2} h^{g,a,0}_{H_2} + J^a_{\mathrm{H_2O}} h^{g,a,0}_{\mathrm{H_2O}} = \\ & J'^{g,a,1}_q + J^a_{H_2} h^{g,a,1}_{H_2} + J^a_{\mathrm{H_2O}} h^{g,a,1}_{\mathrm{H_2O}} + j(\phi^{g,a,1} - \phi^{g,a,0}) \end{aligned} \tag{6.1}$$

The voltage difference over the backing is:

$$\phi^{g,a,1} - \phi^{g,a,0} = -\pi^{g,a} \Delta T - t^{g,a}_{\mathrm{H_2O}} \Delta \mu_{\mathrm{H_2O}} - r^b d^b j \tag{6.2}$$

Assuming that $\pi^{g,a} = 0$ and $\Delta \mu_{\mathrm{H_2O}} = 0$, the produced energy is given as: $j(\phi^{g,a,1} - \phi^{g,a,0}) = j^2 r^b d^b$. The heat balance over the anode backing is then:

$$\begin{aligned} & J'^{g,a,0}_q + J^a_{H_2}(h^{g,a,0}_{H_2} - h^{g,a,1}_{H_2}) + J^a_w(h^{g,a,0}_w - h^{g,a,1}_w) = \\ & J'^{g,a,1}_q + j^2 r^b \end{aligned} \tag{6.3}$$

If the enthalpy-changes are small, the energy balance is:

$$J_q'^{g,a,0} = J_q'^{g,a,1} + j^2 r^b d^b \tag{6.4}$$

The heat flux J_q' in the system is a function of the temperature gradient $(\frac{dT}{dx})$, the gradient in chemical potential of water $(\frac{d\mu_{H_2O,T}}{dx})$ and gradient in electrical potential $(\frac{d\phi}{dx})$. The current density is proportional to the electric potential. The heat flux in the backing can then be described in the following way:

$$J_q' = -\lambda^{g,a}\frac{dT}{dx} - l_{qw}^{g,a}\frac{d\mu_{H_2O,T}}{dx} + \pi^{g,a}\frac{j}{\mathrm{F}} \tag{6.5}$$

where λ is the thermal conductivity of the backing, $l_{qw}^{g,a}$ is an Onsager coefficient defined in chapter 5 and $\pi^{g,a}$ is the Peltier heat for the same system. Here we assume that: $l_{qw}^{g,a} \approx 0$ and $\pi^{g,a} \approx 0$.

6.2.2 The anode surface

The energy balance for the anode surface is more complicated than the balances for the bulk faces in the fuel cell (sections 6.2.1, 6.2.3 and 6.2.5). Heat is still produced from ohmic resistance and current flow through the anode surface, but heat will also be produced due to irreversibilities in the surface, impeding the anode reaction. This process is normally denoted the activation overpotential. Heat will also evolve due to the condensation of water vapour at the electrode. For the anode surface reaction, the overpotential is quite low at small current densities and increases almost linearly at higher current densities. The energy balance for the anode surface is presented in equation (6.6).

$$\begin{aligned} J_q'^{g,a} + J_{H_2}^a h_{H_2}^{g,a} + J_{H_2O}^a h_{H_2O(g)} x_{H_2O(g)}^{g,a,1} + J_{H_2O}^a h_{H_2O(l)}^{m,a}(1 - x_{H_2O(g)}^{g,a,1}) \\ = J_q'^{m,a} + j(\phi^{m,a} - \phi^{g,a}) + J_{H_2O}^a h_{H_2O(l)}^m \end{aligned} \tag{6.6}$$

$x_{H_2O(g)}^{g,a,1}$ is the mole fraction of water transported as gas through the backing. The energy producing term in the equation above is still $j(\phi^{m,a} - \phi^{g,a})$:

$$\begin{aligned} \phi^{m,a} - \phi^{g,a} \quad = \quad & -\frac{1}{\mathrm{F}}(\mu_H^{s,a} - \frac{1}{2}\mu_{H_2}^{g,a}) - \frac{\pi^{s,a}}{\mathrm{F}\,(T^{s,a})}\left(T^{m,a} - T^{g,a,1}\right) \\ & -r^{s,a} j \end{aligned} \tag{6.7}$$

The overvoltage, η^a, is expressed as:

$$\eta^a = \frac{1}{\mathrm{F}}\mu_{\mathrm{H}}^{s,a} + r^{s,a}j \tag{6.8}$$

The Butler-Volmer equation gives values for the overpotential (appendix B). We then obtain the following expression for the heat-balance over the anode surface:

$$\begin{aligned} J_q'^{m,a} &= J_q'^{g,a,1} + \frac{j}{2\mathrm{F}}h_{\mathrm{H}_2} + \frac{\alpha j}{2\mathrm{F}}x_{\mathrm{H}_2\mathrm{O}(g)}^{g,a,1}\Delta\mathrm{H}_{\mathrm{H}_2\mathrm{O}}^{vap,m,a} - \frac{j}{2\mathrm{F}}\mu_{\mathrm{H}_2}^{g,a} \\ &\quad + \pi^{s,a}j\frac{T^{m,a,} - T^{g,a,1}}{T^{s,a}F} + \eta^a j \end{aligned} \tag{6.9}$$

where α denotes the net water flux through the membrane relative to the reacted hydrogen $\left(F_{\mathrm{H}_2\mathrm{O}}^a/F_{\mathrm{H}_2}\right)$. $\Delta\mathrm{H}_{\mathrm{H}_2\mathrm{O}}^{vap,m,a}$ is assumed similar to $\Delta\mathrm{H}_{\mathrm{H}_2\mathrm{O}}^{vap}$. The heat-fluxes in and out of the surface, can be calculated from equations (6.10) and (6.11), given in chapter 5.

$$J_q'^{g,a} = -l_{qq}^{a,g}\frac{\Delta T^{g,a}}{T^{g,a}} - l_{qw}^{a,g}\Delta\mu_{w,T}^{g,a} + \pi^a\frac{j}{\mathrm{F}} \tag{6.10}$$

$$J_q'^{m,a} = -l_{qq}^{a,m}\frac{\Delta T^{m,a}}{T^{m,a}} - l_{qw}^{a,m}\Delta\mu_{w,T}^{m,a} + \pi^m\frac{j}{\mathrm{F}} \tag{6.11}$$

The coefficients in equations (6.10) and (6.11) include the common factor $1/T^{s,a}$. The differences in temperature for the membrane and gas phase is defined like this:

$$\begin{aligned} \Delta T^{g,a} &= T^{s,a} - T^{g,a} \\ \Delta T^{m,a} &= T^{m,a} - T^{s,a} \end{aligned}$$

By assuming that $l_{qw}^{a,g} \approx 0$ and $l_{qw}^{a,m} \approx 0$ the heat-fluxes are:

$$J_q'^{g,a} = -\lambda^{g,s}\Delta T^{g,a} + \pi^a\frac{j}{\mathrm{F}} \tag{6.12}$$

$$J_q'^{m,a} = -\lambda^{m,s}\Delta T^{m,a} + \pi^m\frac{j}{\mathrm{F}} \tag{6.13}$$

6.2.3 The membrane

The energy balance in the membrane can be described similarly to the energy balance in the anode backing (section 6.2.1). Heat is produced and transported in the membrane due to ohmic resistance, concentration gradients and temperature gradients:

$$\left(\phi^{m,c}-\phi^{m,a}\right)j=\left[-\frac{\pi^m}{\mathrm{F}}\ln\frac{T^{m,c}}{T^{m,a}}-\frac{t^m_{\mathrm{H_2O}}}{\mathrm{F}}\Delta\mu^m_{\mathrm{H_2O}}-r_m d_m j\right]j \tag{6.14}$$

The energy balance is then described with the following equation:

$$J'^{m,a}_q+J^m_{\mathrm{H_2O}}(h^{m,a}_{\mathrm{H_2O}}-h^{m,c}_{\mathrm{H_2O}})=J'^{m,c}_q+j\left(\phi^{m,c}-\phi^{m,a}\right) \tag{6.15}$$

The enthalpy difference of water is assumed to be zero. The heat flux is defined from equation (6.5), with phenomenological coefficients specific for the membrane: $l_{qw}\approx 0$ and $\pi^m\approx 0$.

6.2.4 The cathode surface

The cathode surface has a similar energy balance compared to the anode surface. The energy produced is similar, but more heat is dissipated due to a higher overpotential. Heat may be consumed due to evaporation of water. The energy balance is then:

$$\begin{aligned}J'^{m,c}_q+J^a_{\mathrm{H_2O}}h^m_{\mathrm{H_2O}(l)}+j\phi^{m,c}&=J'^{g,c,1}_q+J^c_{\mathrm{H_2O}}h_{\mathrm{H_2O}(g)}x^{g,c,1}_{\mathrm{H_2O}(g)}\\&+J^c_{\mathrm{H_2O}}h^{m,c}_{\mathrm{H_2O}(l)}(1-x^{g,c,1}_{\mathrm{H_2O}(g)})+J_{\mathrm{O_2}}h_{\mathrm{O_2}}+j\phi^{g,c,1}\end{aligned} \tag{6.16}$$

where $x^{g,c,1}_{\mathrm{H_2O}(g)}$ is the mole fraction of water vapour released at the cathode surface. The voltage difference can be interpreted in the same way as the voltage difference for the anode surface (equation (6.7)):

$$\begin{aligned}\phi^{g,c,1}-\phi^{m,c}&=-\frac{1}{\mathrm{F}}(\frac{1}{2}\mu^{g,c}_w-\mu^{s,c}_H-\frac{1}{4}\mu^{g,c}_{O_2})\\&-\frac{\pi^{s,c}}{T^{s,c}\mathrm{F}}\left(T^{g,c,1}-T^{m,c}\right)-r^{s,c}j\end{aligned} \tag{6.17}$$

Similarly to section 6.2.2, the cathode overvoltage, η^c, is expressed as:

$$\eta^c = -\mu_{\mathrm{H}}^{s,c} + r^{s,a} j \tag{6.18}$$

The heat balance is then:

$$\begin{aligned} J_q'^{g,c,1} \quad = \quad & J_q'^{m,c} + \frac{j}{\mathrm{F}}\left(\frac{1}{4}h_{\mathrm{O}_2} - \frac{1}{2}h_{\mathrm{H_2O(l)}}\right) - \frac{(\alpha+1)j}{2\mathrm{F}}\Delta\mathrm{H}_{\mathrm{H_2O}}^{vap,m,c} x_{\mathrm{H_2O}}^{g,c,1} \\ & + \frac{\pi^{s,c} j}{T^{s,c}\mathrm{F}}\left(T^{g,c,1} - T^{m,c}\right) + \frac{j}{\mathrm{F}}\left(\frac{1}{2}\mu_{\mathrm{H_2O(l)}}^{g,c,1} - \frac{1}{4}\mu_{\mathrm{O}_2}^{g,c,1}\right) \\ & + \eta^c j \end{aligned} \tag{6.19}$$

$\Delta\mathrm{H}_{\mathrm{H_2O}}^{vap,m,c}$ is assumed similar to $\Delta\mathrm{H}_{\mathrm{H_2O}}^{vap}$. The heat fluxes in the cathode surface is defined:

$$J_q'^{m,c} = -l_{qq}^{c,m}\frac{\Delta T^{m,c}}{T^{m,c}} - l_{qw}^{c,m}\Delta\mu_{w,T}^{m,c} + \pi^m \frac{j}{\mathrm{F}} \tag{6.20}$$

$$J_q'^{g,c} = -l_{qq}^{c,g}\frac{\Delta T^{g,c}}{T^{g,c}} - l_{qw}^{c,g}\Delta\mu_{w,T}^{g,c} + \pi^c \frac{j}{\mathrm{F}} \tag{6.21}$$

The temperature differences are:

$$\Delta T^{m,c} = T^{s,c} - T^{m,c}$$
$$\Delta T^{g,c} = T^{g,c} - T^{s,c}$$

By assuming that $l_{qw}^{c,m} \approx 0$ and $l_{qw}^{c,g} \approx 0$, the heat-fluxes are:

$$J_q'^{m,c} \quad = \quad -\lambda^{m,s}\Delta T^{m,c} + \pi^m \frac{j}{\mathrm{F}} \tag{6.22}$$

$$J_q'^{g,c} \quad = \quad -\lambda^{g,s}\Delta T^{g,c} + \pi^c \frac{j}{\mathrm{F}} \tag{6.23}$$

6.2.5 The cathode backing

The cathode gas diffusion backing is evaluated in the same way as the anode backing. The energy balance is presented in equation (6.24). The heat flux is defined from equation (6.5).

$$\begin{aligned} J_q'^{g,c,0} + J_{O_2}^c(h_{O_2}^{g,c,0} - h_{O_2}^{g,c,1}) = \\ J_q'^{g,c,1} + J_w^c(h_w^{g,c,1} - h_w^{g,c,0}) + j^2 r^b d^b \end{aligned} \tag{6.24}$$

If the variations in enthalpy are small across the backing, the energy balance simplifies to:

$$J_q'^{g,c,0} = J_q'^{g,c,1} + j^2 r^b d^b \tag{6.25}$$

The equations presented in this section can be used to calculate the temperature profile in the fuel cell. Thermal conductivities in the system can also be calculated, based on a measured temperature profile. The measurements of local temperatures are described in chapter 6.3.

6.3 Temperature measurements

6.3.1 Measurement system

The local temperatures in the polymer electrolyte fuel cell were measured at the four positions shown in figure 6.1:

Temp 1 The temperature at the end of the gas-flow channel at the anode side.

Temp 2 The temperature between the catalytic layer and the membrane on the anode side.

Temp 3 The temperature between the catalytic layer and the membrane on the cathode side.

Temp 4 The temperature at the end of the gas-flow channel at the cathode side.

The positions for Temp 1 to Temp 4 were chosen due to the relative simplicity of the measurement and based on the calculated temperature profile in chapter 5, figure 5.6. From this figure we should expect the largest temperatures close to the membrane.

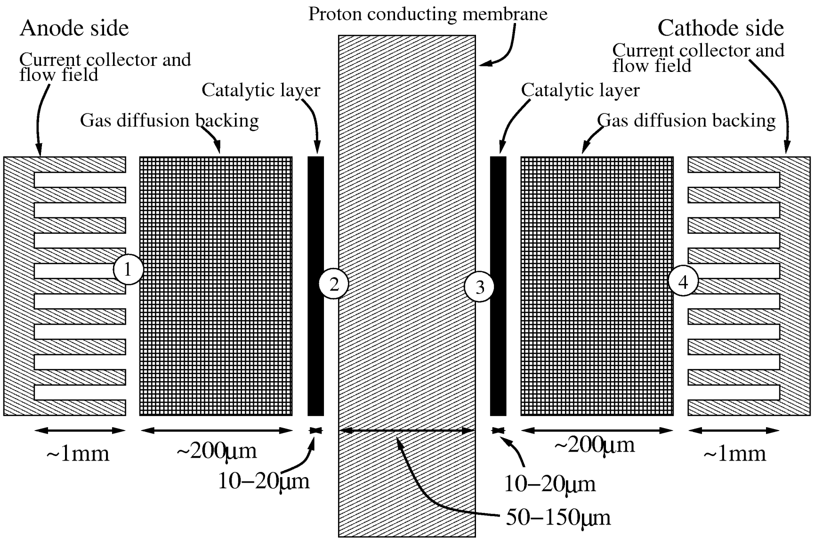

Figure 6.1: A schematic drawing of the polymer fuel cell and the positions for the temperature measurements in the fuel cell. The dimensions in the system are not in scale.

6.3.2 Experimental

All experiments were performed with the fuel cell test-facility presented in chapter 2. Thermocouples of type K, wire-thickness 120 μm (AWG 36), were prepared as described in appendix C.

The electrodes were produced with the same technique as discussed in chapter 3, but this time the slurry was sprayed on the gas diffusion backing[1]. The loading of platinum on the electrode was 0.1 mg/cm^2, and the Nafion content in the dry electrode was 35 wt%. The proton-conducting membrane was a Nafion®115 membrane prepared as described by Møller-Holst [1996b].

The membrane and electrode assembly (MEA) was assembled with two isolated thermocouples in a sandwich on each side of the membrane (Temp 2 and 3), inside the electrodes. Two more thermocouples were positioned in the gas channels (Temp 1 and 4).

The reacting gases, pure hydrogen and oxygen, were humidified at 80 °C,

---

[1] ETEK Elat® double-sided, carbon only

and the gas pressures were 4.5 bara. At atmospheric pressures the measured temperatures were generally more unstable, compared to elevated gas pressures. The partial pressures of hydrogen and oxygen increased, and problems with condensing water were reduced. The gas flow-rates varied according to the conversion of the gases and were set to give a conversion of the gases of approximately 50 %. To avoid unstable gas pressures, the minimum gas flow was otherwise set to 30 ml$_N$/min. The MEA was compressed in the fuel cell housing with a mechanical pressure of around 10 bar. The fuel cell housing was heated in order to give a temperature in the gas channels of ~64 °C at open circuit. See chapter 2 for details on the fuel cell heating elements.

6.3.3 Results and discussion

Local temperatures

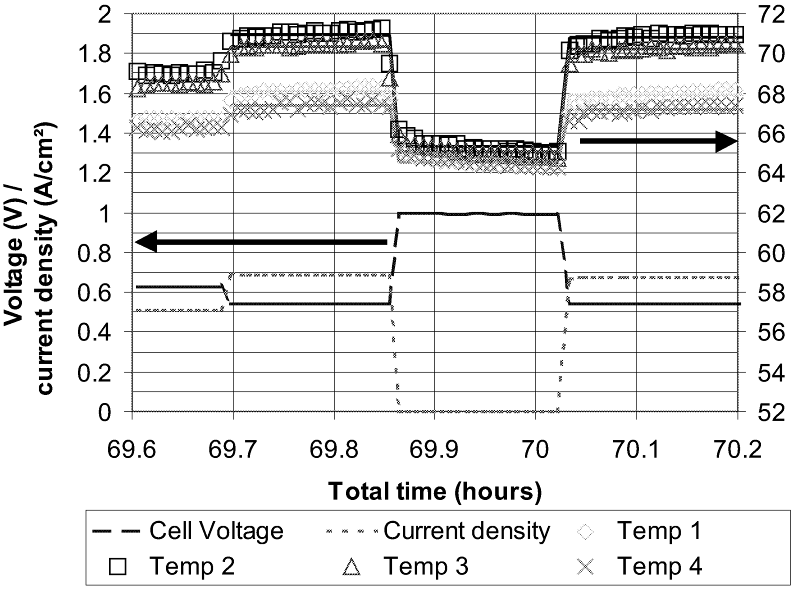

Figure 6.2: This graph shows a typical temperature measurement in the polymer fuel cell. The positions of the thermocouples are presented in figure 6.1.

The temperatures were measured at different current densities. An example of a typical measurement is presented in figure 6.2. The voltage varied in steps from 0.63 V to 0.54 V then to OCV (∼1 V) and back to 0.54 V. This corresponds to a current density increasing from approximately 0.5 A/cm^2 to 0.68 A/cm^2, then to 0 A/cm^2 and back to 0.67 A/cm^2. Four temperatures were measured simultaneously, and we observed that the temperatures varied correspondingly. When the current density dropped, the temperatures also dropped. Consequently the temperature increased when the current density increased. This observation was expected, due to the dissipation of heat in the fuel cell. At OCV, the temperatures stabilised around 64 to 65 ^{o}C.

It is interesting to notice that the temperature on the anode increases as much as the temperature on the cathode. This may be due to the relative positions of the temperature sensing spot (measuring junction) of the thermocouple. The cathode sensor could face away from the heat producing area, while the anode sensor could face towards the warmest parts. Since the elements used here are quite large, the exact positions for temperature measurements is not known. See figure 6.3 for a sketch on the possible location of Temp 2 or 3. Another explanation is that water is condensing at the anode and evaporating at the cathode. This will heat the anode and cool the cathode. However, more heat is produced on the cathode due to higher cathodic overpotentials. This may compensate for the heat of evaporation rendering equal anode and cathode temperatures.

Due to the size of the thermocouples in this experiment, the sensors will affect the system to a large extent. The thermocouples close to the membrane (Temp 2 and 3) block some of the active surface area. Consequently, less heat will be produced from the fuel cell reaction close to the thermocouples. This means that the temperature measured are lower than the real temperature, if the system had been left undisturbed. There are no data on how much this reduce the “true” temperature. These temperature measurements give therefore mainly qualitative measures of temperature jumps inside the fuel cell.

The average temperatures were calculated at stable temperatures. Correlations between measured temperatures and the current density were thus obtained.

The temperature variation

The correlation between temperature and current density was found by varying the cell voltage in different patterns and voltage jumps, and repeating several of the measurements. In figure 6.4 the measured temperatures are correlated

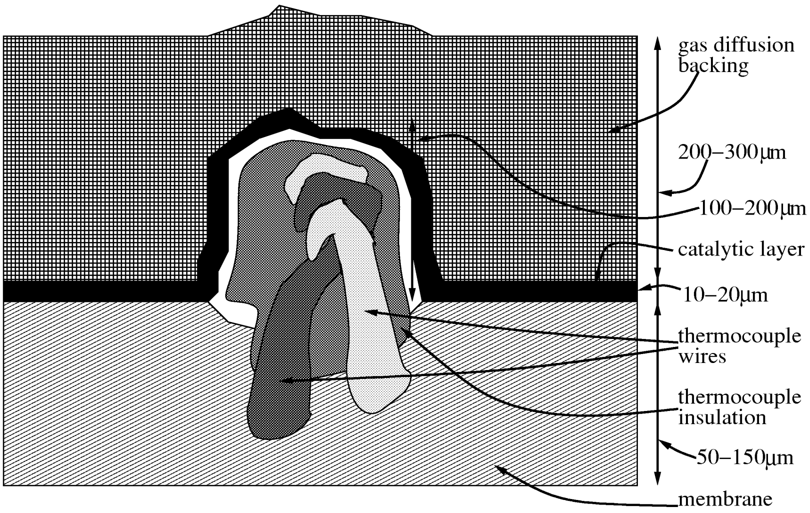

Figure 6.3: A sketch of a probable location of a thermocouple. To give room for the thermocouple, the other components are compressed. The gas diffusion backing is very flexible and gives room for most of the thermocouple.

with the corresponding current density. The models chosen were 2nd order polynomials, see equation (6.26). These models fit quite well to the measured temperatures. See table 6.1 for the model coefficients and statistical data. The heat produced in an electrical wire is known to be proportional to the current squared. We have a similar relationship in equation (6.4), giving a rationale for the 2nd order behaviour in figure 6.4.

$$T_i = a_i + b_i \cdot j + c_i \cdot j^2 \tag{6.26}$$

The polarisation curve in figure 6.5 is fairly smooth with little scatter. This indicates that the conditions in the fuel cell were similar for each measured current density and that stationary states were obtained (see also figure 6.2). The data were fitted to an empirical model based on the Butler-Volmer equation (appendix B). Data in the range 0 - 0.75 A/cm^2 were included in the model-fit. Values for the exchange current densities at the anode and cathode, and total fuel cell resistance were estimated: $j^0_{\mathrm{O}_2} = 2.5 \cdot 10^{-7}$ A/cm^2, $j^0_{\mathrm{H}_2} = 4.2 \cdot 10^{-1}$ A/cm^2 and $r_{tot} = 0.31$ Ωcm^2. These values are the basis for the

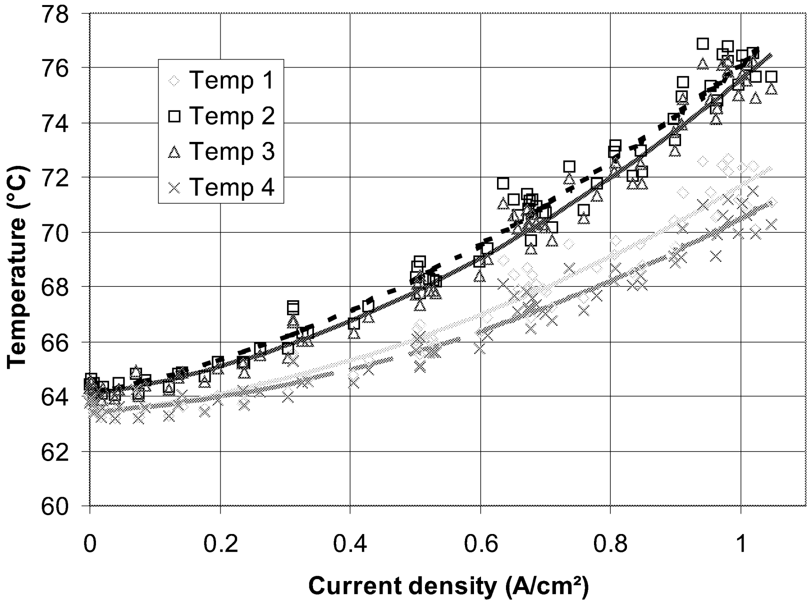

Figure 6.4: The measured temperatures as a function of the current density. The data were fitted to models (equation (6.26)) for each temperature position, and plotted as lines in the figure. The data for the models are presented in table 6.1.

overpotential curves in figure 6.5. The standard deviation for the fitted curve was 0.024 V. At higher current densities we observe a steeper drop in fuel cell voltage. A drier membrane or mass transport limitations may explain this, but these effects were not included in the calculation.

6.4 Thermal conductivities

Thermal conductivities inside the fuel cell can be calculated from the measured temperature profiles. In chapter 5, a temperature profile with 8 temperatures was calculated. The measured temperatures and the size of the thermocouples used, indicate that a profile with fewer temperatures should be applied. The temperatures in the anode and cathode layers ($T^{s,a}$, $T^{s,c}$) are hard to define

Table 6.1: The statistical data and coefficients for the models in figure 6.4. The data were fitted to equation (6.26). "s" is the standard deviation for the model and "r^2" is the correlation coefficient.

	Temp 1	Temp 2	Temp 3	Temp 4
a_i (^{o}C)	63.34	64.13	64.06	63.45
b_i $\left(\frac{^o\mathrm{C}}{\mathrm{A/cm^2}}\right)$	2.60	4.63	3.49	1.67
c_i $\left(\frac{^o\mathrm{C}}{(\mathrm{A/cm^2})^2}\right)$	5.74	7.32	8.03	5.38
s_i (^{o}C)	0.69	0.66	0.60	0.52
r_i^2	0.95	0.98	0.98	0.96

and measure. Consequently, it is reasonable to assume that the electrodes have the same temperature as either the backing or membrane close to electrodes.

Water transported from the electrode to the membrane is assumed to pass as liquid both on the anode and the cathode side. In the backings, water may be transported as both liquid and vapour. The thermal conductivity is therefore much higher between electrode and membrane than between electrode and backing. Hence, we assume that $\Delta T^{m,c} = T^{s,c} - T^{m,c} = 0$ and $\Delta T^{m,a} = T^{s,a} - T^{m,a} = 0$.

6.4.1 Equations

From the equations in section 6.2 we derive the following set of 16 equations defining the heat balance in the fuel cell:

$$
\begin{aligned}
T^{g,a,0} &= T_1 && (6.27)\\
T^{s,a} &= T^{m,a} = T_2 && (6.28)
\end{aligned}
$$

$$
\begin{aligned}
T^{s,c} &= T^{m,c} = T_3 && (6.29)\\
T^{g,c,0} &= T_4 && (6.30)
\end{aligned}
$$

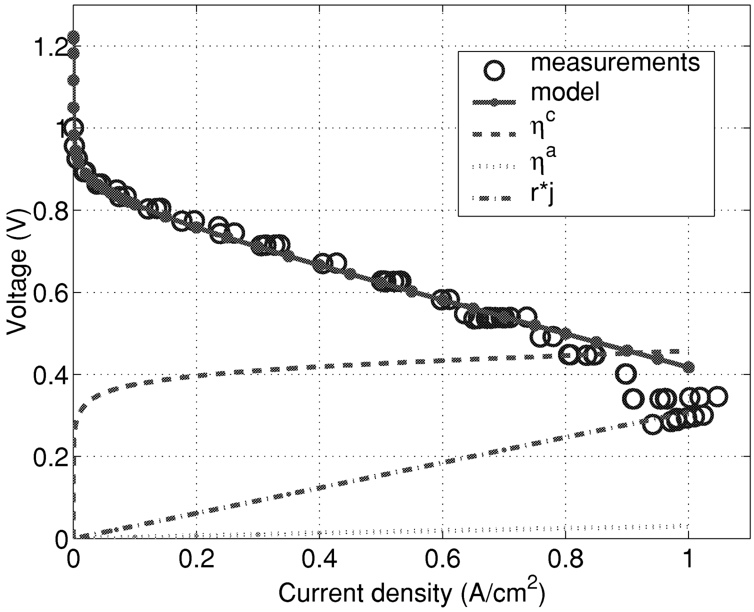

Figure 6.5: The polarisation curve for the data used in the temperature plot in figure 6.4. Curves for the fitted overpotentials at the anode (η^a) and cathode (η^c) and the total resistance ($r \cdot j$) is included.

$$J_q^{\prime g,a,1} = J_q^{\prime g,a,0} + j^2 r^b d^b \tag{6.31}$$

$$T^{g,a,1} = T^{g,a,0} - \frac{d^b}{\lambda^b} \cdot \left[\frac{1}{2}\left(J_q^{\prime g,a,0} + J_q^{\prime g,a,1}\right)\right] \tag{6.32}$$

$$\begin{aligned} J_q^{\prime m,a} = {} & J_q^{\prime g,a,1} + j\eta^a + J_{\mathrm{H_2O}}^a x_{\mathrm{H_2O}}^{cond,a} \Delta H_{\mathrm{H_2O}}^{vap} \\ & + \frac{j}{2F} T^{s,a} S_{\mathrm{H_2}} + 2\pi^{s,a} \frac{j}{F} \frac{T^{m,a} - T^{g,a,1}}{T^{m,a} + T^{g,a,1}} \end{aligned} \tag{6.33}$$

$$T^{s,a} = T^{g,a,1} - \frac{1}{\lambda^{s,g}} \left[J_q^{\prime g,a,1} - \pi^{s,a} \frac{j}{F}\right] \tag{6.34}$$

$$J_q^{\prime m,c} = J_q^{\prime m,a} + j^2 r^m d^m + \pi^m \frac{j}{F} \ln \frac{T^{m,c}}{T^{m,a}} + \frac{j}{F} t_{\mathrm{H_2O}}^m \Delta \mu_{\mathrm{H_2O},T}^m \tag{6.35}$$

$$\begin{aligned}
T^{m,c} &= T^{m,a} - \frac{d^m}{\lambda^m}\left[\frac{1}{2}(J_q'^{m,a} + J_q'^{m,c}) - \pi^m \frac{j}{F}\right] && (6.36)\\
J_q'^{g,c,1} &= J_q'^{m,c} + j\eta^c - J^c_{\mathrm{H_2O}} x^{vap,c}_{\mathrm{H_2O}} \Delta H^{vap}_{\mathrm{H_2O}} \\
&\quad + \pi^{s,c}\frac{j}{F}\left(\frac{T^{g,c,1} - T^{s,c}}{T^{s,c}}\right) + \frac{j}{F}T^{s,c}\left(\frac{1}{4}S_{\mathrm{O_2}} - \frac{1}{2}S_{\mathrm{H_2O(l)}}\right) && (6.37)
\end{aligned}$$

$$\begin{aligned}
T^{g,c,1} &= T^{s,c} - \frac{1}{\lambda^{s,g}}\left[J_q'^{g,c,1} - \pi^{s,c}\frac{j}{F}\right] && (6.38)\\
J_q'^{g,c,0} &= J_q'^{g,c,1} + j^2 r^b d^b && (6.39)\\
T^{g,c,0} &= T^{g,c,1} - \frac{d^b}{\lambda^b}\left[\frac{1}{2}(J_q'^{g,c,0} + J_q'^{g,c,1})\right] && (6.40)
\end{aligned}$$

The Peltier heats in the system are defined in chapter 5.

By introducing equation (6.31) into equations (6.33), (6.35), (6.37) and (6.39), solving for $J_q'^{g,a,0}$ we obtain the following equations: (Peltier heats are neglected since the included entropies are larger than the Peltier heats, and they will therefore contribute less to the solution.)

$$\begin{aligned}
J_q'^{m,a} &= J_q'^{g,a,0} + j^2 r^b d^b + j\eta^a + J^a_{\mathrm{H_2O}} x^{cond,a}_{\mathrm{H_2O}} \Delta H^{vap}_{\mathrm{H_2O}} \\
&\quad + \frac{j}{2F}T^{s,a}S_{\mathrm{H_2}} && (6.41)\\
J_q'^{m,c} &= J_q'^{g,a,0} + j^2(r^b d^b + r^m d^m) + j\eta^a + J^a_{\mathrm{H_2O}} x^{cond,a}_{\mathrm{H_2O}} \Delta H^{vap}_{\mathrm{H_2O}} \\
&\quad + \frac{j}{2F}T^{s,a}S_{\mathrm{H_2}} && (6.42)
\end{aligned}$$

$$\begin{aligned}
J_q'^{g,c,1} &= J_q'^{g,a,0} + j^2(r^b d^b + r^m d^m) + j(\eta^a + \eta^c) \\
&\quad + \Delta H^{vap}_{\mathrm{H_2O}}\left[J^a_{\mathrm{H_2O}} x^{cond,a}_{\mathrm{H_2O}} - J^c_{\mathrm{H_2O}} x^{vap,c}_{\mathrm{H_2O}}\right] \\
&\quad + \frac{j}{F}\left[T^{s,a}\frac{1}{2}S_{\mathrm{H_2}} + T^{s,c}\left(\frac{1}{4}S_{\mathrm{O_2}} - \frac{1}{2}S_{\mathrm{H_2O(l)}}\right)\right] && (6.43)\\
J_q'^{g,c,0} &= J_q'^{g,a,0} + j^2(2r^b d^b + r^m d^m) + j(\eta^a + \eta^c) \\
&\quad + \Delta H^{vap}_{\mathrm{H_2O}}\left[J^a_{\mathrm{H_2O}} x^{cond,a}_{\mathrm{H_2O}} - J^c_{\mathrm{H_2O}} x^{vap,c}_{\mathrm{H_2O}}\right] \\
&\quad + \frac{j}{F}\left[T^{s,a}\frac{1}{2}S_{\mathrm{H_2}} + T^{s,c}\left(\frac{1}{4}S_{\mathrm{O_2}} - \frac{1}{2}S_{\mathrm{H_2O(l)}}\right)\right] && (6.44)
\end{aligned}$$

We can now reduce the system of equations to:

$$\begin{aligned}
T^{g,a,1} &= T^{g,a,0} - \frac{d^b}{\lambda^b}\left[J'^{g,a,0}_q + \frac{1}{2}j^2 r^b d^b\right] && (6.45)\\
T^{s,a} &= T^{g,a,1} - \frac{1}{\lambda^{s,g}}\left[J'^{g,a,0}_q + j^2 r^b d^b - \frac{j}{F}\pi^{s,a}\right] && (6.46)\\
T^{m,c} &= T^{m,a} - \frac{d^m}{\lambda^m}\left[J'^{g,a,0}_q + j^2(r^b d^b + \frac{1}{2}r^m d^m) + j\eta^a\right.\\
&\quad \left. + J^a_{\mathrm{H_2O}} x^{cond,a}_{\mathrm{H_2O}} \Delta H^{vap}_{\mathrm{H_2O}} + \frac{j}{F}\left(\frac{1}{2}T^{s,a}S_{\mathrm{H_2}} - \pi^m\right)\right] && (6.47)
\end{aligned}$$

$$\begin{aligned}
T^{g,c,1} &= T^{s,c} - \frac{1}{\lambda^{s,g}}\left[J'^{g,a,0}_q + j^2(r^b d^b + r^m d^m) + j(\eta^a + \eta^c)\right.\\
&\quad + \Delta H^{vap}_{\mathrm{H_2O}}\left[J^a_{\mathrm{H_2O}} x^{cond,a}_{\mathrm{H_2O}} - J^c_{\mathrm{H_2O}} x^{vap,c}_{\mathrm{H_2O}}\right]\\
&\quad \left. + \frac{j}{F}\left(T^{s,a}\frac{1}{2}S_{\mathrm{H_2}} + T^{s,c}\left(\frac{1}{4}S_{\mathrm{O_2}} - \frac{1}{2}S_{\mathrm{H_2O(l)}}\right) - \pi^{s,c}\right)\right] && (6.48)\\
T^{g,c,0} &= T^{g,c,1} - \frac{d^b}{\lambda^b}\left[J'^{g,a,0}_q + j^2(\frac{3}{2}r^b d^b + r^m d^m) + j(\eta^a + \eta^c)\right.\\
&\quad + \Delta H^{vap}_{\mathrm{H_2O}}\left[J^a_{\mathrm{H_2O}} x^{cond,a}_{\mathrm{H_2O}} - J^c_{\mathrm{H_2O}} x^{vap,c}_{\mathrm{H_2O}}\right]\\
&\quad \left. + \frac{j}{F}\left(T^{s,a}\frac{1}{2}S_{\mathrm{H_2}} + T^{s,c}\left(\frac{1}{4}S_{\mathrm{O_2}} - \frac{1}{2}S_{\mathrm{H_2O(l)}}\right)\right)\right] && (6.49)
\end{aligned}$$

These five equations define the heat balance in the polymer fuel cell in addition to the boundary conditions in equations (6.27) to (6.30). The system was solved by iteration. A start value for $J'^{g,a,0}_q$ was guessed and values for $T^{g,a,1}$ and $T^{g,c,1}$ was calculated from equations (6.45) and (6.49). Further $\lambda^{s,g}$ was calculated from (6.46) and (6.48). The solution of the system was found when a value of $J'^{g,a,0}_q$ gave the same solution for $\lambda^{s,g}$ in both equations. Then λ^m was calculated from equation (6.47).

The following data were used as a basis in the calculations:

- $r^b = 1{\cdot}10^{-4}\ \Omega\mathrm{m}$

- $d^b = 180$ μm [Springer et al., 1996]
- $\lambda^b = 10$ W/mK
- r^m from modelled results in chapter 5 and appendix A
- $d^m = 127$ μm (Nafion® 115 membrane)
- Thermodynamic data were taken from Lide [1990]

These values are similar to the values used in chapter 5.

6.4.2 Results and discussion

The thermal conductivity of the membrane (λ^m) and the heat transfer coefficients of the electrodes ($\lambda^{s,g}$) were calculated by iteration of the system of equations presented above (section 6.4.1). The calculated results are presented in table 6.2. We assumed that all water condensed at the anode electrode surface ($x_{\mathrm{H_2O}}^{cond,a} = 1$). This is likely since the state of water in the membrane is a condensed phase. Due to the hydrophobicity of the gas diffusion backing, the water may be transported as vapour through the backing.

At the cathode side, the aggregate state of water is more unpredictable. If the cathode gas is supersaturated with water vapour, evaporation at the cathode electrode surface should not occur. The backing is both hydrophobic and porous. The hydrophobic character of the backing promotes a vapour phase, whereas the high porosity promotes a liquid phase. Since there is a temperature gradient through the backing, the balance between the two may change. It is thus not clear if the produced water is transported as liquid or gas through the backing. However, the oxygen gas is supersaturated with water, and all produced water will condense entering the cathode gas channel. The fraction of water evaporating at the cathode catalyst layer was therefore varied, but the supersaturated conditions in the cathode gas channel indicate that $x_{\mathrm{H_2O}}^{vap,c} = 0$.

Heat-transfer coefficient of the electrodes

The calculated values for $\lambda^{s,g}$ are not constant in the calculated current density range. The reason for the variation is probably the relatively low accuracy of the temperature measurements at low current densities. The standard deviation for the measured temperatures is approximately 0.6 °C (table 6.1).

Table 6.2: λ^m and $\lambda^{s,g}$ calculated at various current densities (j) and with varying values for $x_{\mathrm{H_2O}}^{vap,c}$. $\bar{\lambda}$ is the average value of λ, s is the standard deviation.

j (A/cm^2)	λ^m (W/mK)			$\lambda^{s,g}$ (W/m^{2}K)		
	$x_{\mathrm{H_2O}}^{vap,c} = 0$	$x_{\mathrm{H_2O}}^{vap,c} = 0.5$	$x_{\mathrm{H_2O}}^{vap,c} = 1$	$x_{\mathrm{H_2O}}^{vap,c} = 0$	$x_{\mathrm{H_2O}}^{vap,c} = 0.5$	$x_{\mathrm{H_2O}}^{vap,c} = 1$
0.1	-0.10	-0.03	0.04	450	350	260
0.2	-0.13	-0.06	0.02	710	580	440
0.3	-0.15	-0.07	0.02	880	730	580
0.4	-0.16	-0.07	0.02	1030	870	710
0.5	-0.17	-0.07	0.03	1110	950	780
0.6	-0.17	-0.07	0.04	1160	990	830
0.7	-0.18	-0.06	0.05	1180	1020	860
0.8	-0.19	-0.06	0.07	1200	1030	870
0.9	-0.20	-0.05	0.09	1210	1050	900
1.0	-0.21	-0.05	0.12	1210	1050	900
$\bar{\lambda}$	-0.17	-0.06	0.05	1010	860	710
s	0.03	0.01	0.03	260	240	220

This is the same as the temperature differences at lower current densities (< 0.2 A/cm^2). At higher current densities the variation in $\lambda^{s,g}$ is smaller. $\lambda^{s,g}$ is also varying with respect to the value of $x_{\mathrm{H_2O}}^{vap,c}$. Due to the large standard deviations, there are no significant differences for the average values. The fuel cell conditions during the experiments indicate that $x_{\mathrm{H_2O}}^{vap,c} = 0$. The heat transfer coefficient of the electrode ($\lambda^{s,g}$) is therefore reported to 1000 ± 300 W/m^{2}K.

Thermal conductivity of Nafion 115

The values of λ^m have smaller variations in the current density range. When $x_{\mathrm{H_2O}}^{vap,c} \leq 0.5$, the calculated values are negative. From equation (6.47) we observe that λ^m depends strongly on the temperature difference over the membrane. This difference is always small and in the same range as the standard deviation of the measured temperatures (figure 6.6). The calculated values will only give an indication of the order of magnitude. λ^m is positive when

$x_{\mathrm{H_2O}}^{vap,c} = 1$, but the uncertainties are still large. The thermal conductivity of the membrane has to be positive. λ^m is therefore assumed to have a value in the range 0.1 ± 0.1 W/mK.

The thermal conductivity of the Nafion membrane was estimated from the thermal conductivities of water and rubber (polymer). The thermal conductivity of water is 0.66 W/mK at 66 °C and rubber has a thermal conductivity of 0.15 W/mK [Geankoplis, 1983]. The conductivity of the Nafion membrane was found from an equation on mixed conductivities [Solheim, 2000; Maxwell, 1881]:

$$\lambda = \lambda_0 \frac{\lambda_{\mathrm{H_2O}} + 2\lambda_0 - 2\theta(\lambda_0 - \lambda_{\mathrm{H_2O}})}{\lambda_{\mathrm{H_2O}} + 2\lambda_0 + \theta(\lambda_0 - \lambda_{\mathrm{H_2O}})} \tag{6.50}$$

λ_0 is the thermal conductivity of the base polymer, here assumed similar to rubber. θ is the volume fraction of water in the hydrated membrane. θ was estimated to 0.12 interpolated from the swelling data of the Nafion membranes reported in chapter 4, table 4.1. The thermal conductivity of the Nafion 115 membrane was estimated to 0.18 W/mK, based on tabulated data. This value is in the range of the thermal conductivity calculated here.

Thermal conductivity of backing and electrode

The thermal conductivity can be estimated from equation (6.5), assuming a zero concentration gradient in water and a zero Peltier coefficient:

$$\lambda^b = -J_q'^{g,0} \frac{\Delta d^b}{\Delta T^b} \tag{6.51}$$

$J_q'^{g,0}$ is the heat flux out of the gas diffusion backing either on anode or cathode. The variation in heat flux over the backing is low due to the small resistance. In the electrode (10 μm) this is not the fact, but the electrode thickness is only about 5 % of the total thickness of electrode and backing. Equation (6.51) therefore gives an estimate of the thermal conductivity of the backing and electrode. The calculated thermal conductivities for both anode and cathode are presented in table 6.3 at different current densities. The combined thermal conductivity for the backing and electrode is 0.19 ± 0.05 W/mK.

The thermal conductivity of the backing can be estimated from an equation similar to equation (6.50), assuming that the backing is comparable to porous amorphous carbon black. The tabulated thermal conductivity of carbon/graphite varies from 1.5 W/mK (amorphous solid carbon) to 2130 W/mK

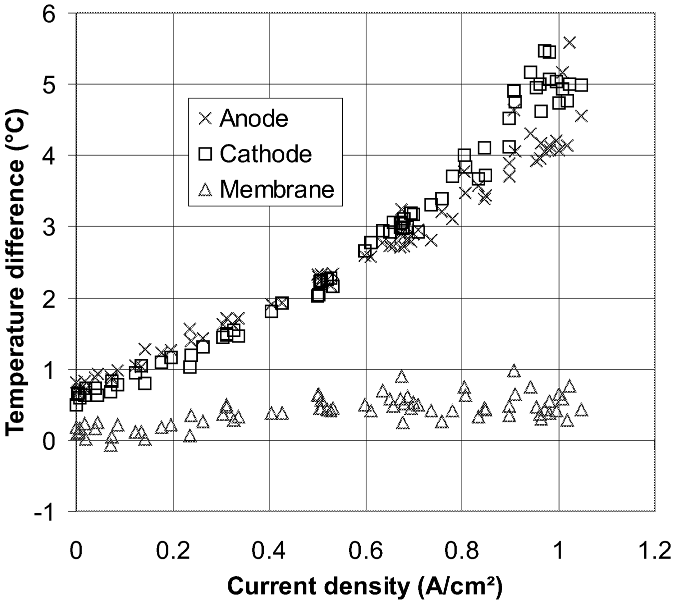

Figure 6.6: The temperature differences over anode, membrane and cathode.

(pyrolytic graphite) [Lide, 1990]. Ebert et al. [1998] reports that carbon-black can have a thermal conductivity as low as 0.030 W/mK at 27 °C in nitrogen atmosphere. There are no reports on the thermal conductivity of the backing in the literature to our knowledge. The porosity of the compressed gas diffusion backing is not well documented, but a porosity of 0.4 is suggested by Springer et al. [1996]. The gas phase is here assumed to be a mixture of 50 % gas (hydrogen/oxygen) and 50% water vapour. The thermal conductivity is then in the range of 0.33 W/mK to 0.40 W/mK, assuming a thermal conductivity of carbon black of 1 W/mK. The gas diffusion backing and electrode is even more complex. It consists of a plain weave carbon cloth (11.6 mg/cm^2), Vulcan XC-72 carbon black (1.4 mg/cm^2) and a hydrophobic fluorocarbon wet-proofing [E-TEK Div. of De Nora N.A., Inc.]. The fluorocarbon content is proprietary to E-TEK. The estimated value is therefore a rough estimate, but it is in the same range as the thermal conductivity calculated in table 6.3.

The values calculated and estimated for λ^b above are much smaller than the value presented in section 6.4.1. This value will affect the results for the

Table 6.3: Thermal conductivities of backing and electrode on anode ($\lambda^{b,a}$) and cathode ($\lambda^{b,c}$) calculated from equation (6.51). $\bar{\lambda}$ is the average value of λ, s is the standard deviation.

j (A/cm^2)	$\lambda^{b,a}$ (W/mK)	$\lambda^{b,c}$ (W/mK)
0.10	0.09	0.09
0.20	0.13	0.13
0.30	0.17	0.17
0.40	0.19	0.19
0.50	0.20	0.20
0.60	0.21	0.21
0.70	0.22	0.22
0.80	0.23	0.23
0.90	0.23	0.23
1.00	0.23	0.23
$\bar{\lambda}$	0.19	0.19
s	0.05	0.05

heat transfer coefficient at the electrode surface, and the reported heat transfer coefficient (1000 W/m^{2}K) should therefore be referenced to $\lambda^b = 10$ W/mK.

6.5 Conclusions

From the experiments performed in this chapter we conclude that the heat produced in the fuel cell, increase the local temperatures in different sections of the fuel cell. The highest temperatures are observed close to the electrodes.

The most frequent assumption for fuel cells is that of isothermal operation. It is clear from equation (6.5) that isothermal conditions require large thermal conductivities. The observations in figure 6.4 show that heat can accumulate locally. This means that the thermal conductivities of the system are not sufficient to conduct heat rapidly enough for isothermal cell conditions.

The reported measurements are uncertain, and the actual temperatures are probably larger than the temperatures reported here. Nevertheless, the temperature profiles can be understood. They give input to a theoretical model that has been used to calculate thermal conductivities in the different sections of the polymer fuel cell. This model contains thermal effects from the electrode overpotentials and the phase transition of water as substantial parts. On this basis, the thermal conductivity of the membrane (λ^m) was calculated to 0.1 ± 0.1 W/mK. The heat transfer coefficient of the electrodes ($\lambda^{s,g}$) was calculated to 1000 ± 300 W/m^{2}K, and the thermal conductivity of the backing was calculated to 0.19 ± 0.05 W/mK. The membrane and backing thermal conductivities are reasonable considering literature reports on similar materials. The electrode surface heat transfer coefficient is not previously reported in the literature.

Bibliography

G. J. K. Acres. Recent advances in fuel cell technology and its applications. *Journal of Power Sources*, 100:60–66, 2001.

O. J. Adlhart and P. L. Terry. Ammonia-air fuel cell system. *Engelhard-Industries-Technical-Bulletin*, 10(3):80–84, 1969.

M. Adžić, M. V. Heitor, and D. Santos. Design of dedicated instrumentation for temperature distribution measurements in solide oxide fuel cells. *Journal of Applied Electrochemistry*, 27:1355–1361, 1997.

A. M. Albano and D. Bedeaux. Nonequilibrium electro-thermodynamics of polarizable multicomponent fluids with an interface. *Physica A*, 147(1-2): 407–435, 1987.

E. Antolini, L. Giorgi, A. Pozio, and E. Passalacqua. Influence of Nafion loading in the catalyst layer of gas-diffusion electrodes for PEFC. *Journal of Power Sources*, 77(2):136–142, 1999.

A. J. Appleby. Electrochemical energy - progress towards a cleaner future: lead/acid batteries and the competition. *Journal of Power Sources*, 53:187–197, 1995.

P. W. Atkins. *Physical Chemistry.* Oxford University Press, 6th edition, 1999.

G. H. Aylward and T. J. V. Findlay. *SI Chemical Data.* John Wiley & Sons, Hong Kong, 2nd edition, 1971.

F. N. Büchi, B. Gupta, O. Haas, and G. G. Scherer. Study of radiation-grafted FEP-g-polystyrene membranes as polymer electrolytes in fuel cells. *Electrochimica Acta*, 40(3):345–353, 1995.

D. Bedeaux. *Flow, Diffusion and Rate Processes*, volume 6 of *Advances in Thermodynamics*, chapter Nonequilibrium Thermodynamics of Surfaces. Taylor and Francis, 1992.

D. Bedeaux, A. M. Albano, and P. Mazur. Boundary conditions and nonequilibrium thermodynamics. *Physica A*, 82:438–462, 1976.

D. Bedeaux, L. F. J. Hermans, and T. Ytrehus. Slow evaporation and condensation. *Physica A*, 169:263–280, 1990.

D. Bedeaux and S. K. Ratkje. The dissipated energy of electrode surfaces : temperature jumps from coupled transport processes. *J. Electrochem. Soc.*, 143(3):767–779, 1996.

D. Bedeaux, J. A. M. Smit, L. F. J. Hermans, and T. Ytrehus. Slow evaporation and condensation. 2. A dilute mixture. *Physica A*, 182:388–418, 1992.

D. M. Bernardi and M. W. Verbrugge. A mathematical model of the solid-polymer-electrolyte fuel cell. *J. Electrochem. Soc.*, 139(9):2477–2491, 1992.

T. Besmann and R.Greer. Morphology of gamma-irradiated, low density, bulk polyethylene. *J. Polym. Sci., Pol. Phys.*, 13:527, 1975.

L. J. M. J. Blomen and M. N. Mugerwa, editors. *Fuel Cell Systems.* Plenum Press, New York, 1993.

D. Bloomfield, E. Behrin, and P. N. Ross. Ammonia-air fuel cell power plant systems analysis. Subcontract 5100201, Lawrence Livermore National Laboratory, 1982.

BMW. BMW 750hL, the ultimate clean machine. `http://www.bmwworld.com/models/750hl.htm`, March 2002.

J. O. Bockris and S. Srinivasan. *Fuel Cells: Their Electrochemistry.* McGraw-Hill, New York, 1969.

U. Bossel. *The Birth of the Fuel Cell 1835 - 1845.* European Fuel Cell Forum, Oberrohrdorf, Switzerland, 2000.

G. E. P. Box, W. G. Hunter, and J. S. Hunter. *Statistics for experimenters, An introduction to Design, Data Analysis, and Model Building.* J. Wiley & Sons, USA, 1978.

J. Brandrup, E. H. Immergut, and E. A. Grulke, editors. *Polymer Handbook.* Wiley Interscience, New York, 1999.

F. N. Büchi and G. G. Scherer. Investigation of the transversal water profile in Nafion membranes in polymer electrolyte fuel cells. *J. Electrochem. Soc.*, 148(3):A183–A188, 2001.

A. Chapiro. *Radiation Chemistry of Polymeric Systems.* Wiley-Interscience, New York, 1962.

K.-H. Choi, D.-H. Peck, C. S. Kim, D.-R. Shin, and T.-H. Lee. Water transport in polymer membranes for PEMFC. *Journal of Power Sources*, 86:197–201, 2000.

DaimlerChrysler. DaimlerChrysler vehicles demonstrate four different approaches to fuel cell technology. `http://media.daimlerchrysler.com/`, December 2001a.

DaimlerChrysler. NECAR: fast-forwarding to the future with the fuel cell. `http://media.daimlerchrysler.com/`, October 2001b.

S. R. de Groot and P. Mazur. *Non-equilibrium thermodynamics.* North-Holland, Amsterdam, 1962.

P. Delhaès and F. Carmona. *Chemistry and Physics of Carbon : A series of advances.*, volume 17, chapter Physical properties of noncrystalline carbons, pages 89–174. Marcel Dekker, New York, USA, 1981.

Dow Chemical Company. *Cyclotene, Advanced Electronics resins, Technical data.* Midland, MI, USA, 1997.

E-TEK Div. of De Nora N.A., Inc. Company homepage. `http://www.etek-inc.com/`, February 2002.

H.-P. Ebert, B. Laudensack, F. Hemberger, O. Nilsson, and J. Fricke. Thermal insulations based on carbon black. *High Temperatures, High Pressures*, 30 (3):261–267, 1998.

B. Efron and R. J. Tibshirani. *An introduction to the Bootstrap.* Chapman & Hall, USA, 1993.

M. W. Ellis, M. R. von Spakovsky, and D. J. Nelson. Fuel cell systems: Efficient, flexible energy conversion for the 21st century. In *Proceedings of the IEEE*, volume 89, pages 1808–1818. IEEE, December 2001.

K. S. Førland, T. Førland, and S. K. Ratkje. *Irreversible Thermodynamics, Theory and Applications.* John Wiley & Sons, Lodon, 1988.

H. Fujimura, N. Kobayashi, and K. Ohtsuka. Heat and mass transfer in a moten carbonate fuel cell -Performance and temperature distribution in a cell stack. *JSME Internation journal. Series II*, 35(1):82–88, 1992.

T. F. Fuller and J. Newman. Water and thermal management in solid-polymer-electrolyte fuel cells. *J. Electrochem. Soc.*, 140(5):1218–1225, 1993.

R. C. Galloway and S. Haslam. The ZEBRA electric vehicle battery: power and energy improvements. *Journal of Power Sources*, 80(1-2):165–170, 1999.

C. J. Geankoplis. *Transport processes and unit operations.* Prentice Hall, Englewood Cliffs, NJ, 2nd edition, 1983.

J. W. Gibbs. *Collected Works*, volume 2. Dover, New York, 1961.

T. D. Gierke, G. E. Munn, and F. C. Wilson. The morphology in Nafion perfluorinated membrane products, as determined by wide- and small-angle X-ray studies. *J. Polym. Sci. Pol. Phys. ed.*, 19:1687, 1981.

E. Gilbert. *Sulfonation and Related Reactions.* Interscience Publishers, New York, 1965.

S. L. Gojkovic, S. K. Zecevic, and R. F. Savinell. O_2 reduction on an ink-type rotating disk electrode using Pt supported on high-area carbons. *J. Electrochem. Soc.*, 145(11):3713–3720, 1998.

R. Greef, R. Peat, L. M. Peter, D. Pletcher, and J. Robinson. *Instrumental methods in electrochemistry.* Ellis Horwood Limited, 1990.

W. Grove. On voltaic series and the combination of gases by platinum. *Phil. Mag.*, 14(89):127–130, 1839.

W. Grove. On a gaseous voltaic battery. *Phil. Mag.*, 21(140):417–420, 1842.

A. Gruger, A. Regis, T. Schmatko, and P. Colomban. Nanostructure of Nafion membranes at different states of hydration; an IR and Raman study. *Vibrational Spectrosopy*, 26:215, 2001.

C. H. Hamann, A. Hamnett, and W. Vielstich. *Electrochemistry.* Wiley-VCH, 1998.

T. Heldal. Water transport in the polymer electrolyte fuel cell. Master's thesis, Norwegian University of Science and Technology, 1999.

S. Hietala, M. Paronen, S. Holmberg, J. Näsman, J. Juhanoja, M. Karjalainen, R. Serimaa, M. Toivola, T. Lehtinen, K. Parovuori, G. Sundholm, H. Ericson, B. Mattson, L. Torell, and F. Sundholm. Phase separation and crystallinity in proton conducting membranes of styrene grafted and sulfonated poly(vinylidene fluoride). *J. Polym. Sci.: Polym. Chem.*, 37:1741, 1999.

J. Ihonen, F. Jaouen, G. Lindbergh, and G. Sundholm. A novel polymer electrolyte fuel cell for laboratory investigations and in-situ contact resistance measurements. *Electrochimica Acta*, 46:2899–2911, 2001.

Isothermal technology limited. *Reference manual for tempeature products and services.* Isotech, Pine Grove, Southport, England, 1 edition, 1995.

G. J. M. Janssen and M. L. J. Overvelde. Water transport in the proton-exchange-membrane fuel cell: measurements of the effective drag coefficient. *Journal of Power Sources*, 101:117–125, 2001.

G. Jerkiewicz and A. Zolfaghari. Comparison of hydrogen electroadsorption from the electrolyte with hydrogen adsorption from the gas phase. *J. Electrochem. Soc.*, 143(4):1240–1248, 1996.

L. R. Jordan, A. K. Shukla, T. Behrsing, N. R. Avery, B. C. Muddle, and M. Forsyth. Diffusion layer parameters influencing optimal fuel cell performance. *Journal of Power Sources*, vol. 86(1-2):250–254, 2000.

F. R. Kalhammer. Polymer electrolytes and the electric vehicle. *Solid State Ionics*, 135:315–323, 2000.

S. Kjelstrup and D. Bedeaux. Jumps in electric potential and in temperature at the electrode surfaces of the solid oxide fuel cell. *Physica A*, 244(1-4): 213–226, 1997.

S. Kjelstrup, J. Qian, and G. M. Haarberg. The Peltier heating of the aluminium cathode in contact with cryolite-alumina melts. *Electrochimica Acta*, 45:2707–2717, 2000.

S. Kjelstrup, P. Vie, and D. Bedeaux. *Surface Chemistry and electrochemistry of membranes*, chapter Irreversible thermodynamics of membrane surface transport with application to polymer fuel cells. Marcel Dekker, New York, 1999.

N. Kobayashi, H. Fujimura, and K. Ohtsuka. Heat and mass transfer in a molten carbonate fuel cell. (Experimental and analytical investigation of fuel cell temperature distribution). *JSME Internation journal. Series II*, 32 (3):420–427, 1989.

K. Kordesch and G. Simader. *Fuel Cells and Their Applications.* VCH Verlagsgesellschaft, 1996.

K. D. Kreuer, T. Dippel, and J. Maier. Membrane materials for PEM-fuel-cells: A microstructural approach. *Proc. Electrochem. Soc.*, 95-23:241, 1995.

G. S. Kumar, M. Raja, and S. Parthasarathy. High performance electrodes with very low platinum loading for polymer electrolyte fuel cells. *Electrochimica Acta*, 40(3):285–290, 1995.

C. Lagergren, G. Lindbergh, and D. Simonsson. Investigation of porous electrodes by current interruption. application to molten carbonate fuel cell cathodes. *J. Electrochem. Soc.*, 142(3):787–797, 1995.

K. Ledjeff-Hey and A. Heinzel. Critical issues and future prospects for solid polymer fuel cells. *Journal of Power sources*, 61:125–127, 1996.

D. R. Lide, editor. *CRC Handbook of Chemistry and Physics.* CRC Press, Ann Arbor, 71st edition, 1990.

A. Lloyd. Towards the zero emission vehicle: A review of the California fuel cell partnership. In *Delegate Manual*, Seventh Grove Fuel Cell Symposium - Commercialising Fuel Cells: The Issues Outstanding, page O8.1, London, UK, September 2001.

A. C. Lloyd. The California fuel cell partnership: an avenue to clean air. *Journal of Power Sources*, 86(1-2):57–60, 2000.

MathWorks, Inc. The Matlab® homepage. http://www.mathworks.com/, 2002.

K. Matsumoto and K. Kasahara. Long-term commitment of Japanese gas utilities to PAFCs and SOFCs. *Journal of Power Sources*, 71(1-2):51–57, 1998.

J. C. Maxwell. *A Treatise on Electricity and Magnetism*, volume 1. Clarendon Press, Oxford, 2nd edition, 1881. p. 398.

R. Metkemeijer and P. Achard. Comparison of ammonia and methanol applied indirectly in a hydrogen fuel cell. *Int. J. Hydrogen Energy*, 19(6):535–542, 1994.

L. Michalski, K. Eckersdorf, and J. McGhee. *Temperature measurement.* John Wiley & Sons, Chichester, 1991.

P. Millet. Water electrolysis using EME technology: Temperature profile inside a Nafion membrane during electrolysis. *Electrochimica Acta*, 36(2):263–267, 1991.

S. Møller-Holst. Preparation and evaluation of thin film electrodes for solid polymer fuel cells. *J. Electrochem. Soc. Jap. Denki Kagaku*, 64(6):699–705, 1996a.

S. Møller-Holst. *Solid Polymer Fuel Cells, Electrode and Membrane performance studies.* PhD thesis, Norwegian University of Science and Technology, June 1996b.

R. Mosdale and P. Stevens. New electrodes for hydrogen/oxygen solid polymer electrolyte fuel cell. *Solid State Ionics*, 61:251–255, 1993.

J. S. Newman. *Electrochemical Systems.* Prentice Hall international series in the physical and chemical engineering sciences. Prentice-Hall, Englewood Cliffs, New Jersey, 2 edition, 1991.

L. Nummedal. Thermal osmosis in a cation exchange membrane. Master's thesis, Norwegian University of Science and Technology, Trondheim, Norway, 1996.

J. M. Ogden, M. M. Steinbugler, and T. G. Kreutz. A comparison of hydrogen, methanol and gasoline as fuels for fuel cell vehicles: implications for vehicle design and infrastructure development. *Journal of Power Sources*, 79:143–168, 1999.

D. Ostrovskii, M. Paronen, G. Jeschke, P. Tikkanen, E. Rauhala, P. Jacobsson, and F. Sundholm. Effect of irradiation on the sulfonation of poly(vinyl fluoride): Oxidation study of the sulfonated PVF membranes. Submitted, 2001.

D. Ostrovskii, M. Paronen, F. Sundholm, and L. Torell. State of water in sulfonated poly(vinyl fluoride) membranes: an FTIR study. *Solid State Ionics*, 116:301, 1999.

M. Ottøy. *Mass and heat transfer in ion-exchange membranes - applicable to solid polymer fuel cells.* PhD thesis, Norwegian University of Science and Technology, 1996.

F. Panik. Fuel cells for vehicle applications in cars - bringing the future closer. *Journal of Power Sources*, 71:36–38, 1998.

M. Paronen. *Modification of Polymer Films by Ionising Radiation in the Preparation of Proton Conductive Membranes.* PhD thesis, Laboratory of Polymer Chemistry, University of Helsinki, 1999.

M. Paronen, M. Karjalainen, K. Jokela, M. Torkkeli, R. Serimaa, J. Juhanoja, D. Ostrovskii, F. Sundholm, T. Lehtinen, G. Sundholm, and L. Torell. Structure of sulfonated poly(vinyl fluoride). *J. Appl. Polym. Sci*, 73:1273, 1999.

M. Paronen, F. Sundholm, E. Rauhala, T. Lehtinen, and S. Hietala. Effects of irradiation on sulfonation of poly(vinyl fluoride). *J. Mater. Chem.*, 7:2401, 1997.

E. Passalacqua, F. Lufrano, G. Squadrito, A. Patti, and L. Giorgi. Nafion content in the catalyst layer of polymer electrolyte fuel cells: effects on structure and performance. *Electrochimica Acta*, 46:799–805, 2001.

K. Pehr, P. Sauermann, O. Traeger, and M. Bracha. Liquid hydrogen for motor vehicles - the world's first public LH_2 filling station. *Int. J. Hydrogen Energy*, 26:777–782, 2001.

R. H. Perry, D. W. Green, and J. O. Maloney, editors. *Perry's chemical engineers' handbook.* McGraw-Hill, 7th edition, 1997.

K. B. Prater. Polymer electrolyte fuel cells: a review of recent developments. *Journal of Power Sources*, 51:129–144, 1994.

K. B. Prater. Solid polymer fuel cells for transport and stationary applications. *Journal of Power Sources*, 61:105–109, 1996.

M. Prigent. On board hydrogen generation for fuel cell powered electric cars. A review of various available techniques. *Revue de l'institut Français du pétrole*, 52(3):349–360, 1997.

S. K. Ratkje and D. Bedeaux. The overpotential as a surface singularity described by nonequilibrium thermodynamics. *J. Electrochem. Soc.*, 143(3): 779–789, 1996.

S. K. Ratkje, M. Ottøy, R. Halseid, and M. Strømgård. Thermoelectric-power relevant for the solid-polymer-electrolyte fuel-cell. *J. Membr. Sci.*, 107(3): 219–228, 1995.

X. M. Ren, M. S. Wilson, and S. Gottesfeld. High performance direct methanol polymer electrolyte fuel cells. *J. Electrochem. Soc.*, 143(1):L12–L15, 1996.

P. N. Ross Jr. Characteristics of an NH_3 - air fuel cell system for vehicular applications. In *Proceedings of the 16th intersociety energy conversion engineering conference*, pages 726–733, 1981.

J. C. Slattery and R. B. Bird. Calculation of the diffusion coefficient of dilute gases and of the self-diffusion coefficient of dense gases. *A.I.Ch.E. Journal*, 4(2):137–142, June 1958.

A. Solheim. Thermal conductivities in electrolytes with gas bubbles. Note - 2000-02-24, 2000.

T. S. Sørensen, editor. *Surface Chemistry and electrochemistry of membranes.* Marcel Dekker, New York, 1999.

T. E. Springer, M. S. Wilson, and S. Gottesfeld. Modeling and experimental diagnostics in polymer electrolyte fuel cells. *J. Electrochem. Soc.*, 140(12): 3513–3526, 1993.

T. E. Springer, T. A. Zawodzinski, Jr., and S. Gottesfeld. Polymer electrolyte fuel cell model. *J. Electrochem. Soc.*, 138(8):2334–2342, 1991.

T. E. Springer, T. A. Zawodzinski, Jr., M. S. Wilson, and S. Gottesfeld. Characterization of polymer electrolyte fuel cells using AC impedance spectroscopy. *J. Electrochem. Soc.*, 143(2):587–599, 1996.

P. Staiti, Z. Poltarzewski, V. Alderucci, G. Maggio, and N. Giordano. Influence of electrodic properties on water management in a solid polymer electrolyte fuel cell. *Journal of applied electrochemistry*, 22:663–667, 1992.

S. Szymanski, G. Gruver, M. Katz, and H. Kunz. The effect of ammonia on hydrogen-air phosphoric acid fuel cell performance. *J. Electrochem. Soc.*, 127(7):1440–1444, 1980.

C. E. Thomas, B. D. James, F. D. Lomax Jr, and I. F. Kuhn Jr. Fuel options for the fuel cell vehicle: hydrogen, methanol or gasoline? *International Journal of Hydrogen Energy*, 25:551–567, 2000.

S. Thomas and M. Zalbowitz. Fuel cells - green power. Technical Report LA-UR-3231, Los Alamos National Laboratory, Los Alamos, NM, 87545, USA, 1999.

M. Uchida, Y. Aoyama, N. Eda, and A. Ohta. New preparation method for polymer-electrolyte fuel cells. *J. Electrochem. Soc.*, 142(2):463–468, 1995.

F. Uribe, C. Hagedorn, T. Q. T. Rockward, J. Valerio, and T. A. Zawodzinski, Jr. Improving PEM fuel cell cathodes. In *Delegate Manual*, Seventh Grove Fuel Cell Symposium - Commercialising Fuel Cells: The Issues Outstanding, page P2a.15, London, UK, September 2001.

J. J. T. T. Vermeijlen, L. J. J. Janssen, and G. J. Visser. Mechanism of hydrogen oxidation on a platinum-loaded gas diffusion electrode. *J. Appl. Electrochem.*, 27(5):497–506, 1997.

P. J. S. Vie, S. Kjelstrup, and D. Bedeaux. Water and heat balances in the polymer fuel cell modeled by irreversible thermodynamics. In *49th Annual Meeting - Extended Abstracts*, pages I–10–14–05, Kitakyushu, Japan, September 1998. International Society of Electrochemistry.

P. J. S. Vie and S. Møller-Holst. Optimization of electrode compostition in the PEFC using factorial designed experiments. In *Abstracts 1998 Fuel Cell Seminar*, pages 566–569, Palm Springs, California, USA, November 1998.

M. P. R. Waligórski, R. N. Hamm, and R. Katz. The radial distrubution of dose around the path of a heavy ion in liquid water. *Radiat. Meas.*, 6:309, 1986.

L. A. Wall, S. Straus, and R. E. Florin. Pyrolysis of vinyl and vinylidene fluride polymers: Influence of prior 8- irradiation. *J. Polym. Sci., A-1*, 4:349, 1966.

J. T. Wang, S. Wasmus, and R. F. Savinell. Evaluation of ethanol, 1-propanol, and 2-propanol in a direct oxidation polymer-electrolyte fuel cell - a real-time mass spectrometry study. *J. Electrochem. Soc.*, 142(12):4218–4224, 1995.

M. S. Wilson and S. Gottesfeld. Thin-film catalyst layers for polymer electrolyte fuel cell electrodes. *J. Appl. Electrochem.*, 22:1–7, 1992.

M. S. Wilson, J. A. Valerio, and S. Gottesfeld. Low platinum loading electrodes for polymer electrolyte fuel cells fabricated using thermoplastic ionomers. *Electrochimica Acta*, 40(3):355–363, 1995.

J. Wind, R. Späh, W. Kaiser, and G. Böhm. Metallic bipolar plates for PEM fuel cells. *Journal of Power Sources*, 105:256–260, 2002.

T. A. Zawodzinski, Jr., C. Derouin, S. Radzinski, R. J. Sherman, V. T. Smith, T. E. Springer, and S. Gottesfeld. Water uptake by and transport through Nafion 117 membranes. *J. Electrochem. Soc.*, 140(4):1041–1047, 1993.

T. A. Zawodzinski, Jr., M. Neeman, L. Sillerud, and S. Gottesfeld. Determination of water diffusion coefficients in perfluorosulfonate ionomeric membranes. *J. Phys. Chem*, 95:6040–6044, 1991.

A. Zolfaghari, M. Chayer, and G. Jerkiewicz. Energetics of the underpotential deposition of hydrogen on platinum electrodes. 1. Absence of coadsorbed species. *J. Electrochem. Soc.*, 144(9):3034–3041, 1997.

Appendix A

The fuel cell model

The basic equations for the fuel cell model in chapter 5 are presented here. The equations will also apply for the calculation of thermal conductivities in chapter 6. The physical interpretations of the model are also discussed.

A.1 The structure of the fuel cell model

The fuel cell model is a one-dimensional model of the polymer electrolyte fuel cell. All transport in the model is assumed to take place perpendicular to the membrane plane. The model is separated into five parts:

- anode gas diffusion backing
- anode electrode (catalytic layer)
- membrane electrolyte
- cathode electrode (catalytic layer)
- cathode gas diffusion backing

See figure 6.1 for an illustration of the different parts of the fuel cell. A set of unique equations for each part exists, describing the transport of matter, current, heat and energy. The system of equations can be solved by combining each subset of equations.

The model boundaries are the current collector plates connected to the gas diffusion backings. Heat and electricity are transported through the plates.

Flow channels in the current collector plates transport water and reacting gases to and from the system. In figure A.1 the boundary conditions on the anode side are presented. Similar boundary conditions exist for the cathode. The axis in the one-dimensional model is also illustrated.

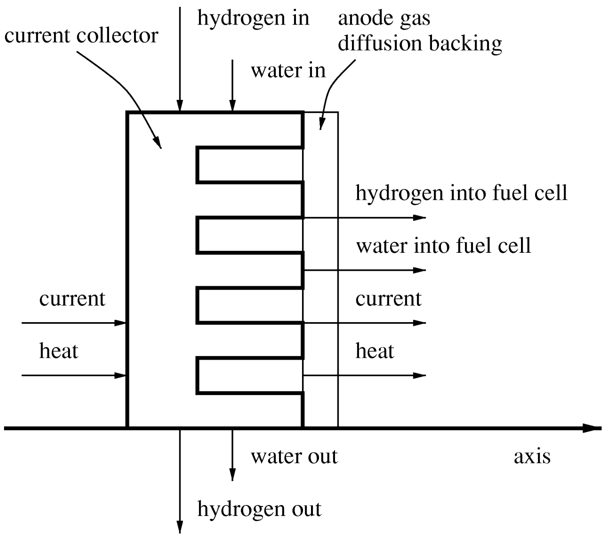

Figure A.1: The boundary conditions for the anode.

A.2 Solving the fuel cell model

The system of equations was solved by iteration. By first assuming isothermal conditions through the fuel cell, the mass and water balances through the fuel cell were solved at different current densities. When the water concentration profile in the electrolyte is calculated, the membrane resistance is known. By introducing information on the kinetics of the fuel cell electrodes and on the overpotentials, the voltage profile through the fuel cell was solved.

All the heat producing terms are now defined and the heat balance for the system were solved. A unique temperature profile was calculated, assuming that the heat transfer coefficients are known.

The calculated temperature profile was introduced into the equations for the mass and water balances. The mass and water balances were then recalculated. This sequence was repeated till convergence of the system.

A.3 Assumptions

The model is a one-dimensional model, with the axis perpendicular to the membrane. Hence we assume that no variation in the system is taking place along the gas flow channels parallel to the membrane. The values calculated are thus average values representing the whole flow field.

In chapter 5 we assume that no heat is removed or added through the current collector plates. The temperatures of the gases entering and leaving the system are the same as the temperatures at the collector plates. We therefore assume that we have an adiabatic system.

The model describes the fuel cell system presented in chapter 2.

A.4 Equations

The water and mass balances in the fuel cell model are mainly presented in this section. The equations for the energy balance and cell voltage are presented in chapters 5 and 6.

A.4.1 Water- and mass balance

Equations for the five separate regions of the fuel cell defined in section A.1, were specified to solve the water and mass balances. In addition to these regions, balances at the boundaries were solved as well. I will first present the equations that define the boundary conditions.

Anode gas compartment

The hydrogen gas enters the anode gas channels containing water. The amount of water is controlled through the temperature in the gas humidifier. The hydrogen gas flow rate can be set to a constant value or adjusted to keep the conversion of the gases constant in the fuel cell. In equation (A.1) the hydrogen flow rate in mol/s ($F^{in}_{\mathrm{H_2}}$) is calculated from the hydrogen flow rate used in the experimental setup, in $\frac{\mathrm{l_N}}{\mathrm{min}}$ ($U^{in}_{\mathrm{H_2}}$) (273.15 K and 1.013·10^5 Pa).

$$F^{in}_{\mathrm{H_2}} = \frac{P_0 \cdot U^{in}_{\mathrm{H_2}} \cdot 10^{-6}}{\mathrm{R} \cdot T_0 \cdot 60} \tag{A.1}$$

The steady-state amount of hydrogen flow to the anode electrode as a function of the current density is:

$$F_{\mathrm{H}_2} = \frac{j \cdot A}{2\mathrm{F}} \tag{A.2}$$

The hydrogen gas flow into the anode compartment can then be calculated from the following equation:

$$U_{\mathrm{H}_2}^{in} = \frac{60 F_{\mathrm{H}_2} \cdot \mathrm{R} T_0}{10^{-6} P_0 \cdot \xi_{\mathrm{H}_2}} \tag{A.3}$$

where

$$\xi_{\mathrm{H}_2} = \frac{F_{\mathrm{H}_2}}{F_{\mathrm{H}_2}^{in}} \tag{A.4}$$

Water enters the anode in equilibrium with the hydrogen gas. The vapour pressure of water is calculated from the following equation [Springer et al., 1991]:

$$P^{sat}(T) = P_0 \cdot 10^{-2.1794+0.02953(T-T_0)-9.1837\cdot 10^{-5}(T-T_0)^2+1.4454\cdot 10^{-7}(T-T_0)^3} \tag{A.5}$$

The amount of water entering the anode can then be calculated from equation (A.6).

$$F_{\mathrm{H}_2\mathrm{O}}^{in,a} = \frac{P_{T_{hum}^a}^{sat}}{P_{tot}^a - P_{T_{hum}^a}^{sat}} F_{\mathrm{H}_2}^{in} \tag{A.6}$$

The amount of water passing from anode to cathode ($F_{\mathrm{H}_2\mathrm{O}}^a$) depends on membrane properties and the state of water in the membrane. This will be further elaborated in the membrane section. The factor α defined in equation (A.7), gives a value for the net water transport through the membrane:

$$\alpha = \frac{F_{\mathrm{H}_2\mathrm{O}}^a}{F_{\mathrm{H}_2}} \tag{A.7}$$

Mass balances for hydrogen and water can then be solved, calculating the flows out of the anode:

$$
\begin{aligned}
F^{out}_{\mathrm{H_2}} &= F^{in}_{\mathrm{H_2}} - F_{\mathrm{H_2}} \qquad \text{(A.8)} \\
F^{out,a}_{\mathrm{H_2O}} &= F^{in,a}_{\mathrm{H_2O}} - F^{a}_{\mathrm{H_2O}} \qquad \text{(A.9)}
\end{aligned}
$$

Hydrogen gas can enter the anode gas compartment supersaturated with water. It is necessary to establish the phase of the water entering and leaving the gas compartment.

When supersaturated gas enters the gas compartment, the amount of water vapour entering the anode gas compartment is found from the temperature at the inlet ($T^{in,a}$):

$$F^{in,a}_{\mathrm{H_2O(g)}} = \frac{P^{sat}_{T^{in,a}}}{P^{a}_{tot} - P^{sat}_{T^{in,a}}} F^{in}_{\mathrm{H_2}} \qquad \text{(A.10)}$$

The liquid water entering the anode compartment is then:

$$F^{in,a}_{\mathrm{H_2O(l)}} = F^{in,a}_{\mathrm{H_2O}} - F^{in,a}_{\mathrm{H_2O(g)}} \qquad \text{(A.11)}$$

and the vapour pressure is:

$$P^{in,a}_{\mathrm{H_2O}} = P^{sat}_{T^{in,a}} \qquad \text{(A.12)}$$

When the water entering the anode gas compartment is undersaturated, all water enters as vapour:

$$F^{in,a}_{\mathrm{H_2O(g)}} = F^{in,a}_{\mathrm{H_2O}} \qquad \text{(A.13)}$$

and the vapour pressure is:

$$P^{in,a}_{\mathrm{H_2O}} = \frac{F^{in,a}_{\mathrm{H_2O}}}{F^{in,a}_{\mathrm{H_2O}} + F^{in}_{\mathrm{H_2}}} P^{a}_{tot} \qquad \text{(A.14)}$$

The mole fraction of water into the anode gas compartment can then be calculated:

$$x^{in,a}_{\mathrm{H_2O}} = \frac{F^{in,a}_{\mathrm{H_2O}}}{F^{in,a}_{\mathrm{H_2O}} + F^{in}_{\mathrm{H_2}}} \qquad \text{(A.15)}$$

Similar equations as equations (A.10) to (A.15) exist for the state of the water leaving the anode compartment at another temperature ($T^{out,a}$). It is then possible to evaluate whether an evaporation or condensation takes place in the anode gas compartment. If more liquid water is leaving the anode than entering the anode, a condensation has happened. The amount of water either evaporating or condensing is defined in equation (A.16). If $F_{\mathrm{H_2O}}^{vap,a}$ is positive, water evaporated in the anode gas compartment, if negative, water condensed.

$$F_{\mathrm{H_2O}}^{vap,a} = F_{\mathrm{H_2O(l)}}^{in,a} - F_{\mathrm{H_2O(l)}}^{out,a} \tag{A.16}$$

Since this model is one-dimensional, average values in the anode compartment are used.

$$P_{\mathrm{H_2O}}^{a} = \frac{P_{\mathrm{H_2O}}^{in,a} + P_{\mathrm{H_2O}}^{out,a}}{2} \tag{A.17}$$

$$x_{\mathrm{H_2O}}^{a} = \frac{x_{\mathrm{H_2O}}^{in,a} + x_{\mathrm{H_2O}}^{out,a}}{2} \tag{A.18}$$

These are the boundary conditions for water in the anode gas compartment.

Cathode gas compartment

The flow of oxygen into the cathode gas compartment ($F_{\mathrm{O_2}}^{in}$) can be calculated from the flow in $\frac{\mathrm{l_N}}{\mathrm{min}}$ ($U_{\mathrm{O_2}}^{in}$) in the same way as the hydrogen flow in equation (A.1). When the conversion of oxygen ($\xi_{\mathrm{O_2}}$) is constant, the gas entering the cathode compartment can be calculated from a similar equation as equation (A.3). The conversion of oxygen is defined in equation (A.19). The negative sign is due to the defined positive axis of the mathematical model.

$$\xi_{\mathrm{O_2}} = \frac{-F_{\mathrm{O_2}}}{F_{\mathrm{O_2}}^{in}} \tag{A.19}$$

The gas entering the cathode gas compartment is saturated with water in the same way as the anode gas. The amount of water entering the cathode ($F_{\mathrm{H_2O}}^{in,c}$) can then be calculated from an equation similar to equation (A.6), but now based on the conditions on the cathode side.

The steady-state flow of oxygen gas entering the cathode electrode is calculated from the following equation:

$$F_{\mathrm{O_2}} = \frac{-j \cdot A}{4\mathrm{F}} \tag{A.20}$$

Water is transported from the anode to the cathode, and water is produced at the cathode. The water transported from the cathode ($F^c_{\mathrm{H_2O}}$) is therefore:

$$F^c_{\mathrm{H_2O}} = F^a_{\mathrm{H_2O}} + \frac{j \cdot A}{2\mathrm{F}} \tag{A.21}$$

Mass balances for oxygen and water is then:

$$\begin{aligned} F^{out}_{\mathrm{O_2}} &= F^{in}_{\mathrm{O_2}} + F_{\mathrm{O_2}} && \text{(A.22)} \\ F^{out,c}_{\mathrm{H_2O}} &= F^{in,c}_{\mathrm{H_2O}} + F^c_{\mathrm{H_2O}} && \text{(A.23)} \end{aligned}$$

Water enters the cathode gas compartment from both gas inlet and gas diffusion backing. Water is leaving through the outlet. Due to possibly different temperatures in these sections, $T^{in,c}$, $T^{out,c}$ and $T^{c,0}$, condensation or evaporation may take place. $T^{c,0}$ is the temperature in the gas diffusion backing close to cathode gas compartment. The state of water at the inlet in the anode compartment was discussed in equations (A.10) to (A.15). Similar equations exists for the inlet and outlet at the cathode. In the backing, water may leave as both vapour and liquid. The flow of saturated water ($F^{sat,c}_{\mathrm{H_2O}}$) is calculated in equation (A.24). This flow is used to evaluate the state of water in the backing. If $F^{sat,c}_{\mathrm{H_2O}}$ is larger than the total flow of water in the backing ($F^c_{\mathrm{H_2O}}$), all water transport is by vapour, see equation (A.25). Liquid water is flowing in the backing if $F^c_{\mathrm{H_2O}}$ is larger than $F^{sat,c}_{\mathrm{H_2O}}$, and $F^c_{\mathrm{H_2O(l)}}$ is defined in equation (A.26).

$$F^{sat,c}_{\mathrm{H_2O}} = \frac{P^{sat}_{T^{c,0}}}{P^c_{tot} - P^{sat}_{T^{c,0}}} \cdot |F_{\mathrm{O_2}}| \tag{A.24}$$

$$\begin{aligned} F^c_{\mathrm{H_2O(g)}} &= F^c_{\mathrm{H_2O}} && \text{(A.25)} \\ F^c_{\mathrm{H_2O(l)}} &= F^c_{\mathrm{H_2O}} - F^c_{\mathrm{H_2O(g)}} && \text{(A.26)} \end{aligned}$$

It is now possible to establish the amount of water condensing or evaporating in the cathode gas compartment. In equation (A.27) the flow of saturated water vapour out of the gas compartment ($F^{sat,out,c}_{\mathrm{H_2O}}$) is specified.

$$F^{sat,out,c}_{\mathrm{H_2O}} = \frac{P^{sat}_{T^{out,c}}}{P^c_{tot} - P^{sat}_{T^{out,c}}} F^{out}_{\mathrm{O_2}} \tag{A.27}$$

If more water vapour enters the gas compartment than the calculated saturation flow out, water will condense. The amount of water evaporating is given in equation (A.28). (Condensed amount is negative.)

$$F_{\mathrm{H_2O}}^{vap,c} = F_{\mathrm{H_2O(g)}}^{c} + F_{\mathrm{H_2O(g)}}^{in,c} - F_{\mathrm{H_2O}}^{sat,out,c} \tag{A.28}$$

There may not be enough water available for evaporation to saturate the leaving gas. The amount of water evaporated is then calculated from equation (A.29).

$$F_{\mathrm{H_2O}}^{vap,c} = F_{\mathrm{H_2O(l)}}^{c} + F_{\mathrm{H_2O(l)}}^{in,c} \tag{A.29}$$

The average conditions in the cathode gas compartment are presented in equations (A.30) to (A.32).

$$P_{\mathrm{H_2O}}^{c} = \frac{P_{\mathrm{H_2O}}^{in,c} + P_{\mathrm{H_2O}}^{out,c}}{2} \tag{A.30}$$

$$x_{\mathrm{H_2O}}^{c} = \frac{x_{\mathrm{H_2O}}^{in,c} + x_{\mathrm{H_2O}}^{out,c}}{2} \tag{A.31}$$

$$x_{\mathrm{H_2O(g)}}^{c} = \frac{F_{\mathrm{H_2O(g)}}^{c}}{F_{\mathrm{H_2O}}^{c} + |F_{\mathrm{O_2}}|} \tag{A.32}$$

Anode gas diffusion backing

The anode gas diffusion backing is a porous hydrophobic carbon matrix [E-TEK Div. of De Nora N.A., Inc.]. Hydrogen and water is transported through the backing to the anode electrode surface. This transport is modelled by diffusion, and all water is assumed to be transported as water vapour.

The gas pressures in the backing at the boundary of the gas compartment are defined in equations (A.33) to (A.35). The position of the number specified in the equations are given in figure A.2.

$$P_{tot}^{1} = P_{tot}^{a} \tag{A.33}$$

$$P_{\mathrm{H_2O}}^{1} = P_{\mathrm{H_2O}}^{a} \tag{A.34}$$

$$P_{\mathrm{H_2}}^{1} = P_{tot}^{1} - P_{\mathrm{H_2O}}^{1} \tag{A.35}$$

Differential equations describing the diffusion in the backing are given below. By solving these equations the local gas pressures at the anode electrode

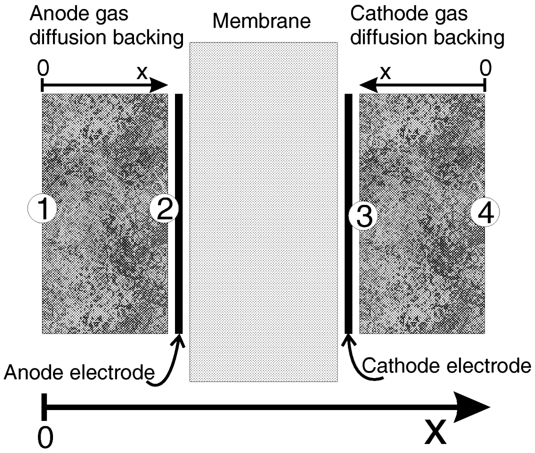

Figure A.2: The positions defining the boundaries of the gas diffusion backings on anode and cathode. The axis for the model is also given.

($P^2_{\mathrm{H_2}}$ and $P^2_{\mathrm{H_2O}}$) can be found. Binary diffusion coefficients are calculated from data given by Slattery and Bird [1958]. See section A.5.1 for details on binary diffusion coefficients.

$$\frac{dP_{\mathrm{H_2}}}{dx} = \frac{-\mathrm{R}T}{D_{\mathrm{H_2H_2O}}} \cdot \left(J_{\mathrm{H_2}} - \frac{P_{\mathrm{H_2}}}{P_{tot}} \left(J_{\mathrm{H_2}} + J^a_{\mathrm{H_2O}} \right) \right) \tag{A.36}$$

$$\frac{dP_{\mathrm{H_2O}}}{dx} = \frac{-\mathrm{R}T}{D_{\mathrm{H_2H_2O}}} \cdot \left(J_{\mathrm{H_2O}} - \frac{P_{\mathrm{H_2O}}}{P_{tot}} \left(J_{\mathrm{H_2}} + J^a_{\mathrm{H_2O}} \right) \right) \tag{A.37}$$

Cathode gas diffusion backing

The transports of oxygen and water through the cathode backing are similar to the hydrogen and water transport through the anode backing. Due to a larger flux of water, water is transported both as gas and liquid. However, the water transport is modelled in a similar way as the water vapour in the anode gas diffusion backing, **assuming that all water is transported as gas**.

The gas pressures in the backing at the cathode gas compartment boundary are presented below:

$$P_{tot}^4 = P_{tot}^c \tag{A.38}$$

$$P_{\mathrm{H_2O}}^4 = P_{\mathrm{H_2O}}^c \tag{A.39}$$

$$P_{\mathrm{O_2}}^4 = P_{tot}^4 - P_{\mathrm{H_2O}}^4 \tag{A.40}$$

The diffusion into the cathode backing was modelled as a ternary diffusion, including diffusion of nitrogen as well as diffusion of oxygen and water. Nitrogen was included because fuel cells are often running on air and hydrogen. The differential equations are presented in equations (A.41) to (A.43). The x-axis in these equations is a local x-axis with direction from gas channel to electrode (figure A.2). The fluxes are thus negative. By solving the system of differential equations we can calculate the local gas pressures at the cathode electrode ($P_{\mathrm{O_2}}^3$, $P_{\mathrm{H_2O}}^3$ and $P_{\mathrm{N_2}}^3$).

$$\begin{aligned}\frac{dP_{\mathrm{O_2}}}{dx} &= \frac{-\mathrm{R}T}{D_{\mathrm{O_2N_2}}} \cdot \left(\frac{P_{\mathrm{N_2}}}{P_{tot}}(-J_{\mathrm{O_2}}) - \frac{P_{\mathrm{O_2}}}{P_{tot}}(-J_{\mathrm{N_2}})\right) \\ &- \frac{-\mathrm{R}T}{D_{\mathrm{O_2H_2O}}} \cdot \left(\frac{P_{\mathrm{H_2O}}}{P_{tot}}(-J_{\mathrm{O_2}}) - \frac{P_{\mathrm{O_2}}}{P_{tot}}(-J_{\mathrm{H_2O}})\right) \qquad \text{(A.41)} \\ \frac{dP_{\mathrm{H_2O}}}{dx} &= \frac{-\mathrm{R}T}{D_{\mathrm{H_2ON_2}}} \cdot \left(\frac{P_{\mathrm{N_2}}}{P_{tot}}(-J_{\mathrm{H_2O}}) - \frac{P_{\mathrm{O_2}}}{P_{tot}}(-J_{\mathrm{N_2}})\right) \\ &- \frac{-\mathrm{R}T}{D_{\mathrm{O_2H_2O}}} \cdot \left(\frac{P_{\mathrm{O_2}}}{P_{tot}}(-J_{\mathrm{H_2O}}) - \frac{P_{\mathrm{H_2O}}}{P_{tot}}(-J_{\mathrm{O_2}})\right) \qquad \text{(A.42)} \\ \frac{dP_{\mathrm{N_2}}}{dx} &= \frac{-\mathrm{R}T}{D_{\mathrm{O_2N_2}}} \cdot \left(\frac{P_{\mathrm{O_2}}}{P_{tot}}(-J_{\mathrm{N_2}}) - \frac{P_{\mathrm{N_2}}}{P_{tot}}(-J_{\mathrm{O_2}})\right) \\ &- \frac{-\mathrm{R}T}{D_{\mathrm{N_2H_2O}}} \cdot \left(\frac{P_{\mathrm{H_2O}}}{P_{tot}}(-J_{\mathrm{N_2}}) - \frac{P_{\mathrm{N_2}}}{P_{tot}}(-J_{\mathrm{H_2O}})\right) \qquad \text{(A.43)}\end{aligned}$$

The solution gives virtual gas pressure gradients through the gas diffusion backing (figure A.5). Virtual in this respect is meant to cover the case of simultaneous one phase and two phase flow. The real oxygen and nitrogen gas pressures can be found from equations (A.44) and (A.45).

$$P^3_{\mathrm{O_2}} = P^{3,virtual}_{\mathrm{O_2}} \left(\frac{1 + x^{3,liq}_{\mathrm{H_2O}}}{1 - x^{3,tot}_{\mathrm{H_2O}}} \right) \quad \text{(A.44)}$$

$$P^3_{\mathrm{N_2}} = P^{3,virtual}_{\mathrm{N_2}} \left(\frac{1 + x^{3,liq}_{\mathrm{H_2O}}}{1 - x^{3,tot}_{\mathrm{H_2O}}} \right) \quad \text{(A.45)}$$

$x^{3,liq}_{\mathrm{H_2O}}$ and $x^{3,tot}_{\mathrm{H_2O}}$ are given below:

$$x^{3,tot}_{\mathrm{H_2O}} = \frac{P^{3,virtual}_{\mathrm{H_2O}}}{P^3_{tot}} \quad \text{(A.46)}$$

$$x^{3,liq}_{\mathrm{H_2O}} = x^{3,tot}_{\mathrm{H_2O}} - x^{3,gas}_{\mathrm{H_2O}} \quad \text{(A.47)}$$

Membrane electrolyte

Water is transported in the membrane electrolyte. Two mechanisms control this transport [Springer et al., 1991] (chapter 5):

- Simultaneous transport of water and protons
- Diffusion of water

Both effects must be considered for the calculation of water transported through the membrane.

The water content in the membrane at the membrane electrode interface is assumed to be in equilibrium with the water vapour pressure in the electrodes. Springer et al. [1991] present in equation (A.48) a correlation between the vapour pressure and the water content in the membrane (λ). λ is the number of water molecules per charge carrying specie ($\mathrm{RSO_3^-}$). At 30 °C the value of λ is 14 in equilibrium with saturated water vapour. In contact with liquid water, higher water concentrations are obtained: $\lambda = 22$ at 100 °C and $\lambda = 16.8$ at 80 °C. The membrane's ability to take up more water in contact with liquid water than in contact with water vapour, the so-called Schröder's paradox is discussed elsewhere [Springer et al., 1991; Ottøy, 1996; Zawodzinski et al., 1993]. λ is assumed independent of temperature [Springer et al., 1991].

$$\lambda = 0.043 + 17.81\frac{P_{\mathrm{H_2O}}}{P^{sat}_{\mathrm{H_2O}}} - 39.85\left(\frac{P_{\mathrm{H_2O}}}{P^{sat}_{\mathrm{H_2O}}}\right)^2 + 36.0\left(\frac{P_{\mathrm{H_2O}}}{P^{sat}_{\mathrm{H_2O}}}\right)^3 \tag{A.48}$$

Springer et al. [1991] report a correlation for the water concentration in the membrane when the gas is supersaturated:

$$\lambda = 14 + 1.4\left(\frac{x^{tot}_{\mathrm{H_2O}}P^{tot}}{P^{sat}} - 1\right), \text{ when } 1 \leqslant \frac{x^{tot}_{\mathrm{H_2O}}}{P^{sat}} \leqslant 3 \tag{A.49}$$

Ottøy [1996] reports values for the water transference coefficient[1], $t_{\mathrm{H_2O}}$, in the Nafion®117 membrane in equilibrium with vapour phase. The water transference coefficient is defined in equation (A.50). $t_{\mathrm{H_2O}}$ is 1.2 for λ in the interval $2 \leqslant \lambda \leqslant 14$. At $\lambda = 22$ (liquid water), $t_{\mathrm{H_2O}}$ is 2.6. Similar results were obtained by Zawodzinski et al. [1993]. Their results varied from 0.9 at $\lambda = 11$ to 2.5 - 2.9 at $\lambda = 22$. A constant $t_{\mathrm{H_2O}}$ of 1.0 was also reported in the interval $1 \leqslant \lambda \leqslant 14$. The constant value measured by Ottøy [1996] is chosen here. The results for $t_{\mathrm{H_2O}}$ will be extrapolated for $\lambda > 14$.

$$t_{\mathrm{H_2O}} = \left(\frac{J_{\mathrm{H_2O}}}{j}\right)_{\nabla\mu_i=0} \tag{A.50}$$

Values for water diffusion coefficients in Nafion®117 membranes are reported by Zawodzinski et al. [1991]. Results for the diffusion coefficient ($D_{\mathrm{H_2O},\lambda}$) when $\lambda > 4$ is presented in equation (A.51) . When $\lambda < 4$ the diffusion coefficient is found by interpolation of data for the intra-diffusion coefficient of water ($D'_{\mathrm{H_2O}}$), and then recalculating to $D_{\mathrm{H_2O},\lambda}$, which is refered to the water content in the membrane (λ). The data are presented in table A.1.

$$D_{\mathrm{H_2O},\lambda} = 10^{-10}e^{\left[2416\left(\frac{1}{303}-\frac{1}{T}\right)\right]}\cdot(2.563-0.33\lambda+0.0264\lambda^2-0.000671\lambda^3) \tag{A.51}$$

In equation (A.52), the $D_{\mathrm{H_2O},\lambda}$ for $\lambda < 4$ is presented. The factor "s" represents a correction for the membrane swelling. Springer et al. [1991] report it to 0.0126. The water activity ($\frac{P_{\mathrm{H_2O}}}{P^{sat}_{\mathrm{H_2O}}}$) can be calculated from equation (A.48).

---

[1] The water transference coefficient is equivalent to the electro-osmotic drag reported by e.g. Zawodzinski et al. [1993].

Table A.1: Data for the intra-diffusion coefficient (D'_{H_2O}) measured by Zawodzinski et al. [1991] as a function of the water content in the membrane (λ). The point at $\lambda = 0$ is introduced to estimate values when $\lambda < 2$.

λ	0	2	3	4
D'_{H_2O}	0	0.6	1.2	2.1

$$\begin{aligned} D_{H_2O,\lambda} &= 10^{-10} e^{\left[2416\left(\frac{1}{303}-\frac{1}{T}\right)\right]} \cdot \frac{1}{(1+s\lambda)^2} \\ &\cdot \frac{\lambda}{\frac{p_{H_2O}}{p^{sat}_{H_2O}}\left[17.81 - 79.70\frac{p_{H_2O}}{p^{sat}_{H_2O}} + 108\left(\frac{p_{H_2O}}{p^{sat}_{H_2O}}\right)^2\right]} D'_{H_2O} \end{aligned} \tag{A.52}$$

The water balance in the membrane can now be solved. The flow of water induced by the flow of protons can be found from equation (A.50):

$$F^{a,drag}_{H_2O} = t_{H_2O}\frac{jA}{\mathrm{F}} \tag{A.53}$$

According to Springer et al. [1991], the flow of water due to diffusion is:

$$F^{a,diff}_{H_2O} = \frac{-\rho_{dry}A}{M_m} D_{H_2O,\lambda}\frac{d\lambda}{dx} \tag{A.54}$$

where ρ_{dry} is the density of the dry membrane and M_m is the equivalent weight of the Nafion®membrane.

The net flow of water through the membrane is then:

$$F^{a}_{H_2O} = t_{H_2O}\frac{jA}{\mathrm{F}} - \frac{\rho_{dry}A}{M_m} D_{H_2O,\lambda}\frac{d\lambda}{dx} \tag{A.55}$$

The following differential equation is obtained by introducing equation (A.7) into equation (A.55) above:

$$\alpha - 2t_{H_2O} = -\frac{2\rho_{dry}\mathrm{F}}{M_m j} \cdot D_{H_2O,\lambda}\frac{d\lambda}{dx} \tag{A.56}$$

By separating the differential equation and integrating over the membrane from anode to cathode, we obtain an expression for the net water transport factor (α):

$$\alpha = 2t_{\mathrm{H_2O}} - \frac{2\rho_{dry}\mathrm{F}}{M_m j d_{memdry}} \int_{\lambda^a}^{\lambda^c} D_{\mathrm{H_2O},\lambda} d\lambda \tag{A.57}$$

d_{memdry} is the thickness of the dry Nafion®membrane.

The water balance in the membrane can now be solved by applying the function "fminsearch" in Matlab®. A starting value for α is specified and the water contents on the anode ($P^{2,g}_{\mathrm{H_2O}}$) and cathode ($P^{3,g}_{\mathrm{H_2O}}$) sides of the membrane are calculated solving equations (A.36), (A.37), (A.41) and (A.42). Through equation (A.57), the water content on the cathode ($P^{3,m}_{\mathrm{H_2O}}$) will be calculated and α will be varied until $P^{3,g}_{\mathrm{H_2O}}$ equals $P^{3,m}_{\mathrm{H_2O}}$.

A.4.2 Membrane resistance

Springer et al. [1991] present the following equation (A.58) for the membrane conductivity ($\sigma(T,\lambda)$) as a function of temperature and membrane water content. This equation is valid when $\lambda > 1$. If $\lambda \leqslant 1$, the value for $\sigma(T,1)$ is used. This is a crude approximation, and the only purpose is to avoid the calculation to break down during iteration.

$$\sigma(T,\lambda) = e^{\left[1268\left(\frac{1}{303} - \frac{1}{T-0.15}\right)\right]}(0.005139\lambda - 0.00326)1 \cdot 10^2 \tag{A.58}$$

The membrane resistance is then calculated by integrating over the membrane water profile from anode to cathode, see equation (A.59). The temperature is assumed constant in the membrane when solving this equation.

$$R_{mem} = \int_0^{d_{memdry}} \frac{dz}{\sigma(T,\lambda)} \tag{A.59}$$

A.5 Auxiliary equations

A.5.1 Binary diffusion coeffcients

Slattery and Bird [1958] present an equation for estimation of binary diffusion coefficients for a mixture of A and B:

$$D_{\mathrm{AB}} = \left[\frac{a}{P_{tot}} \cdot \left(\frac{T}{\sqrt{T_{\mathrm{A}}^{cr} T_{\mathrm{B}}^{cr}}}\right)^{b} \cdot (P_{\mathrm{A}}^{cr} P_{\mathrm{B}}^{cr})^{\frac{1}{3}} \cdot (T_{\mathrm{A}}^{cr} T_{\mathrm{B}}^{cr})^{\frac{5}{12}} \cdot \sqrt{\frac{1}{\mathrm{M_A}} + \frac{1}{\mathrm{M_B}}}\right] \cdot \frac{\epsilon}{\tau} \cdot 1 \cdot 10^{-4} \qquad \text{(A.60)}$$

Critical temperatures, pressures and molecular weight for hydrogen, oxygen and water are given in table A.2 [Perry et al., 1997; Lide, 1990]. Values for a and b depend on the amount of water. If water is one of the diffusing substances $a = 0.000364$ and $b = 2.334$, if not $a = 0.0002745$ and $b = 1.832$. The porosity ($\epsilon = 0.4$) and tortuosity ($\tau = 7$) for the gas diffusion backing were reported by Springer et al. [1996].

Table A.2: Critical temperatures and pressures for hydrogen, oxygen, nitrogen and water [Perry et al., 1997]. The molecular weight of each substance are also specified.

Compound	P^{cr} (atm)	T^{cr} (K)	M (g/mol)
H_2	13.03	33.19	2.016
O_2	49.54	154.58	31.999
H_2O	216.5	647.13	18.015
N_2	23.29	126.2	28.014

A.6 Substantiation of the model

The equations presented in section A.4 are substantiated in this section. The substantiation was done by measurements and calculations. The gas flows, temperatures and gas pressures are the same as the measuring conditions presented in chapter 6. The gas pressure on both cathode and anode is 4.5 bar, the minimum gas flow rate is 30 $\mathrm{ml_N}$/min, the gas conversion is 50 % and the humidification temperature is 80 °C. The temperatures in the fuel cell are also taken from chapter 6.

A.6.1 Experimental check of flow rates

Measured and calculated flowrates are presented in table A.3. We observe good agreement between the measured and calculated flow-rates. This agreement indicates that the equations for calculating the molar flows in the fuel cell model are correct.

Table A.3: A comparison between controlled and calculated flow rates in the fuel cell. The minimum flow rate was 30 ml_N/min and the gas conversion was set to 50%.

Controlled current density (A/cm^2)	Controlled hydrogen flow (ml_N/min)	Calculated current density (A/cm^2)	Calculated hydrogen flow (ml_N/min)
0.20	30	0.20	30
0.26	30	0.30	30
0.33	30	0.40	31
0.43	32		
0.53	40	0.50	39
0.61	46	0.60	46
0.70	52	0.70	54
0.78	59	0.80	62
0.85	63	0.90	69

The flow rates are presented as a function of current density in figure A.3. In the upper figure we see that the hydrogen flow into the anode gas channel ($F_{\mathrm{H}_2}^{in}$) is constant until it starts to increase steadily at 0.4 A/cm^2. The hydrogen flow into the anode electrode (F_{H_2}) is increasing and the hydrogen flow out of the gas channel ($F_{\mathrm{H}_2}^{out}$) is decreasing. A similar pattern is observed for water entering and leaving the anode gas channel. The amount of water entering the anode gas channel is much lower than the amount of hydrogen due to the large gas pressure in the system. At higher current densities (0.4 A/cm^2) we observe that all water entering the fuel cell is being transported through the membrane. This observation will be further discussed in section A.6.3.

Figure A.3 gives similar behaviours for the gas flows in the cathode gas channel. Hydrogen is consumed at twice the rate of oxygen. The oxygen gas flow into the gas channel is therefore constant upto 0.8 A/cm^2. Water is produced at the cathode and we see at 0.8 A/cm^2 that approximately 20 μmol/s

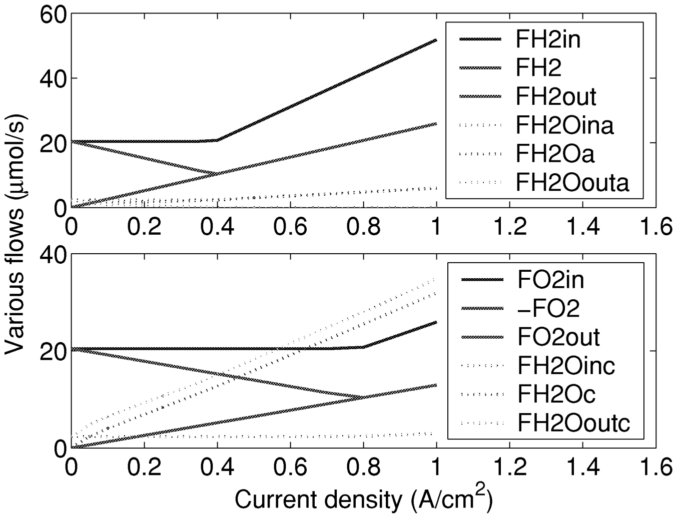

Figure A.3: The variation of gas flow rates as a function of the current density. The upper figure contains data for the anode gas channel, and the lower figure contains data for the cathode gas channel.

hydrogen is consumed, 10 μmol/s oxygen is consumed and 22 μmol/s water is leaving the cathode gas diffusion backing. The extra 2 μmol/s is the water transported through the membrane.

A.6.2 Gas diffusion electrodes

The gas diffusion in the backings was modelled from the equations presented in section A.4. The results are presented in figures A.4 and A.5. In the anode gas diffusion backing we observe a fairly constant partial pressure profile throughout the backing. This observation indicates that there are no diffusion limitations in the anode backing.

The partial pressure varies slightly as a function of the current density, see figure A.6. At about 0.4-0.6 A/cm^2 there is a maximum in the partial pressure of hydrogen. This may be correlated to the fact that all water entering the anode gas compartment here enters the gas diffusion backing and membrane.

A somewhat different profile is observed for the gas diffusion backing on the cathode (figure A.5). The profile is constant at low current densities, but at higher current densities the partial pressures of oxygen and water is varying

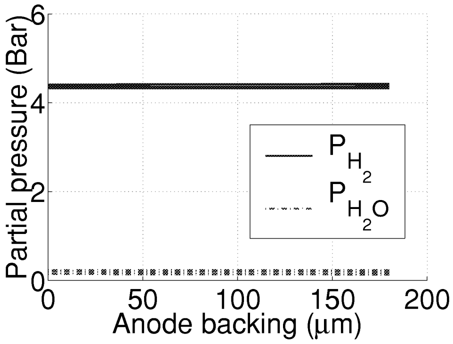

Figure A.4: The partial pressures of hydrogen and water in the anode gas diffusion backing at different current densities (0 - 1 A/cm^2); highest $P_{\mathrm{H_2O}}$ at 0 A/cm^2.

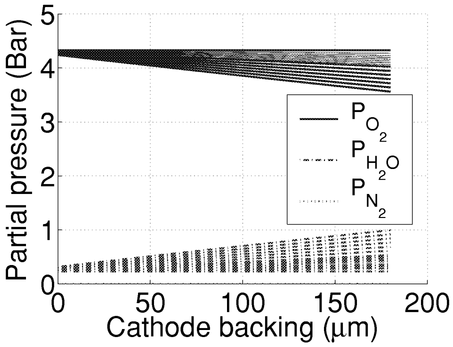

Figure A.5: The virtual partial pressures of oxygen and water in the anode gas diffusion backing at different current densities (0 - 1 A/cm^2); lowest $P_{\mathrm{H_2O}}$ at 0 A/cm^2. The pressures presented in this figures are the virtual gas pressures, see equation (A.44) for a definition.

along the gas diffusion backing. The profile illustrates the water transport mechanism in the cathode gas diffusion backing. The true gas pressures in figure A.6 are constant throughout the cathode backing.

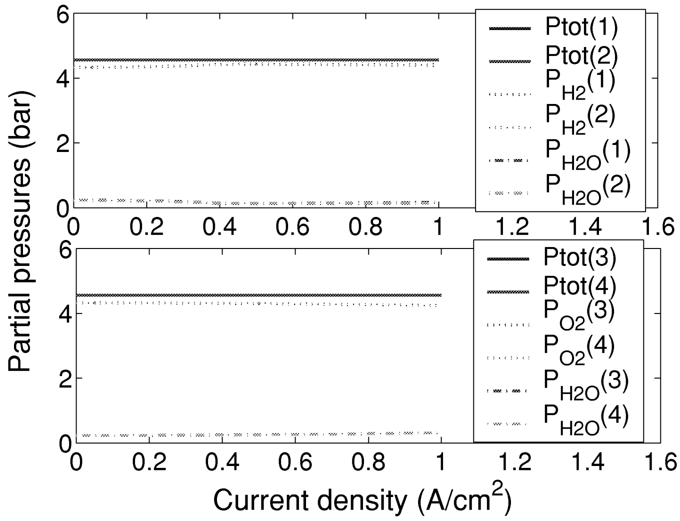

Figure A.6: The variation of gas pressures with respect to the current density. The positions specified are defined in figure A.2.

A.6.3 Water balance

The water balance was solved by iteration. A discussion of the obtained water concentration profile in the membrane is given first.

Membrane water profile

The water concentration profile in the membrane is presented in figure A.7. At low current densities, the water content is constant at $\lambda = 14$ throughout the membrane. This corresponds to the membrane being in equilibrium with saturated water vapour. When the current densities increase, the water content decreases on the anode and increases on the cathode. This is reasonable, since water is produced on the cathode and transported from the anode to the cathode. Büchi and Scherer [2001] present a similar membrane water profile. The main difference of this profile is the curvature close to the anode, and the fact that the water content is maximum $\lambda = 14$ in the results given by Büchi and Scherer [2001]. The difference in curvature is probably caused by different models for the water diffusion coefficient in the membrane. The further elucidation of the profile need the connection to the net water transport factor discussed below.

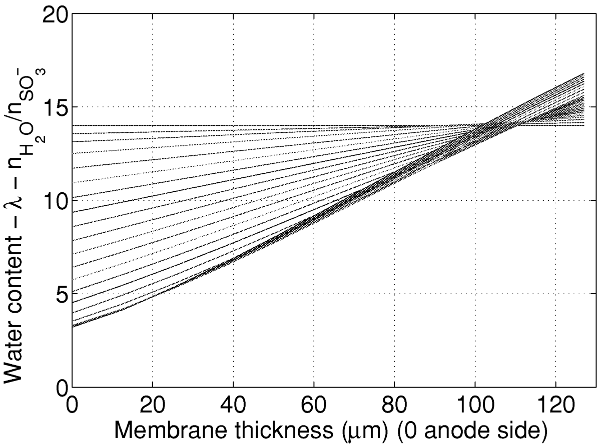

Figure A.7: The membrane water content (λ) at different current densities (0 - 1 A/cm^2). The profile is “flat” at 0 A/cm^2.

Net flux of water in membrane

The net water transport in the membrane is a balance between the simultaneous drag of protons and water (t_{H_2O}) and diffusion of water due to a concentration gradient. In equation (A.57) this balance is solved giving a solution for the net water transport factor α defined in equation (A.7). At no back diffusion of water, α is 2.4. Values for α at different current densities are presented in figure A.8. We observe that α is below 2.4 for all current densities, indicating that water is also transported from cathode to anode.

The behaviour of α upto 0.4 A/cm^2 is reasonable with an increasing back diffusion of water due to an increasing water concentration gradient in the membrane (figure A.9). Above 0.4 A/cm^2 α is increasing, which is not likely. Simultaneously, we observe that λ^a stabilises at about $\lambda = 3.2$, which is the limiting value (equation (A.17)) at the inlet conditions. The system may behave non-physical above 0.4 A/cm^2, lacking robustness. A two-dimensional model would probably solve this problem better.

A few other groups have also reported results for the net water transport in humidified systems [Janssen and Overvelde, 2001; Choi et al., 2000]. Unfortunately the results reported by Choi et al. [2000] were erroneous. Janssen and

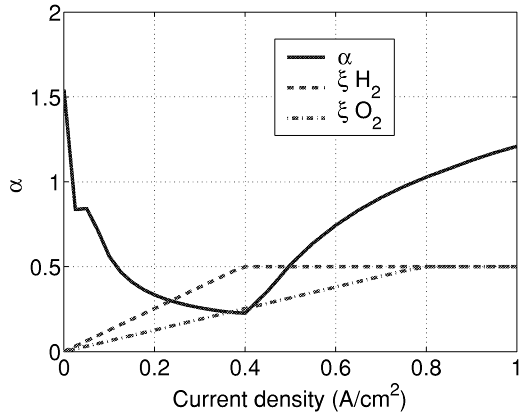

Figure A.8: The net membrane water transport factor (α) as a function of current density.

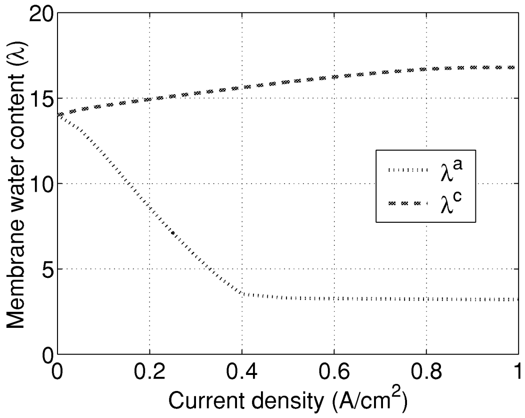

Figure A.9: The membrane water content (λ) at anode and cathode side as a function of current density.

Overvelde [2001] report $\alpha \approx 0.4$ with a Nafion® 105 membrane, and similar conditions[2] at current densities of 0.4 and 0.6 A/cm^2. This is in the same range or lower than the values reported in figure A.8. The Nafion 105 membrane has a lower equivalent weight which enhances the back-diffusion. Staiti

---

[2] ETEK Elat® electrodes, humidified gases (80 °C) and 67 % gas conversion

et al. [1992] report values for water transport ($F_{H_2O}/(j/F)$)[3] in PEM fuel cells[4] at 50 °C, a humidified anode gas and dry cathode gas, varying the amount of wet-proofing in the backing. They report values for α varying from 0.2 to 1.2, corresponding to a Teflon® loading of respectively 60 wt% and 0 wt%. With electrodes similar to ETEK Elat® electrodes modelled here, α was reported to 0.1. Results from other groups is referenced by Staiti et al. [1992][5]: Springer et al. report an α of 1.34 at 80 °C, Nafion®117 membrane and 0.5 A/cm^2.

The results reported in figure A.8 are therefore reasonable compared to available literature. But, the behaviour does not seem likely above 0.4 A/cm^2, and further studies of the water transport in the PEM fuel cell are advised.

---

[3] $\alpha = (F_{H_2O}/F_{H_2})$

[4] Nafion®117 membrane, electrodes: 0.5 mg Pt/cm^2 and 1.1 mg/cm^2 Nafion, backing: Toray TGP 90

[5] Unfortunately the results are not published in primary literature.

Appendix B

Fit of polarisation curve data

B.1 Introduction

In this appendix the measured fuel cell polarisation curve is modelled. The Butler-Volmer equation is applied to describe the electrode kinetics. The ohmic resistance and diffusion limitations at higher current densities are also included. This method will be used to calculate estimates for the overpotentials applied in chapter 6, from the measured polarisation curve.

B.2 Theory

The measured fuel cell voltage differs from the reversible potential for the fuel cell reaction (equation (B.3)). Heat is produced in the system due to ohmic resistance in the various parts of the fuel cell, and heat is generated due to irreversibilities in the electrode processes. Diffusion limitations in the electrodes can also cause a reduced fuel cell voltage. In section B.2.2 these effects are discussed. Before discussing these effects further, the expression for the reversible cell voltage will be discussed in section B.2.1.

The fuel cell reactions are presented below. In equation (B.1) the net anode reaction is given. The net cathode reaction is given in equation (B.2). The total fuel cell reaction is given in equation (B.3).

$$\mathrm{H}_2(g) \rightarrow 2\mathrm{H}^+ + 2e^- \tag{B.1}$$

$$\frac{1}{2}\mathrm{O_2}(g) + 2\mathrm{H}^+ + 2e^- \rightarrow \mathrm{H_2O}(l) \tag{B.2}$$

$$\mathrm{H_2}(g) + \frac{1}{2}\mathrm{O_2}(g) \rightarrow \mathrm{H_2O}(l) \quad E^0 = 1.23\mathrm{V}\ (298\ \mathrm{K},\, 1\ \mathrm{atm}) \tag{B.3}$$

B.2.1 Reversible cell voltage

The cell voltage is linked to the Gibbs energy through equation (B.4). The Gibbs energy for the fuel cell reaction is defined in equation (B.5).

$$\Delta\mathrm{G} = -n\mathrm{F}E \tag{B.4}$$

$$\Delta\mathrm{G} = \Delta\mathrm{G}^0 + \mathrm{R}T \ln \frac{a_{\mathrm{H_2O}}}{a_{\mathrm{H_2}} a_{\mathrm{O_2}}^{0.5}} \tag{B.5}$$

The activity of a gaseous specie is here defined as $a_x = \frac{P_x}{P_0}$. P_0 is 1 atm. The activity of pure water is assumed 1. n in equation (B.4) is here 2 due to the number of electrons transferred.

The variation of ΔG with temperature and pressure can be found from the Maxwell relations [Atkins, 1999]:

$$\left(\frac{\partial \Delta\mathrm{G}}{\partial T}\right)_P = -\Delta\mathrm{S} \tag{B.6}$$

$$\left(\frac{\partial \Delta\mathrm{G}}{\partial P}\right)_T = \Delta V \tag{B.7}$$

By integrating these expressions with respect to temperature and pressure, correction terms may be found. Equation (B.6) can be further elaborated by introducing the temperature dependence of ΔS[Atkins, 1999].

$$\begin{aligned} \Delta\left(\Delta\mathrm{G}(T)\right)_P &= -\Delta\mathrm{S}^0(T - T_0) + C_p^r \ln |T_0(T - T_0)| \\ &\quad -C_p^r T \ln T + C_p^r T_0 \ln T_0 + C_p^r (T - T_0) \end{aligned} \tag{B.8}$$

C_p^r is the heat capacity for the reacting species:

$$C_p^r = C_p(\mathrm{H_2O}) - 0.5 C_p(\mathrm{O_2}) - C_p(\mathrm{H_2}) \tag{B.9}$$

ΔV in equation (B.7) can be correlated to the change in molecules in gas phase during the fuel cell reaction, Δn, through the equation of state for an ideal gas. When liquid water is produced, $\Delta n = -\frac{3}{2}$, and when water in gas phase is produced, $\Delta n = -\frac{1}{2}$.

$$\Delta\left(\Delta \mathrm{G}(P)\right)_T = \Delta n \mathrm{R} T \ln \frac{P}{P_0} \tag{B.10}$$

From the equations above the total expression for the reversible cell voltage as a function of temperature, pressure and composition can be found:

$$\begin{aligned} E^{rev}(T,P) &= E^0 + \frac{1}{2\mathrm{F}}\Bigg[\Delta \mathrm{S}^0(T-T_0) - C_p^r \ln|T_0(T-T_0)| \\ &\quad + C_p^r T \ln T - Cp^r T_0 \ln T_0 - C_p^r (T - T_0)\Bigg] \\ &\quad - \frac{\Delta n \mathrm{R} T}{2\mathrm{F}} \ln \frac{P}{P^0} - \frac{\mathrm{R}T}{2\mathrm{F}} \ln \frac{a_{\mathrm{H_2O}}}{\frac{P_{\mathrm{H_2}}}{P^0}\left(\frac{P_{O_2}}{P^0}\right)^{0.5}} \end{aligned} \tag{B.11}$$

B.2.2 Irreversible losses

E^{rev} is the energy available for production of electricity. Due to irreversibilities, heat is dissipated in the system. These irreversibilities are often denoted overvoltages. There exist different types of overvoltage [Kordesch and Simader, 1996; Greef et al., 1990; Hamann et al., 1998], below are the most relevant presented:

Activation overvoltage is caused by the speed of the charge transfer reactions on the electrodes. Activation overvoltages are normally denoted the overvoltage on anode and cathode; η^a and η^c. The overvoltage is normally described by the Butler-Volmer equation, which simplifies into the Tafel-equation at high η.

Concentration overvoltage is occurring when the diffusion process is limiting the reaction kinetics. The concentration overvoltage can be represented by the following term; $E_d(1 - \frac{j}{j_L})$. j_L is the limiting current density and E_d is a correcting voltage.

Resistance overvoltage is the voltage drop caused by the ohmic resistance in the electrochemical system; $r \cdot j$. The resistance overvoltage can be separated into terms for the different sections of the fuel cell.

All these overvoltages will contribute in the reduction of the cell voltage from E^{rev}. See equation (B.12) for the contribution from each section of the fuel cell to the cell voltage.

$$E = E^{rev} - r^a j - E^a_d(1 - \frac{j}{j^a_L}) - \eta^a - r^m j + \eta^c - r^c j - E^c_d(1 - \frac{j}{j^c_L}) \quad \text{(B.12)}$$

By assuming that diffusion limitations in one electrode is larger than in the other, we define the fuel cell to have one diffusion current. A simplified expression is then:

$$E = E^{rev} - \eta^a + \eta^c - rj - E_d(1 - \frac{j}{j_L}) \quad \text{(B.13)}$$

The activation overvoltage enters the Butler-Volmer equation, and can be estimated from the measured current density and the exchange current density (equations (B.14) and (B.15)). The temperature is also a factor in the equation, and non-isothermal conditions can therefore be included.

$$\begin{aligned} j &= j^0_{\mathrm{H}_2}\left[e^{\frac{\alpha n \mathrm{F}\,\eta^a}{\mathrm{R}T}} - e^{-\frac{\alpha n \mathrm{F}\,\eta^a}{\mathrm{R}T}}\right] & \text{(B.14)} \\ j &= j^0_{\mathrm{O}_2}\left[e^{\frac{\alpha n \mathrm{F}\,\eta^c}{\mathrm{R}T}} - e^{-\frac{\alpha n \mathrm{F}\,\eta^c}{\mathrm{R}T}}\right] & \text{(B.15)} \end{aligned}$$

j^0 is the exchange current density, α is the symmetry factor and η is the overvoltage. In this empirical data fit model, α and n are assumed respectively 0.5 and 2. j^0 has the unit A/cm^2, which is referring to the active fuel cell area and not to the area of the catalyst surface.

B.2.3 Model-fit

The aim of this appendix is to develop an empirical mathematical model for fitting measured polarisation curves. Due to the non-linear nature of equations (B.14) and (B.15), a linear regression algorithm is not suited. Instead a search for the coefficients giving a least squares solution can be obtained with various multi-dimensional search routines. The unconstrained routine, “fminsearch” was used in Matlab®. This routine uses the Nelder-Mead simplex (direct search) method. The constrained routine, “fmincon”, was also used. This routine is especially suited when diffusion overvoltage is included, due to the constraints on the limiting current density. With this method it is possible to obtain a good fit at both high and low current densities. Due to the direct use of the Butler-Volmer equation, this model does not run into numerical instabilities at very low current densities. The Tafel-equation is not applicable for the anode overvoltage due to the low overvoltage for the hydrogen reduction reaction.

B.3 Experimental

An experiment was performed on the fuel cell test-facility presented in chapter 2, measuring both fuel cell temperatures and ohmic resistance in the fuel cell by current interrupt, in addition to obtaining the polarisation curves.

The electrodes were commercial E-TEK ELAT® electrodes impregnated with 0.6 mg/cm^2 Nafion ionomer. The loading of the electrodes were approximately 0.5 mg/cm^2 Platinum. The membrane was a Nafion 112 membrane. Gas pressure was 2 bara. Hydrogen and oxygen gas were humidified to 80 ^{o}C before entering the fuel cell at a rate of 80% conversion. The minimum flow rate was 20 ml$_n$/min. The temperature at the outlet of the cathode gas channel was measured. During the testing, the fuel cell temperature was normally in the range of 50 to 55 ^{o}C.

B.4 Results and discussion

B.4.1 Reversible cell voltage

The reversible cell voltage varies as a function of temperature, gas pressure and gas composition. From equation (B.8) we see that $\Delta(\Delta \mathrm{G}(T))$ is positive when increasing the temperature for negative $\Delta\mathrm{S}$. This means that the E^{rev} is reduced. Likewise is $\Delta(\Delta \mathrm{G}(P))$ negative, when increasing the gas pressure above P_0, see equation (B.10). Hence is E^{rev} increasing with increasing gas pressure.

The gas composition of the reacting gases affects E^{rev} considerably. Low activities of hydrogen and oxygen may exist when the gases are dissolved in

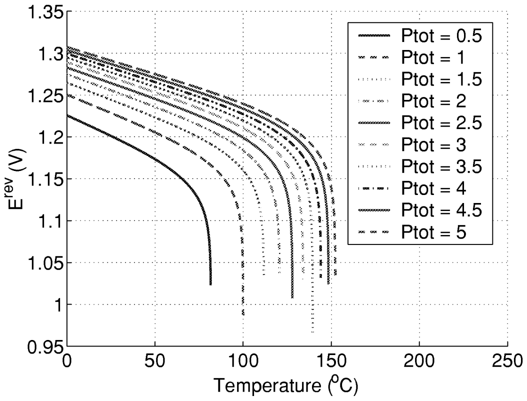

Figure B.1: E^{rev} as function of temperature and gas pressure. The gas pressures are given in bara. The partial pressure of water is the saturation pressure of water.

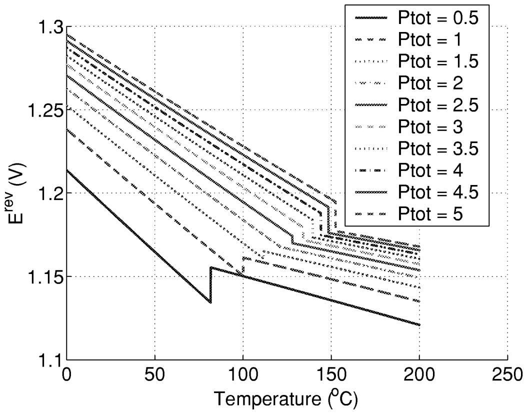

Figure B.2: E^{rev} as function of temperature and gas pressure. The gas pressures are given in bara. The partial pressure of water is $0.5P_{tot}$.

liquid water or Nafion ionomer. This occurs at higher current densities when gas pressures are reduced due to diffusion limitations. E^{rev} is plotted as a function of temperature at various gas pressures in figure B.1 and B.2.

We observe large negative slopes in figure B.1 close to the boiling point of water for the various pressures. This is caused by the rapidly decreasing activities of hydrogen and oxygen. We also observe discontinuities in E^{rev} at the boiling points in figure B.2. This is caused by the phase transition of water.

B.4.2 Fuel cell testing

One single scan was performed, measuring the fuel cell resistance manually. The voltage, current density and temperature data are presented in figure B.3. We observe some peaks in the cell voltages. These were caused by the measurements of ohmic resistance, by opening the circuit for a short time, during the voltage measurement. The current interruption technique was further discussed by Møller-Holst [1996b] and Lagergren et al. [1995]. The voltage peaks were removed from the data set and the measured resistance data was fitted to a linear regression model. The model is presented in figure B.4. We observe a small decrease in fuel cell resistance when increasing the current density. This decrease may be caused by the increased fuel cell temperature (figure B.5), enhancing the membrane's ionic conductivity. The measured temperature is presented as a function of current density in figure B.5. We observe a small hysteresis effect. The effect is explained by the fact that the measurements were taken too fast to let the system come to a complete stationary state.

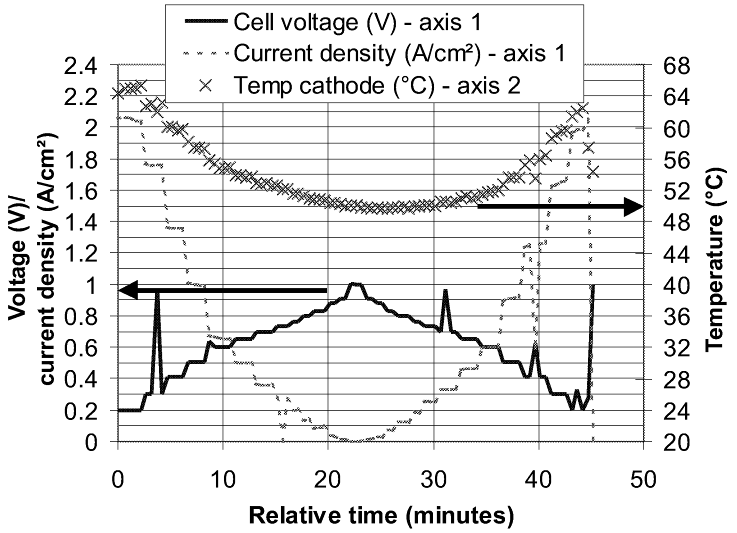

Figure B.3: The voltage current density data plotted as a function of relative measurement time. The measured cathode temperature is also included.

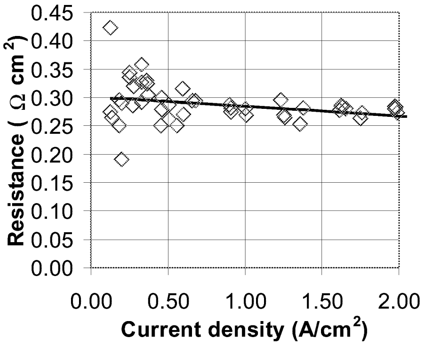

Figure B.4: Measured fuel cell resistance as a function of current density. The data was fitted to a linear regression model, corresponding to the following equation: $R = 0.301 - 0.0169j$ The standard deviation of the fit was: $\sigma = 0.03\ \Omega\text{cm}^2$.

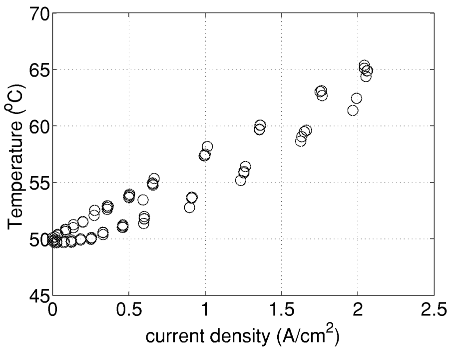

Figure B.5: The measured temperature as a function of current density.

B.4.3 Irreversible losses

Polarisation curve data were fitted to the model presented in equation (B.13). In addition to the measured voltage and current density data (figure B.3), the measured fuel cell temperatures and ohmic resistances were also used as input to the model. Several options exist to fit the data with a varying number of free variables. Due to the strong linear relationship between voltage and current density at higher current densities (figure B.6), diffusion limitations were not necessary. The possible free variables chosen here are $j^0_{\mathrm{H}_2}$, $j^0_{\mathrm{O}_2}$ and r.

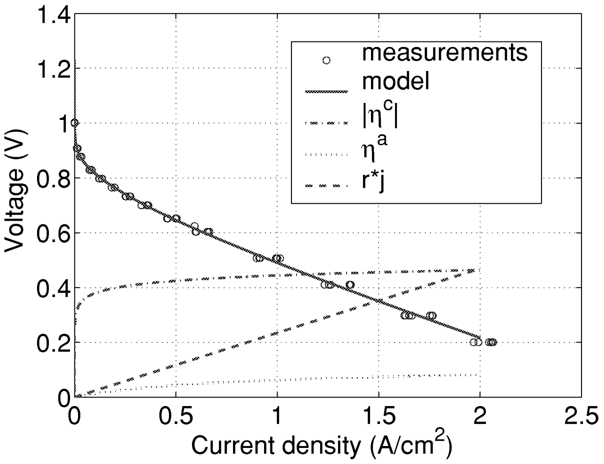

Figure B.6: Polarisation curve fit for fit A (table B.1. Calculated variables: $j^0_{\mathrm{O}_2} = 1.5 \cdot 10^{-7}$ A/cm^2, $j^0_{\mathrm{H}_2} = 0.11$ A/cm^2 and r = 0.24 Ωcm^2. Temperature was assumed constant at 55 °C. The standard deviation of the fit was 0.011.

Results from the various fits are presented in table B.1. Most of the fits obtain almost the same standard deviation, only fit E and G give a distinct visible systematic deviation from the measured data. These fits have also significant higher standard deviations.

We observe that several different fits give almost the same standard deviation. This indicates that the system is over-determined. The value of $j^0_{\mathrm{H}_2}$ is especially sensitive, and varies in the range $[0.1, 700]$ A/cm^2. In contrast, $j^0_{\mathrm{O}_2}$ is much more robust and is varying in a much more narrow region; $[5 \cdot 10^{-8}, 1.3 \cdot 10^{-7}]$ A/cm^2. The fitted values of r are also in a narrow region; $[0.21, 0.26]$ Ωcm^2.

A typical fit is presented in figure B.6. We observe a very good fit to the measured polarisation curve data. It should be noted that the obtained values for the exchange current densities refer to the active fuel cell area and not the catalyst surface area. An equivalent fit can be obtained by interchanging the calculated values for $j^0_{\mathrm{H}_2}$ and $j^0_{\mathrm{O}_2}$. This shows the empirical basis of this model. The obtained values for η^a in figure B.6 are nonetheless in the same range as values previously measured in our laboratory (not published). The fit based on the measured values for temperature and ohmic resistance (fit D) have a slightly higher standard deviation than the best fit (fit A). This can be

Table B.1: Solutions to the fit of polarisation curve data to empirical models. Various combinations (A to H) of constant and free variables were fitted to the model (equation (B.13).

Fit	Constant values			Fitted values			Standard deviation
	r [Ωcm^2]	T [^{o}C]	$j^0_{H_2}$ [A/cm^2]	$j^0_{O_2}$ [A/cm^2]	$j^0_{H_2}$ [A/cm^2]	r [Ωcm^2]	[V]
A	-	55	-	$1.51 \cdot 10^{-7}$	0.111	0.235	0.011
B	-	$T(j)$	-	$1.12 \cdot 10^{-7}$	0.0857	0.216	0.013
C	-	$T(j)$	0	$5.5 \cdot 10^{-8}$	-	0.26	0.016
D	$r(j)$	$T(j)$	-	$9.8 \cdot 10^{-8}$	700	-	0.016
E	0.29	$T(j)$	-	$1.3 \cdot 10^{-7}$	320	-	0.026
F	-	$T(j)$	0.1	$1.03 \cdot 10^{-7}$	-	0.22	0.013
G	$r(j)$	$T(j)$	0.1	$5.2 \cdot 10^{-7}$	-	-	0.035
H	$r(j)$	$T(j)$	10000	$9.8 \cdot 10^{-8}$	-	-	0.015

caused by inaccuracies in the measured resistances, or factors not included in the empirical fit.

It should be stressed that this model basically will give a good empirical fit of polarisation curve data. The physical interpretation of the data is weak, especially since no measurements of overvoltage is included. Due to the linearity of η^a as function of current density, when η^a is small, it is difficult to separate ohmic resistance and η^a.

B.5 Conclusion

A measured polarisation curve was fitted to an empirical mathematical model. The electrode kinetics was described by the Butler-Volmer equation. A good fit to the measured data was obtained for the complete current density range. The obtained fit is mostly empirical, but it can give indications of values for the exchange current densities of hydrogen and oxygen and the total resistance of the measured fuel cell.

Appendix C

Preparation of thermocouples

C.1 Thermocouple description

The thermocouples used for measuring temperatures where thermocouples of type K, also denoted as the chromel-alumel thermocouple [Michalski et al., 1991]. The thermocouple wires consist of nickel-chromium (90 % Ni and 10 % Cr) and nickel-aluminium (95 % Ni and Al, Si and Mn in balance). Isolated thermocouple wire was delivered from Max Sievert A/S [1] in dimensions of AWG[2] 30 and 36, respectively 0.25 mm and 0.127 mm in diameter. The isolation was PTFE (Teflon$^{\mathrm{TM}}$).

A schematic drawing of a thermocouple element is given in figure C.1. The measuring junction was obtained by twisting the two different thermocouple wires together in a junction. A normal copper-type wire was connected to the thermocouple wires at the reference temperature junction. The voltage signal was measured by a high impedance multimeter. The temperature at the reference temperature junction was measured with a Pt-100 resistance thermometer.

The voltage signal was corrected for the temperature at the reference junction (room temperature) and converted to temperature by interpolating from a reference table [Isothermal technology limited, 1995].

---

[1] Breig. 12, 0187 Oslo, Norway

[2] American Wire Gauge

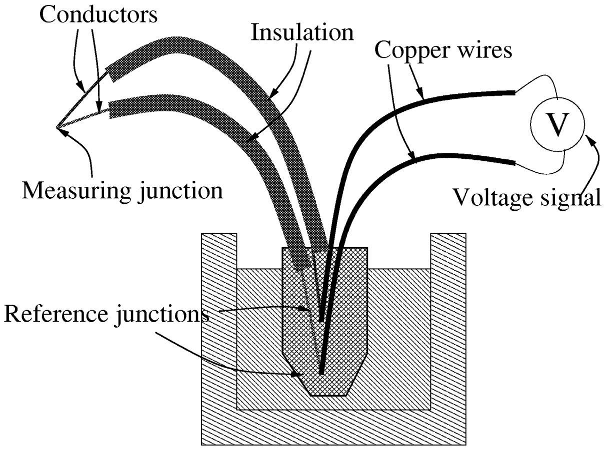

Figure C.1: A schematic drawing of a thermocouple element. The reference junction is in a glass tube filled with silicon oil immersed in a water-filled thermos.

C.2 Coating the thermocouples

The measuring junction and the thermocouple wires have to be chemically and electrically isolated from the measuring system. Otherwise the thermocouple element can oxidise and the measuring circuit will be broken. Electric contact with the measurement system can force current through the wires and this could affect the measured voltage from the thermocouple element. The coating has to be relatively thin, compared to the dimension of the thermocouple wires. This will increase the temperature sensing speed and preferably keep the total dimension of the thermocouple element smaller than the system it is going to measure. In the fuel cell system this means that the total thickness of the thermocouple element should be less than 100 μm and the thickness of the coating should be less than 20 - 30 μm.

Several types of coating for the thermocouple elements were tested. A suspension of Teflon$^{\mathrm{TM}}$[3] was tried. This suspension gave a brittle, not homogeneous and “thick” coating. We got the same problems with a solution of PVDF[4]. The coating was brittle and would not stick to the surface of the ther-

---

[3] 60 wt% in H_2O, Sigma-Aldrich Cat.no. 44509-6

[4] poly(vinylidene fluoride)

mocouple element surface. Epoxy glue was also tried[5], but the surface tension in the glue prevented a full surface coverage of the thermocouple element.

A class of resins made for the electronics industry was examined[6]. The resins are used for making homogeneous thin films (2 - 20 μm) on for instance silicon wafers. They are derived from B-staged bisbenzocyclobutene (BCB) monomers [Dow Chemical Company]. Several resins were tested; Cyclotene 4024-40, Cyclotene 4026-46 and Cyclotene 3022-57. Due to its relatively high viscosity, Cyclotene 4026-46 gave the best and most uniform coating on the thermocouple elements and was therefore chosen for further experimenting.

C.2.1 Procedure for coating thermocouple elements with Cyclotene 4026-46

The procedure below is a modification of a procedure found in [Dow Chemical Company] for making films on silicone wafers.

1. The thermocouple junction and the bare thermocouple wires, now called thermocouple tip, were thoroughly cleaned. Visible rests of the removed isolation were removed, and then further cleaned in different detergents and solvents:
   (a) The bare wires of the thermocouple element were cleaned in a detergent solution (soap) in an ultrasonic bath for 5 minutes.
   (b) The element was further cleaned with Opticlean[7] in an ultrasonic bath for 5 minutes.
   (c) Then the element was cleaned in acetone in an ultrasonic bath for 5 minutes.
   (d) The element was also cleaned in methanol in an ultrasonic bath for 5 minutes.
   (e) Finally the element was rinsed in purified water (distilled water quality) in an ultrasonic bath for 5 minutes, and then dried at 100 °C in an oven for 30 minutes.
2. The thermocouple tip was then dipped in an adhesion promoter, AP 3000 from the Dow Chemical Company, and the surplus was spun off in

---

[5] Epoxy Rapid, Casco Nobel

[6] CYCLOTENE® Resins from The Dow Chemical Company

[7] citric acid based detergent

a centrifugal separator for approximately 30 seconds at 2000 rpm (rounds per minute).

3. Then the thermocouple tip was dipped in Cyclotene 4026-46, letting surplus of the resin go back into the resin container, and then spinning off the rest of the surplus in the same centrifugal separator as above (point 2). The spinner was started slowly and thereafter the spinning speed was slowly increased to 1000 - 2000 rpm. The thermocouple tip was kept spinning at top speed (1000 - 2000 rpm) for 20 seconds.

4. Then the element was dried in a hot convection oven at 150 °C for 60 minutes, ramping the temperature from room-temperature and back.

5. This procedure was then repeated from point 3 above 3-4 times.

6. Then the polymer film was hardcured [Dow Chemical Company] at 250 °C for one hour in nitrogen atmosphere. The temperature in the oven was increased slowly from room temperature to 250 °C, then kept at 250 °C for one hour and then let to cool down naturally.

7. The polymer film was inspected visually in a microscope and the electronic isolating property was tested by measuring the ohmic resistance (impedance) between the thermocouple tip and a copper-wire immersed in a solution of $\mathrm{NaCl(aq)}$. If the total resistance in the system was higher than 1 GΩ the thermocouple tip was supposed to be chemically and electrically sealed/isolated. If the total resistance measured above was less than 1 GΩ the coating procedure was repeated from point 3 above until the resistance was higher than 1 GΩ.

The final isolated thermocouple element was then tested in a water-bath for testing of the temperature sensor and for testing of the offset in temperature from similar prepared thermocouples.

C.3 Testing of isolated thermocouples

Several of the prepared thermocouples were tested in a thermostated water bath for days. To reduce temperature fluctuations the thermocouple elements were kept in a beaker with distilled water inside another beaker with distilled water in the thermostated water bath. The largest beaker did also contain

600 g of stainless steel working as a heat sink. In this system very stable temperatures were obtained (± 0.01 °C for more than ten hours) In figure C.2 and C.3 one can see the measured temperature of four different thermocouples measured in the same water bath at the same time. In figure C.3 there has been a slight change in the positions of the thermocouples in the system. In table C.1 the average values and standard deviations for the measured temperatures in figure C.2 and C.3 are presented. The largest offset between the thermocouples was 0.06 °C, and the standard deviations for each measurement for 10 hours testing was varying from 0.01 to 0.02 °C. The variation in the temperature of the Pt-100 reference element in figure C.3 is due to fluctuations in the room temperature, which eventually affects the temperature in the isolated thermos containing the Pt-100 sensor and the reference temperature junctions of the thermocouple elements. One should notice that the temperatures in the water-bath are not varying noticeably.

Table C.1: The average values for the measurements given in figure C.2 and figure C.3

Time [hours]		Temp 1 [°C]	Temp 2 [°C]	Temp 3 [°C]	Temp 4 [°C]
34-	average value	41.660	41.707	41.722	41.658
44	standard deviation	0.011	0.022	0.017	0.011
45-	average value	41.717	41.745	41.774	41.738
49.5	standard deviation	0.011	0.010	0.010	0.011

The offset in average values for the measured thermocouple elements, indicates that the elements that is going to be used simultaneously, should be thoroughly calibrated internally. If not, one would not be able to trust the absolute values with better than approximately 0.1 °C significance. A thorough calibration could give an accuracy of less than 0.01 °C. The relative change in the temperatures can however be trusted to 0.02 °C anyway. In table C.1 we can see a slight change in average values for the different thermocouples. This change is due to repositioning of the temperature sensors in the small glass beaker. The positioning of the thermocouples is therefore vital in this experiment and the accuracy of the thermocouples could be even better than established here. The number of thermocouples tested simultaneously are also quite low. Therefore, the total accuracy was set to 0.1 °C.

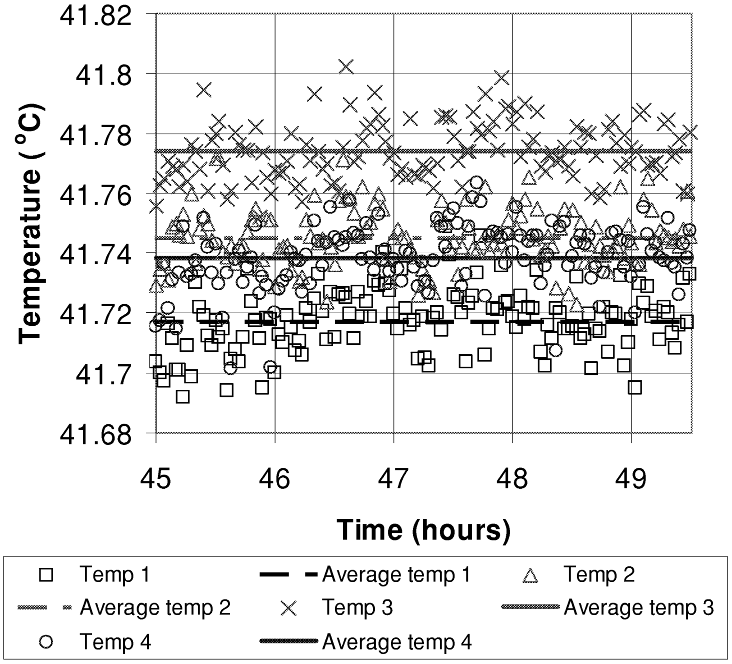

Figure C.2: Measured temperatures for four different thermocouples of type k for more than 38 hours. Temperature for the Pt-100 reference sensor is also given.

C.4 Stability of the coating

The isolated thermocouples were installed in the fuel cell housing described in appendix 2. The thermocouple elements were tested for a long time in the fuel cell (more than 200 hours), checking for changes in the performance and reversible cell voltage (open-circuit voltage). There was no changes in the fuel cell performance that could be stated to come from contamination from the isolation of the thermocouples. The reversible cell voltage was very stable and the cell performance did not decrease any faster than normal. Hence, the isolation is concluded to be inert to the polymer fuel cell conditions and the “Cyclotene” polymers are therefore chosen as the best tested thermocouple isolation in the fuel cell.

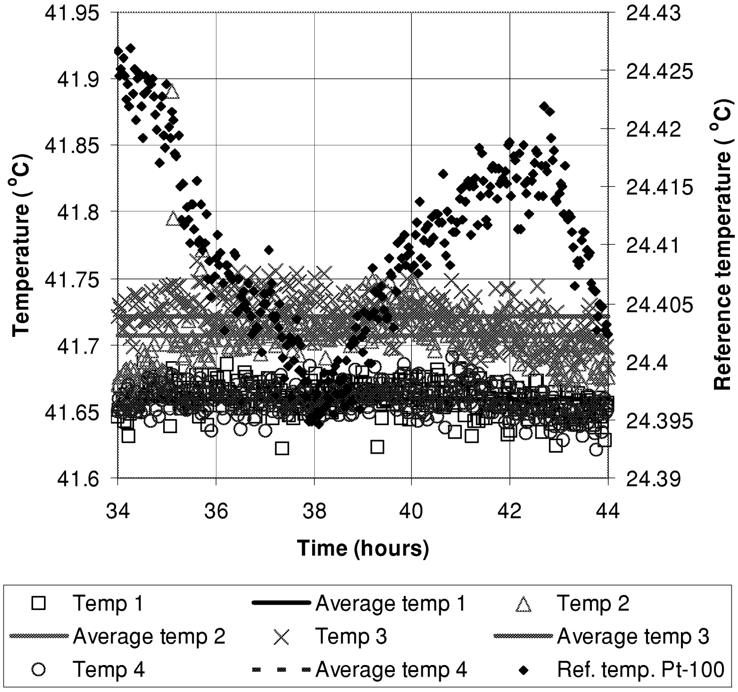

Figure C.3: Measured temperatures for four different thermocouples of type k for more than 38 hours. Temperature for the Pt-100 reference sensor is also given.

C.5 The dimension of the isolated thermocouple

The thermocouple wires of approx. 130 μm were twisted into a contact point (measuring junction) . This should give a dimension of the contact point of at least 260 μm. With a thickness of the isolating polymer layer of 10 - 20 μm, the total thickness of the thermocouple element would be at least 280 μm.

Appendix D

The data acquisition system and control program

D.1 The data acquisition system

The data acquisition system has evolved since the first version [Møller-Holst, 1996b]. Several features have been added and new possibilities for fuel cell control are included: The fuel cell load is better controlled, and the mass flow rates can be controlled according to the conversion of the reacting gases. Easier programmed measurements of polarisation curves are also enabled.

The basis for the measurement system is still a computer (now a Pentium 300MHz, 64MByte RAM, 6 GByte Harddisk) programmed with LabVIEW; version 5.1. LabVIEW is a graphical programming language from National Instruments. The program controls the fuel cell test-station through the GPIB bus (National Instruments PCI-GPIB), a PC-DIO 24, digital input/output, board and the RS-232 bus. Several instruments are connected to the computer through these boards:

- GPIB bus:
  - Two Hp 3457A multimeters with 10 and 8 channel multiplexers for voltage measurements. The front panel is used for 4 electrode resistance measurements (Pt-100).
  - Hp 6060B current load
  - Hp 6032A power supply

  - Schlumberger multimeter for current measurements

- PC-DIO 24 card:
  - A in-house-made box for control of mass-flow controllers and pressure controllers (The “Relay box”). The box was made by the electronics workshop at the Department of Chemistry, NTNU.

- RS-232 bus:
  - Combined with the in-house box described above

The functioning and features of the fuel cell test-station control system will be described from the control window of the program. In figures D.2 and D.3 the control window is presented. Most of the controls are self-explaining[1], but a brief discussion of the panels and controls will be given below. The information screen in figures D.4 and D.5 will also be discussed.

D.2 Control program

D.2.1 The main screen

The main screen in the data-acquisition program controls all the necessary adjustments of the fuel cell test-station. All the most important data are also presented there.

The reacting gases

In the upper left corners of figures D.2 (“Cathode gas”) and D.3 (“Anode gas”), controls and information of the entering gases are given. The temperature of the humidifiers is measured with Pt-100 resistance thermometers at the position given in figure 2.6. The temperature is controlled with PID controllers from Eurotherm[2] (type 2408). The controllers give a voltage signal to the computer, which is read by the Hp 3457A multimeters and conditioned into temperatures.

The gas pressure is controlled by Brooks pressure controllers (Model 5866). A digital signal is sent from the DIO24 card to the “Relay box”, and the “Relay

---

[1] At least to the trained user...

[2] Eurotherm A/S, Postboks 227, NO-1326 Lysaker

box" sends a signal to the pressure controller. An analog signal is sent back to the "Relay box" and further read by the Hp 3457A multimeter. An option for switching from oxygen to air on the cathode is given but not yet implemented in the laboratory. So far the gases used have been pure oxygen and hydrogen.

The cathode gas composition is calculated from the measured temperature of the humidifier and the corresponding vapour pressure of water and the gas pressure of the system.

The mass flow rates are controlled from Brooks mass flow controllers (Model 5850S). A digital signal is sent from the PC-DIO24 card to the "Relay box", and an analog signal is sent to the controller. The flow rate read-out is measured by the Hp 3457A multimeters. The conversion of the reacting gases is calculated from the total current through the system and the measured flow rates. The mass flow rates have different set-points. One set-point is for normal operation, the other set-point is when a programmed scan is being performed. The mass flow rates can also be controlled according to the conversion of the gases. This is set in the box: "Adjust mass flow from conversion" in figure D.3. In addition to adjusting the wanted conversion, maximum and minimum levels of the flow-rates can also be set.

The water consumption of the humidifiers are calculated. It depends on the temperatures, the gas pressures and the flow-rates of the humidifiers.

The fuel cell

The information and controls of the fuel cell are given in the fuel cell box in figure D.2, in the upper right corner. The temperatures on the cathode and anode are measured with type K thermocouples. The thermocouples are positioned at the outlet of the gas flow channels on the anode and cathode. The preparation of the thermocouples is described in appendix C. The cold junction temperature (room temperature, 20 - 25 °C) was measured with a Pt-100 resistance thermometer. The measured thermocouple voltages were corrected for the offset of the reference temperature from the normally tabulated ice-reference temperature. Then a correct temperature could be calculated. The room temperature reference was chosen since the measured temperatures were much more stable with this reference. Only small temperature gradients would exist at the reference junction (appendix C). There could be a minor offset from the true temperature, but the difference between the thermocouples should be correct. The temperature of the heating elements ("Contr. temp.") on the cathode and anode is measured in the same way as the temperature of the humidifiers. These temperature sensors are positioned close to the heating elements and do not give a precise fuel cell temperature.

The overpotentials are measured voltages at the anode and cathode, usually the voltage difference between a reference electrode and the working electrodes. In figure D.2 the “cathodic overpot.” is measuring the cell voltage at the pistons. The “anodic overpot.” is shorted.

The measured cell voltage at the backing, the current density and the power density are given in an inverted table array, the last measured values are in the first element. The last cell current and cell power are also given. They form the basis for calculating the current and power densities. To calculate the densities the program needs to know the fuel cell active area. It is given in the “Cell Area” control.

The time span of the total results array can also be set. A large value will make it possible to track changes and errors in the fuel cell. The length of time-axis of the process-curves can also be controlled. The process curves are given in the lower right corner of figure D.2.

Controlling the fuel cell

The fuel cell can be controlled either manually or through a programmed variation of the load (Hp 6060B DC). In manual mode the load can be set in the control: “Load”. The mode of the DC Load can be set either to constant resistance, voltage or current. The most normal modes are either the constant current or constant voltage modes. The load can be turned on or off by the switch “Input On/Off”. A programmed scan/variation of the load can also be performed. It is started by pressing the “Take SCAN” button. You are able to build a new scan or choose a previously built scan. In the “Scan mode” in the lower left corner of figure D.2, information of the current scan is given. The measured data in the scan can also be plotted as a polarisation curve by pressing the “Show POL” button.

The current is measured either with the Hp 6060B DC load, or at lower currents, with the more exact amperemeter in the Schlumberger multimeter model. The current limit for measuring the current with the DC load is given in a control. The reason for having this control is the need and possibility to test both well performing fuel cells and poorer cells. The Schlumberger multimeter adds extra resistance to the outer circuit, and therefore there can be a need to measure lower currents with the Hp 6060B.

Lately, the Hp 6032A power supply has been added to the fuel cell test-station. This instrument enables operation of cells with hydrogen on both anode and cathode. The instrument is operated in a slightly different way than the DC load. Depending on which maximum value that is limiting, it regulates the system either in constant current or constant voltage mode. This can be seen from figure D.2. The measured voltage over the power supply is 0.495 V and the current is 5.325 A. Therefore the voltage is the limiting value (maximum voltage is 0.5 V), and the power supply is in constant voltage mode. The power supply can also be used when running in normal fuel cell mode. This is the fact in figure D.2. The power supply raises the total voltage over the DC current load. See figure D.1. This makes it possible to run the fuel cell at low cell voltage, independent of the external ohmic resistance.

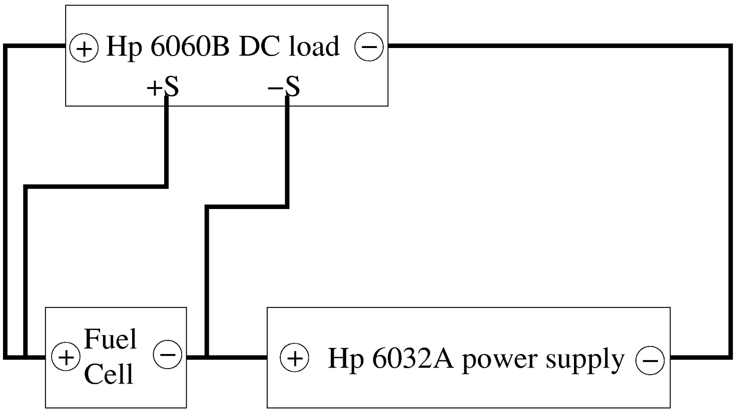

Figure D.1: The electrical circuit of the fuel cell system in normal fuel cell mode with the Hp 6032A power supply. The power supply raises the total voltage drop at the DC load. The “+S” and “-S” connections are the sense leads from the DC load to the tested fuel cell.

Saving the data

All information about saving data and controlling the saving is given in the upper right corner of figure D.3; “File and Measurement information”. Saving of data can be stopped or started, and saving can be temporarily paused. The interval between each measurement cycle can be controlled, and the interval between saving the data to file can be adjusted. When performing a scan it can be advantageous to save the data more often, and this is also controlled. Comments can be saved to the main file. When performing a scan, data is saved to an additional file to ease the data analysis. It is possible to control which temperatures that are saved to the data file. The simplest configuration of the test-station does not use thermocouples for detailed temperature monitoring. Instead, the temperatures at the heating elements can be saved.

Measuring more variables

The data-acquisition program is flexible. Several extra temperatures can be measured, or maybe there is a need to measure some extra voltages. This can be controlled in the "Measure more variables" box in figure D.3. The thermocouples are measured in the same way as the thermocouples in the fuel cell.

In this box it is also possible to program the computer to send email updates of the last measurements. When this option is active, the computer will also send a warning to the operator at an emergency. The emergency action is described below.

Emergency action and regulation of cell voltage

In the lower left corner of figure D.3 the control of the fuel cell at an emergency situation is controlled. The flow of hydrogen and oxygen will be reduced to a minimum (Mass flow setpoint at "0"). Usually something is wrong when the cell voltage drops below 0.1 V, and probably there is a hole in the membrane when the cell voltage is around 0 V. A fire is indicated by a higher temperature in the fuel cell. The emergency action can be triggered by a measured fuel cell temperature that is higher than wanted.

In the box above the emergency action, it is possible to regulate the load if the cell voltage drops below a specified level when operating the fuel cell in constant current mode or constant resistance mode. This is a simple regulation routine which reduces the given load so that the voltage increases above the specified level. This feature is important for unstable fuel cells. A low cell voltage over a long time can reduce the fuel cell performance permanently.

Instrument information

Data from the instruments can be vital when checking a data-acquisition program for errors. Therefore a box with all the measured data is included in the main screen of the data-acquisition program. This box is in the lower right corner of figure D.3.

D.2.2 The information screen

When the fuel cell system is performing well, the experimenter is interested in the measured data. A window with the most important process-data has therefore been constructed. The window is opened by pressing the button in the upper left corner of figure D.2. The information window is presented in figures D.4 and D.5. Information about the reacting gases and the file saving are presented in the same way as in the main screen. The most important information is the graphical presentations of the cell voltage, current density, power density and temperatures as a function of time. A large reversed data-array presents the same data below the plots. Another feature makes it possible to search for the specific data at a given time.

D.3 Analyzing the data

The data from the data-acquisition program can be analysed in a spreadsheet. This author has programmed several macros running in Visual Basic/Microsoft Excel 97. Diagrams with all the important data can easily be processed, and the automated polarisation curves is plotted. The macros help to reduce the amount of data and ease the work analysing them.

Matlab® [MathWorks, Inc., 2002] was used for plotting the three-dimensional curves.

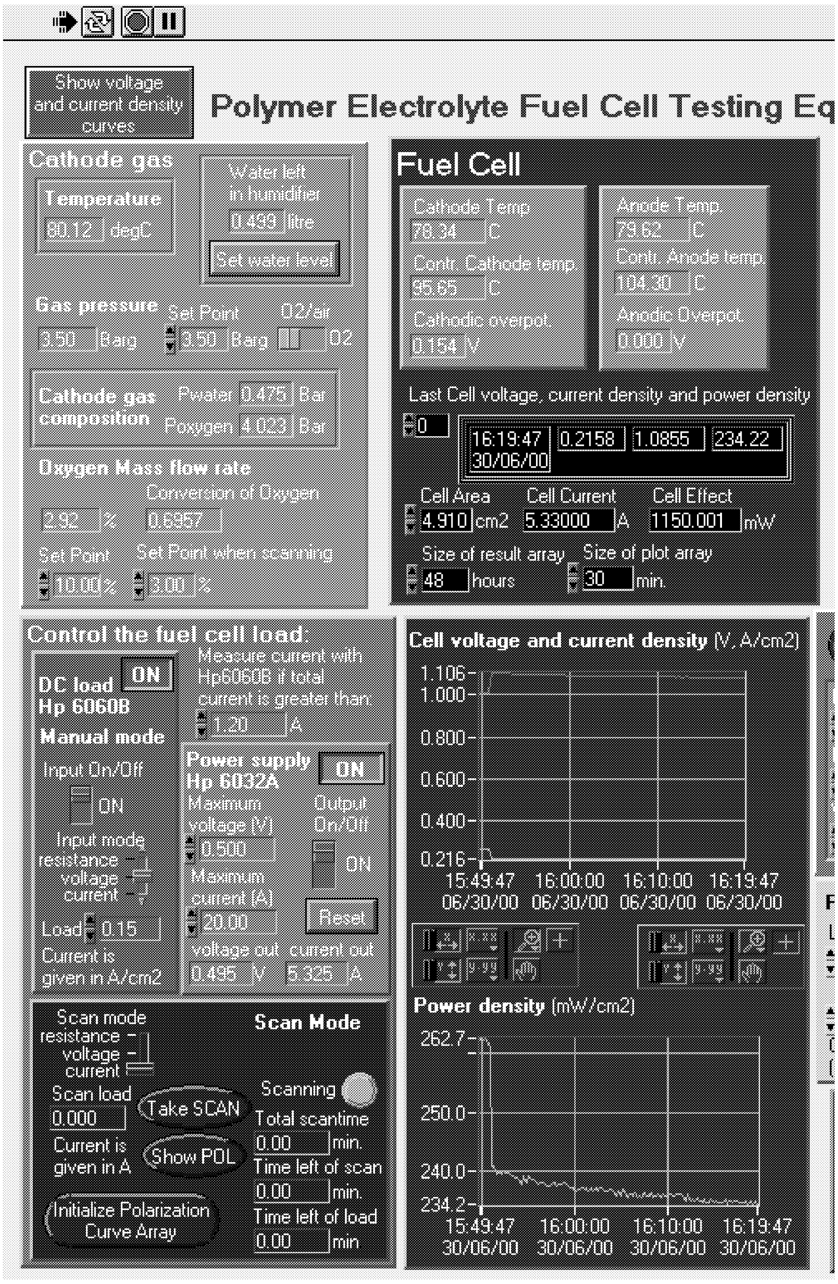

Temperature 80.12 degC

Water left in humidifier 0.499 litre

Gas pressure 3.50 Barg

Set Point 3.50 Barg

O2/air O2

Cathode gas composition

Pwater 0.475 Bar

Poxygen 4.023 Bar

Oxygen Mass flow rate 2.92 %

Conversion of Oxygen 0.6957

Set Point 10.00 %

Set Point when scanning 3.00 %

Cathode Temp 78.34 C

Contr. Cathode temp. 95.65 C

Cathodic overpot. 0.154 V

Anode Temp. 79.62 C

Contr. Anode temp. 104.30 C

Anodic Overpot. 0.000 V

Last Cell voltage, current density and power density

0

16:19:47 30/06/00	0.2158	1.0855	234.22

Cell Area 4.910 cm2

Cell Current 5.33000 A

Cell Effect 1150.001 mW

Size of result array 48 hours

Size of plot array 30 min.

Measure current with Hp6060B if total current is greater than 1.20 A

Input On/Off ON

Input mode resistance voltage current

Load 0.15

Current is given in A/cm2

Maximum voltage [V] 0.500

Output On/Off ON

Maximum current [A] 20.00

voltage out 0.495 V

current out 5.325 A

Scan mode resistance voltage current

Scan load 0.000

Current is given in A

Total scantime 0.00 min.

Time left of scan 0.00 min.

Time left of load 0.00 min

Figure D.2: Left half of main screen from the data-acquisition program.

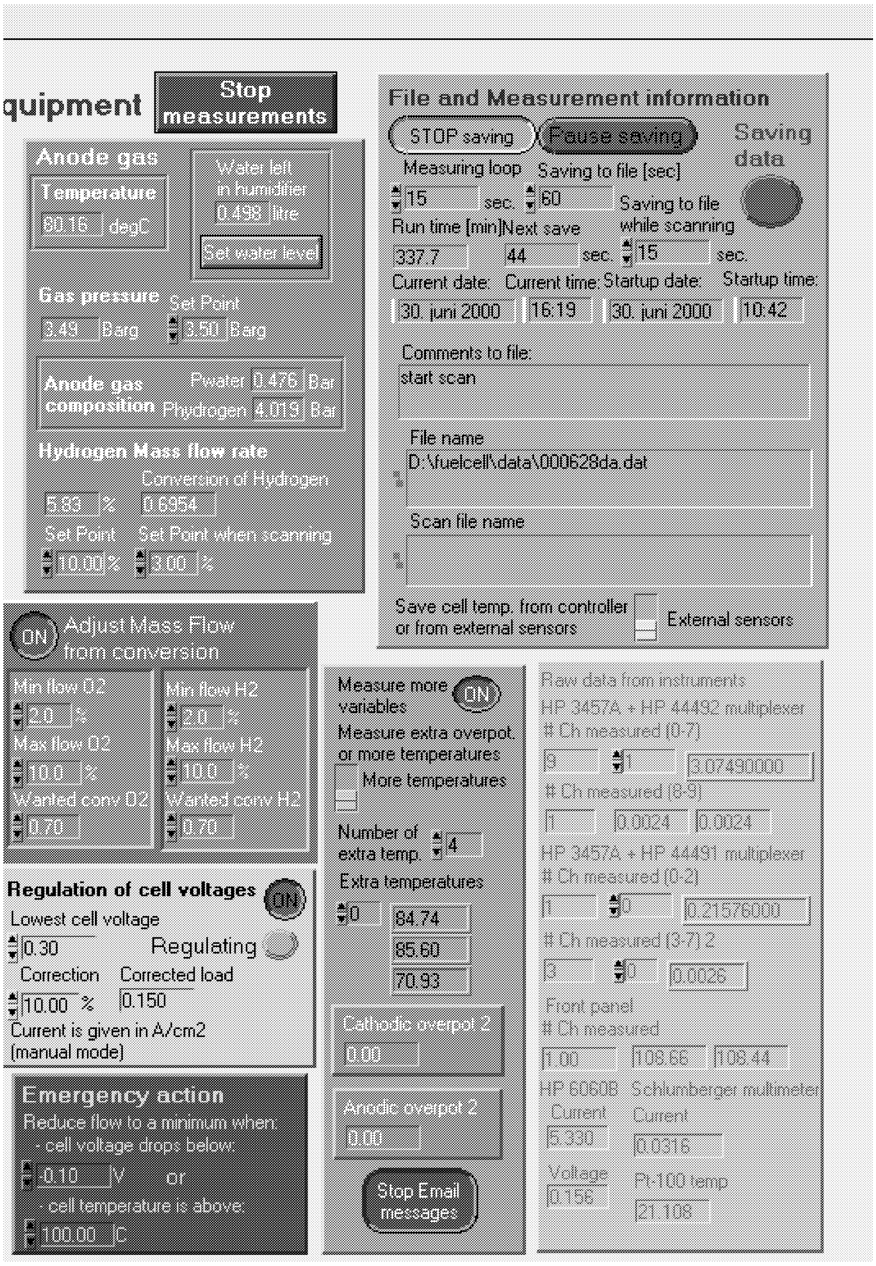

Temperature 80.16 degC

Water left in humidifier 0.498 litre

Gas pressure 3.49 Barg

Set Point 3.50 Barg

Anode gas composition

Pwater 0.476 Bar

Phydrogen 4.019 Bar

Hydrogen Mass flow rate 5.83 %

Conversion of Hydrogen 0.6954

Set Point 10.00 %

Set Point when scanning 3.00 %

Min flow O2 2.0 %

Max flow O2 10.0 %

Wanted conv O2 0.70

Min flow H2 2.0 %

Max flow H2 10.0 %

Wanted conv H2 0.70

Regulation of cell voltages ON

Lowest cell voltage 0.30

Regulating

Correction 10.00 %

Corrected load 0.150

Current is given in A/cm2 (manual mode)

Reduce flow to a minimum when:

- cell voltage drops below: -0.10 V or
- cell temperature is above: 100.00 C

Measuring loop 15 sec.

Saving to file [sec] 60

Run time [min] 337.7

Next save 44 sec.

Saving to file while scanning 15 sec.

Current date: 30. juni 2000

Current time: 16:19

Startup date: 30. juni 2000

Startup time: 10:42

Comments to file: start scan

File name D:\fuelcell\data\000628da.dat

Scan file name

Save cell temp. from controller or from external sensors: External sensors

Measure more variables ON

Measure extra overpot. or more temperatures: More temperatures

Number of extra temp. 4

Extra temperatures 0 84.74 85.60 70.93

Cathodic overpot 2 0.00

Anodic overpot 2 0.00

HP 3457A + HP 44492 multiplexer

Ch measured (0-7) 8 1 3.07490000

Ch measured (8-9) 1 0.0024 0.0024

HP 3457A + HP 44491 multiplexer

Ch measured (0-2) 1 0 0.21576000

Ch measured (3-7) 2 3 0 0.0026

Front panel

Ch measured 1.00 108.66 108.44

HP 6060B Current 5.330

HP 6060B Voltage 0.156

Schlumberger multimeter Current 0.0316

Pt-100 temp 21.108

Figure D.3: Right half of main screen from the data-acquisition program.

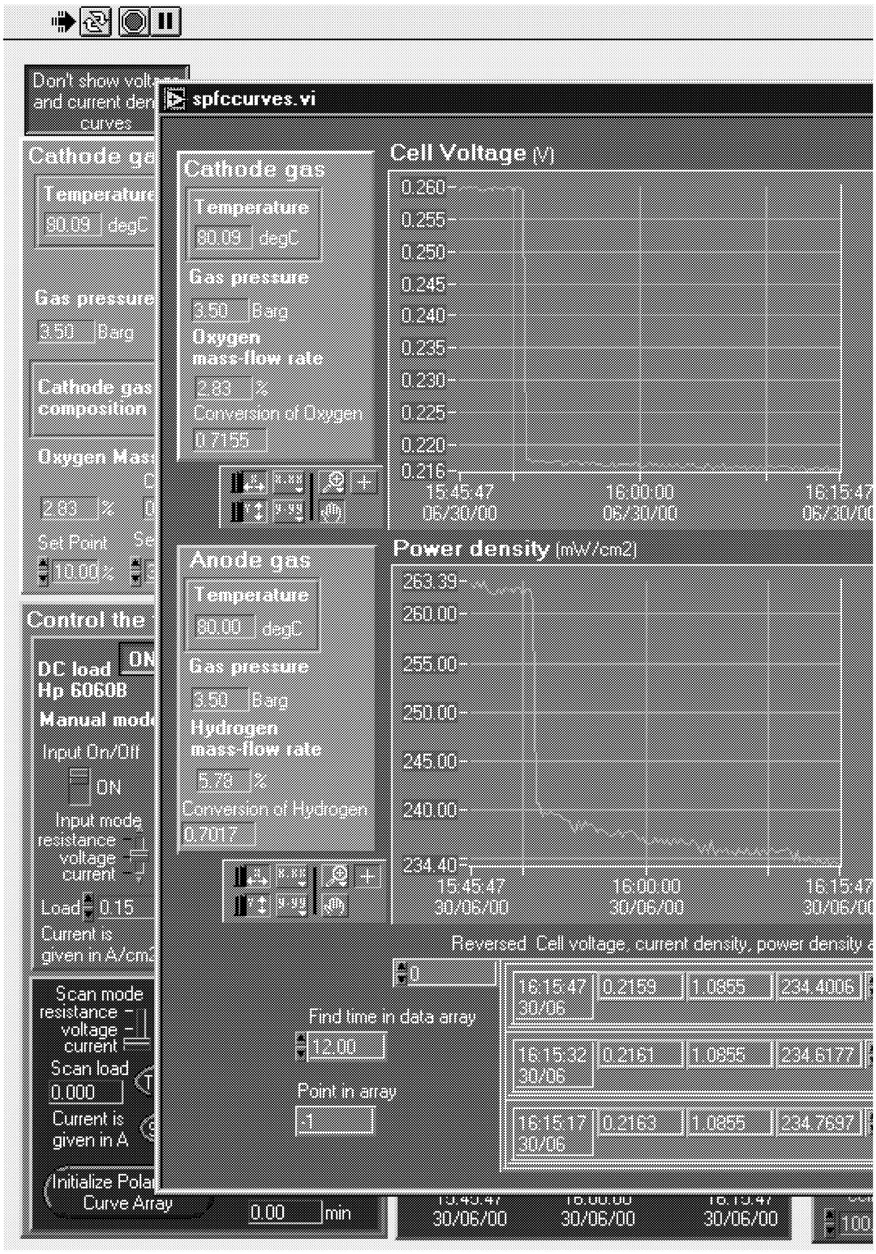

spfccurves.vi

Cathode gas

Temperature 80.09 degC

Gas pressure 3.50 Barg

Oxygen mass-flow rate 2.83 %

Conversion of Oxygen 0.7155

Anode gas

Temperature 80.00 degC

Gas pressure 3.50 Barg

Hydrogen mass-flow rate 5.73 %

Conversion of Hydrogen 0.7017

Find time in data array 12.00

Point in array -1

Reversed Cell voltage, current density, power density a

16:15:47 30/06	0.2159	1.0855	234.4006
16:15:32 30/06	0.2161	1.0855	234.6177
16:15:17 30/06	0.2163	1.0855	234.7697

Figure D.4: Left half of information screen from the data-acquisition program.

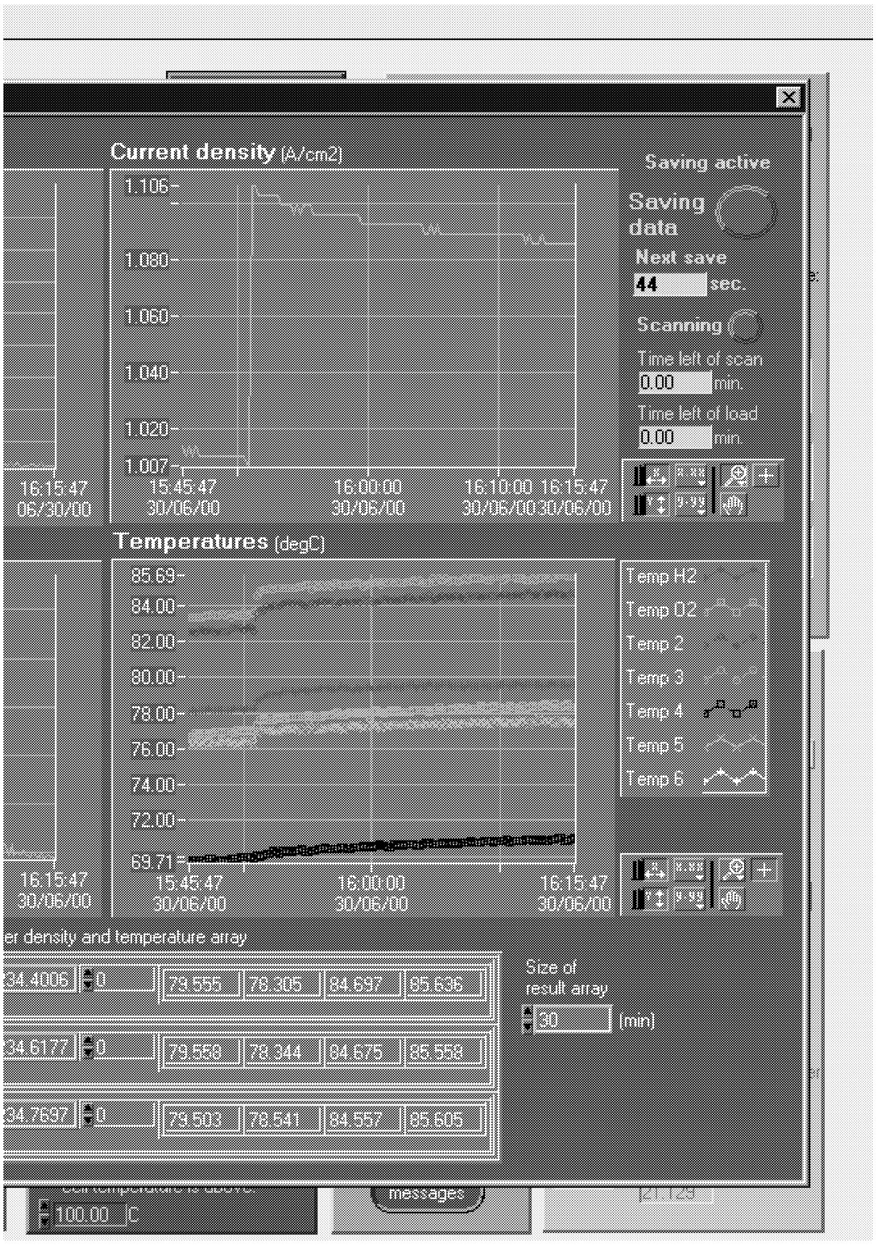

Next save 44 sec.

Time left of scan 0.00 min.

Time left of load 0.00 min.

er density and temperature array

34.4006 0 79.555 78.305 84.697 85.636

34.6177 0 79.558 78.344 84.675 85.558

34.7697 0 79.503 78.541 84.557 85.605

Size of result array 30 [min]

100.00 C

Figure D.5: Right half of information screen from the data-acquisition program.